



## Calhoun: The NPS Institutional Archive DSpace Repository

---

Theses and Dissertations

1. Thesis and Dissertation Collection, all items

---

1987

### Optimizing superplastic response in lithium containing aluminum-magnesium alloys.

Munro, Ian Glenn.; McNelley, Terry R.

---

<http://hdl.handle.net/10945/22400>

---

*Downloaded from NPS Archive: Calhoun*



<http://www.nps.edu/library>

Calhoun is the Naval Postgraduate School's public access digital repository for research materials and institutional publications created by the NPS community.

Calhoun is named for Professor of Mathematics Guy K. Calhoun, NPS's first appointed -- and published -- scholarly author.

Dudley Knox Library / Naval Postgraduate School  
411 Dyer Road / 1 University Circle  
Monterey, California USA 93943









# NAVAL POSTGRADUATE SCHOOL

## Monterey , California



# THEESIS

M9525

OPTIMIZING SUPERPLASTIC RESPONSE  
IN LITHIUM CONTAINING  
ALUMINUM-MAGNESIUM ALLOYS

by

Ian G. Munro

• • •

December 1987

Thesis Advisor  
Co-Advisor

T. R. McNelley  
S. J. Hales

Approved for public release; distribution is unlimited.

123-212



## REPORT DOCUMENTATION PAGE

1a REPORT SECURITY CLASSIFICATION Uncclas.		1b RESTRICTIVE MARKINGS	
2a SECURITY CLASSIFICATION AUTHORITY		3 DISTRIBUTION/AVAILABILITY OF REPORT Distribution unlimited.	
2b DECLASSIFICATION/DOWNGRADING SCHEDULE			
4 PERFORMING ORGANIZATION REPORT NUMBER(S)		5 MONITORING ORGANIZATION REPORT NUMBER(S)	
6a NAME OF PERFORMING ORGANIZATION Naval Postgraduate School		6b OFFICE SYMBOL (If applicable) 69	7a NAME OF MONITORING ORGANIZATION Naval Postgraduate School
6c ADDRESS (City, State, and ZIP Code) Monterey, CA. 93943 - 5000		7b ADDRESS (City, State, and ZIP Code) Monterey, CA. 93943 - 5000	
8a NAME OF FUNDING SPONSORING ORGANIZATION		8b. OFFICE SYMBOL (If applicable) 69	9. PROCUREMENT INSTRUMENT IDENTIFICATION NUMBER
10c. ADDRESS (City, State, and ZIP Code)		10 SOURCE OF FUNDING NUMBERS	
		PROGRAM ELEMENT NO.	PROJECT NO.
		TASK NO.	WORK UNIT ACCESSION NO
1. TITLE (Include Security Classification) OPTIMIZING SUPERPLASTIC RESPONSE IN LITHIUM CONTAINING ALUMINUM-MAGNESIUM ALLOYS			
2. PERSONAL AUTHOR(S) Munro, Ian Glenn			
3a. TYPE OF REPORT	13b TIME COVERED FROM _____ TO _____	14 DATE OF REPORT (Year, Month, Day) 1987 December	15 PAGE COUNT 93
6. SUPPLEMENTARY NOTATION			
7 COSATI CODES		18 SUBJECT TERMS (Continue on reverse if necessary and identify by block number) Aluminum-Magnesium-Lithium, Superplastic Response, Superplasticity, Thermomechanical Processing	
19 ABSTRACT (Continue on reverse if necessary and identify by block number)			
<p>Four lithium containing Al-Mg-Zr alloys, containing 6-8 wt. pct. Mg, 0.5-2 wt. pct. Li, and 0.15-0.25 wt. pct. Zr, were studied with a view to maximizing superplastic ductilities. Differential scanning calorimetry was employed to assist in the characterization of the microstructures and to determine the solvi of the constituent second phases. These data were used to aid in the choice of thermomechanical processing parameters previously applied to Al-Mg alloys containing 10 wt. pct. magnesium. The superplastic response of the alloys was evaluated over a range of temperatures (275°C to 350°C) and a range of strain rates (10<sup>-4</sup> to 10<sup>-1</sup> sec<sup>-1</sup>). Elongations in excess of 1000% at 300°C and 1.7 x 10<sup>-2</sup> sec<sup>-1</sup> strain rate were obtained in a Al-8Mg-1Li-0.15Zr (wt. pct.) alloy. Transmission electron microscope investigations of the microstructure before and after superplastic deformation revealed that the volume fraction of second phase was predominantly responsible for structural stability.</p>			
20 DISTRIBUTION/AVAILABILITY OF ABSTRACT <input checked="" type="checkbox"/> UNCLASSIFIED/UNLIMITED <input type="checkbox"/> SAME AS RPT <input type="checkbox"/> DTIC USERS		21. ABSTRACT SECURITY CLASSIFICATION Uncclas.	
22a NAME OF RESPONSIBLE INDIVIDUAL Prof. T.R. McNelley		22b TELEPHONE (Include Area Code) (408) 646-2589	22c. OFFICE SYMBOL 69

Approved for public release; distribution is unlimited.

Optimizing Superplastic Response  
in Lithium Containing  
Aluminum-Magnesium Alloys

by

Ian G. Munro  
Captain, Canadian Armed Forces  
B Eng, Royal Military College of Canada, 1978

Submitted in partial fulfillment of the  
requirements for the degree of

MASTER OF SCIENCE IN MECHANICAL ENGINEERING

from the

NAVAL POSTGRADUATE SCHOOL  
December 1987

## ABSTRACT

Four lithium containing Al-Mg-Zr alloys, containing 6-8 wt. pct. Mg, 0.5-2 wt. pct. Li, and 0.15-0.25 wt. pct. Zr, were studied with a view to maximizing superplastic ductilities. Differential scanning calorimetry was employed to assist in the characterization of the microstructures and to determine the solvi of the constituent second phases. These data were used to aid in the choice of thermomechanical processing parameters previously applied to Al-Mg alloys containing 10 wt. pct. magnesium. The superplastic response of the alloys was evaluated over a range of temperatures (275°C to 350°C) and a range of strain rates ( $10^{-5}$  to  $10^{-1}$  sec $^{-1}$ ). Elongations in excess of 1000% at 300°C and  $1.7 \times 10^{-2}$  sec $^{-1}$  strain rate were obtained in a Al-8Mg-1Li-0.15Zr (wt. pct.) alloy. Transmission electron microscope investigations of the microstructure before and after superplastic deformation revealed that the volume fraction of second phase was predominantly responsible for structural stability.

## TABLE OF CONTENTS

I.	INTRODUCTION .....	10
II.	BACKGROUND .....	12
	A. ALLOYING ELEMENTS .....	13
	1. Magnesium .....	13
	2. Lithium .....	14
	3. Aluminum-Magnesium-Lithium Ternary System .....	15
	4. Zirconium .....	16
	B. SUPERPLASTICITY .....	16
	1. Phenomenological Description .....	16
	2. Microstructural Requirements .....	18
	C. THERMOMECHANICAL PROCESSING .....	18
	1. Alternative TMP .....	18
	2. NPS Procedure .....	19
	3. Warm Rolling Temperature .....	19
	4. Reheating Time Between Rolling Passes .....	20
	5. Reduction Per Rolling Pass .....	20
	6. Total Strain .....	20
	D. DIFFERENTIAL SCANNING CALORIMETER .....	20
III.	EXPERIMENTAL PROCEDURE .....	27
	A. DIFFERENTIAL SCANNING CALORIMETRY .....	27
	B. THERMOMECHANICAL PROCESSING .....	27
	C. ELEVATED TEMPERATURE TESTING .....	28
	D. DATA REDUCTION .....	31
	E. TRANSMISSION ELECTRON MICROSCOPY (TEM) .....	31
IV.	RESULTS .....	33
	A. DSC .....	33
	1. Al-8 wt. pct. Mg-0.5 wt. pct. Li .....	33

2.	Al-8 wt. pct. Mg-1 wt. pct. Li .....	33
3.	Al-6 wt. pct. Mg-1 wt. pct. Li .....	33
4.	Al-6 wt. pct. Mg-2 wt. pct. Li .....	34
B.	TMP .....	38
C.	MECHANICAL PROPERTIES .....	38
1.	Matrix of Experiments .....	38
2.	Al-8 wt. pct. Mg-1 wt. pct. Li .....	41
3.	Al-6 wt. pct. Mg-1 wt. pct. Li .....	43
4.	Al-8 wt. pct. Mg-0.5 wt. pct. Li .....	46
5.	Al-10 wt. pct. Mg-0 wt. pct. Li .....	46
D.	TEM .....	46
1.	Al-8 wt. pct. Mg-1 wt. pct. Li .....	46
2.	Al-6 wt. pct. Mg-1 wt. pct. Li .....	53
3.	Al-6 wt. pct. Mg-2 wt. pct. Li .....	58
V.	DISCUSSION .....	67
A.	DSC .....	67
B.	MECHANICAL PROPERTIES .....	68
C.	TEM .....	73
VI.	CONCLUSIONS .....	75
VII.	RECOMMENDATIONS .....	76
APPENDIX A:	DIFFERENTIAL SCANNING CALORIMETRY .....	77
APPENDIX B:	TRUE STRESS DATA .....	80
LIST OF REFERENCES .....	90	
INITIAL DISTRIBUTION LIST .....	92	

## LIST OF TABLES

1. NOMINAL ALLOY COMPOSITIONS .....	11
2. COMMERCIAL AL-MG ALLOYS COMPARED TO LI- CONTAINING ALLOYS .....	12
3. EXAMPLES OF SUPERPLASTIC ALUMINUM ALLOYS .....	13
4. ALLOY CONDITIONS AS TESTED IN THE DSC .....	28
5. TMP VARIABLES FOR EACH OF THE ALLOYS STUDIED .....	30
6. MATRIX OF ELEVATED TEMPERATURE EXPERIMENTS .....	41
7. TOTAL ATOMIC PERCENT SOLUTE CONTENT AND EQUIVALENT MAGNESIUM CONTENT .....	69
8. DSC CALIBRATION SETTINGS .....	77

## LIST OF FIGURES

2.1	DSC Apparatus Showing Theory of Operation .....	22
2.2	Aluminum-Lithium Binary Phase Diagram .....	23
2.3	Aluminum-Magnesium Binary Phase Diagram .....	24
2.4	Al-Li-Mg Ternary Phase Diagram at 425°C .....	25
3.1	NPS Thermomechanical Processing Procedure .....	29
3.2	Tensile Test Sample Geometry .....	30
4.1	DSC trace for the 8-1.2 alloy .....	35
4.2	DSC trace for the 8-1 alloy .....	35
4.3	DSC trace for the 6-1 alloy .....	36
4.4	DSC trace for the 6-2 alloy (1st run) .....	39
4.5	DSC trace for the 6-2 alloy (3rd run) .....	39
4.6	Mechanical properties vs strain rate for the 8-1 alloy .....	44
4.7	Tensile samples of the 8-1 alloy deformed at 300°C .....	45
4.8	Mechanical properties vs temperature for the 8-1 alloy .....	47
4.9	Variation in fracture mode due to temperature .....	47
4.10	Mechanical properties vs strain rate for the 6-1 alloy .....	48
4.11	Mechanical properties vs temperature for the 6-1 alloy .....	49
4.12	Mechanical properties for 4 identically processed alloys .....	51
4.13	10-0 and 8-1 prior to deformation .....	53
4.14	8-1 prior to deformation .....	54
4.15	8-1.2 and 8-1 following deformation at $1.7 \times 10^{-2} \text{ sec}^{-1}$ .....	55
4.16	8-1 bright field/dark field following deformation at $1.7 \times 10^{-2} \text{ sec}^{-1}$ .....	56
4.17	6-1 prior to deformation .....	57
4.18	6-1 bright field/dark field prior to deformation .....	59
4.19	6-1 following deformation at $1.7 \times 10^{-2} \text{ sec}^{-1}$ .....	60
4.20	6-1 bright field/dark field following deformation at $1.7 \times 10^{-2} \text{ sec}^{-1}$ .....	61
4.21	6-1 following deformation at $6.7 \times 10^{-3} \text{ sec}^{-1}$ .....	62
4.22	6-1 bright field/dark field following deformation at $6.7 \times 10^{-3} \text{ sec}^{-1}$ .....	63

4.23	6-2 in the as-rolled condition . . . . .	64
4.24	6-2 following 1 hour anneal at 300°C . . . . .	65
4.25	6-2 following DSC cycling . . . . .	66
B.1	The 8-1 Alloy at 275°C . . . . .	81
B.2	The 8-1 Alloy at 300°C . . . . .	81
B.3	The 8-1 Alloy at 325°C . . . . .	82
B.4	The 8-1 Alloy at 350°C . . . . .	83
B.5	The 6-1 Alloy at 275°C . . . . .	84
B.6	The 6-1 Alloy at 300°C . . . . .	85
B.7	The 6-1 Alloy at 325°C . . . . .	86
B.8	The 6-1 Alloy at 350°C . . . . .	88
B.9	The 8-1 2 Alloy at 300°C . . . . .	88

## ACKNOWLEDGEMENTS

I would like to express my sincere gratitude to Professor T.R. McNelley and Dr. S.J. Hales for their expert guidance and enthusiastic support throughout this research. The technical expertise of Tom Kellogg, Tammy Bloomer and Tom McCord was also greatly appreciated. Lastly, my thanks go to Procopis Spiropoulos and Bill Ferris, fellow students whose willing assistance contributed much to this research.

## I. INTRODUCTION

The utility of superplastic aluminum alloys in the aerospace and related industries need not be discussed in depth here, but clearly large weight and cost savings would be the potential benefit of a significant advance in this area of technology. Investigations have shown that several Al alloys containing Li are capable of being formed superplastically. Li combines the ability to lower density and increase strength, making it very attractive as an alloying addition. The maximum advantage in weight and cost savings would result from a combination of superplastic forming and the use of the lightest and strongest materials possible.

There are two different approaches to achieve superplastically formable alloys for structural components in the aerospace industry. The first involves the development of new alloys which exhibit superplastic response, with subsequent development for commercial applications; the second involves the development of superplastic properties in existing commercial alloys. Since Li-containing Al-based alloys are the subject of intensive commercial alloy development at present, it is possible through academic studies, such as those at NPS, to influence compositional and processing requirements of these alloy systems.

Al-Mg-Zr alloys containing 10 wt. pct. Mg were the first to be studied at NPS and much insight has been gained with respect to optimizing superplastic response through careful control of thermomechanical processing (TMP) parameters. As these alloys are essentially binary alloys, with only minor additions of Zr to stabilize the microstructure during casting and hot working, they are well suited to academic studies of the mechanisms involved in superplastic behaviour. More recently, two preliminary studies of Li containing Al-Mg-Zr alloys were undertaken. The first, by Oster (Al-8Mg-0.5Li-0.15Zr), considered the effects of warm rolling to 1.9 true strain which produced moderate superplasticity [Ref. 1]. The second, by Sanchez (Al-8Mg-0.5Li-0.15Zr), found that increasing the true rolling strain to 2.6 during TMP enhanced the superplastic response of the alloys at 300°C. The flow stress decreased by 25-40% over all strain rates, allowing peak ductilities in excess of 500% to be achieved. [Ref. 2].

The purpose of this thesis is to determine an optimum TMP to obtain maximum superplastic elongations in the same alloy system. The nominal compositions of the four alloys chosen for this study are given in Table 1.

TABLE 1  
NOMINAL ALLOY COMPOSITIONS

Alloy Designation *	Mg (wt. pct.)	Li (wt. pct.)	Zr (wt. pct.)	Al (wt. pct.)
8-1 2	8.0	0.5	0.25	balance
6-1	6.0	1.0	0.25	balance
8-1	8.0	1.0	0.15	balance
6-2	6.0	2.0	0.15	balance

\* refers to Mg and Li content, respectively (in wt. pct.)

Differential scanning calorimetry (DSC) will be used to aid in the choice of TMP temperatures for the various alloys and transmission electron microscopy (TEM) will be used to characterize the microstructure before and after superplastic deformation. In striving to achieve the goal of this research, it is hoped that new clues to understanding the superplastic phenomenon will be revealed.

## II. BACKGROUND

The non-heat treatable 5xxx series alloys are being used extensively in moderate-strength applications where good corrosion resistance is desirable. An example of this is the welded plate used in superstructures of naval vessels. These alloys have also found applications in missile structural components. The alloys 5083 (4.0-4.9 wt. pct. Mg) and 5456 (4.7-5.5 wt. pct. Mg) are the most widely available high-Mg alloys used commercially. Some typical mechanical properties of these alloys are listed in Table 2 where they are compared to the alloys used in this research.

TABLE 2  
COMMERCIAL AL-MG ALLOYS COMPARED TO LI-CONTAINING  
ALLOYS

Alloy	Density (g cm <sup>-3</sup> )	UTS (MPa)	Ductility (%)
5083-H321	2.66	317	16
5456-H321	2.66	352	16
8-1-2	2.57	448	12
6-1	2.54	-	-
8-1	2.52	413	10
6-2	2.45	-	-

The microstructural condition of these materials with respect to the working and tempering treatments highlights the important role played by Mg in imparting strength to 5xxx alloys. Since these alloys are not heat treatable, the desired mechanical properties must be achieved in the as-fabricated condition through a combination of solid solution strengthening and precipitation hardening. Research has been aimed at achieving the necessary mechanical properties in components fabricated using superplastic forming (SPF). Examples of the different types of Al alloys that have been processed to possess superplastic behaviour are given in Table 3.

TABLE 3  
EXAMPLES OF SUPERPLASTIC ALUMINUM ALLOYS

Alloy Type	Composition
solid solution	Al-5Mg Al-Mg-(Mn) (5456)
grain size stabilized, nominally single phase, solid solutions	binary Al-Mg-(Zr) ternary Al-Zn-Mg-(Zr) (7075)
two phase or multiphase alloys stabilized by a specific alloy addition	Al-Li-(Zr) Al-Cu-(Zr) (Supral) Al-Cu-Li-Mg-(Zr) (8090)

The Al alloys which are currently available as production quality SPF materials are based on the 7475, Supral and 8090 systems. In the case of 7475, superplasticity has been achieved by special TMP to refine microstructures utilizing a dispersion of fine particles. Supral alloys rely on dynamic recrystallization during forming to produce and maintain a fine grain size. The superplastic capability of 8090 is the result of the conversion to a fine-grained, recrystallized structure during superplastic straining.

## A. ALLOYING ELEMENTS

### 1. Magnesium

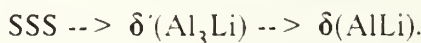
Magnesium, because of its high solubility, is one of the more common alloying elements added to Al. In addition to beneficial effects on the strength-to-weight ratio, it has been found to raise ambient temperature ductility and corrosion resistance as well as improve weldability [Ref. 3]. For the range of Mg contents considered in this research (i.e. 6 - 8 wt. pct.), it may be anticipated that the amount of Mg in solid solution will be at most 6.8 wt. pct. after warm working at 300°C. The remainder of the Mg in the alloys will be present as the  $\beta$  phase. This is an intermetallic compound based on  $Al_8Mg_5$  with a complex cubic structure ( $a = 2.82$  nm). The volume fraction of  $\beta$  phase then is expected to range from 0% for 6 wt. pct. Mg to 5% for 8 wt. pct. Mg at 300°C. This brittle phase forms preferentially at grain boundaries and triple points and reduces alloy ductility unless this tendency is controlled by grain refinement or other means. The density of this compound is 2.23 g cm<sup>3</sup> which indicates that,

when a substantial volume fraction is present, it will lead to considerable reductions in overall density. In fact, the density decreases linearly by 0.47% for every 1 wt. pct. Mg in solution and 0.5% for every 1 wt. pct. present as  $\text{Al}_8\text{Mg}_5$  [Ref. 4: p. 313].

Recent work on 8 and 10 wt. pct. Mg alloys concentrating on grain refinement has demonstrated an ability to sustain superplastic elongations. The important role played by Mg in superplasticity has been related to the morphology and distribution of the  $\beta$  phase precipitate [Ref. 5].  $\beta$  phase present as 1  $\mu\text{m}$  particles is able to stabilize the microstructure by processes as yet not fully understood. These relatively coarse  $\beta$  precipitates promote development of a substructure of a size approximately the same as the interparticle spacing and which evolves into a fine-grained structure.

## 2. Lithium

To date, not many commercial alloys with significant Li content are in service. This is despite the fact that alloying with Li would appear to be a nearly ideal technique for improving both strength and density properties of Al alloys. The reported density reductions are 3% per wt. pct. Li added [Ref. 6: p. 57]. This has proven to be less successful in practice mainly due to reduced fracture toughness and difficulties in adding Li to the Al during casting. Two principal causes for this have been identified. Firstly, the highly reactive nature of Li has meant that it is difficult to add to Al without introducing harmful quantities of contaminants such as Na, K, and S. These elements have little or no solubility in Al and may embrittle the matrix near the grain boundaries. Secondly, the shearable  $\delta'$  phase contributes to the problem by causing stress concentrations at the grain boundaries [Ref. 8: p. 18]. The solid solubility of Li in Al is less than 0.5 wt. pct. at ambient temperatures, rises to 1.6 wt. pct. at 300°C and, at the eutectic temperature of 600°C, it reaches a maximum of 4.2 wt. pct. The predominant strengthening effect of Li is precipitation hardening due to fine, evenly distributed  $\delta'$  particles. The Al-Li system has been found to have a precipitation sequence of

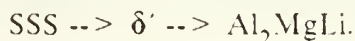


The metastable  $\delta'$  phase is an intermetallic compound of stoichiometry  $\text{Al}_3\text{Li}$  with a cubic structure (0.401 nm). Its low misfit (0.18%) with Al allows for coherent precipitation of a superlattice structure. A uniform distribution of fine spheroidal precipitates has the potential for imparting considerable strength to an alloy providing overaging does not occur. Overaging leads to  $\delta$  phase formation which adversely affects

mechanical properties through detrimental grain boundary effects. Studies by Sanders and Starke [Ref. 8: p. 2] have shown that, at concentrations greater than 1.7 wt. pct. Li, precipitation of  $\delta'$  cannot be prevented even with a cold water quench. On the other hand Fridlyander, et al. [Ref. 9] found that, with levels of Li less than 1.6 wt. pct., little or no evidence of  $\delta'$  was seen. This suggests a threshold value of approximately 1.6 wt. pct. Li content which separates two distinct precipitation sequences. In contrast, the  $\delta$  phase tends to precipitate on grain boundaries creating a precipitate free zone (PFZ) which is weaker than the surrounding matrix. This leaves the alloy susceptible to intergranular cracking.

### 3. Aluminum-Magnesium-Lithium Ternary System

As one might expect, the presence of the Mg reduces the solubility of Li in Al. Parson and Sheppard found that solid solution strengthening of Al-Li alloys is thereby enhanced by approximately 50 MPa per wt. pct. of Mg added [Ref. 10]. The precipitation sequence for the ternary has been determined to be



Working with several Al alloys containing approximately 3.5 wt. pct. Mg and 2.0 wt. pct. Li, they report that the ternary  $\text{Al}_2\text{MgLi}$  phase precipitated along grain boundaries, which severely reduced ductility in the material. The 6-2 alloy clearly has more than the minimum Li content needed to produce Li based precipitates, so it was anticipated that this alloy would behave in a true ternary fashion as described by Parson and Sheppard. However, the Al-Li phase diagram shows that, at the warm working temperature employed in this research, the solubility of Li is 1.6 wt. pct. Since this is the threshold discussed above, it is anticipated that alloys with less than this level of Li might display a different precipitation sequence than seen in the Al-Mg-Li ternary system. This is supported by previous work on the 8-1 and 8-1.2 alloys, where the primary second phase seen was  $\beta(\text{Al}_3\text{Mg}_5)$ . Since this implies that the Li has remained in solid solution and has not joined in the precipitation sequence, these alloys were considered quasi-binary alloys.

The well-known diffusion rate equation,  $D = D_0 \exp(-Q/RT)$ , can be used to estimate the relative rates of diffusion of the two elements involved in these alloys. The results of this calculation suggests that lithium diffuses in aluminum approximately five times faster than magnesium. This is an indication that lithium containing phases may precipitate more rapidly than phases containing magnesium and aluminum only.

#### 4. Zirconium

Zr is a common minor addition to Al alloys which acts as a stabilizer principally during casting and hot working. Large primary particles of  $\text{Al}_3\text{Zr}$  of approximately 5  $\mu\text{m}$  size can form during casting. Primary  $\text{Al}_3\text{Zr}$  is a non-coherent particle which has a tetragonal structure ( $a = 0.4015 \text{ nm}$ ,  $c = 1.732 \text{ nm}$ ) whereas the much finer secondary particles are cubic ( $a = 0.405 \text{ nm}$ ) and are also coherent. The primary particles can be sites for crack initiation and are obviously undesirable; thus care during casting is imperative. Mondolfo states that the effects of small Zr additions is to provide nucleation sites for the solidification of the Al matrix [Ref. 4: p. 414]. This permits a finer grain structure than otherwise possible in cast Al alloys. Ideally, the Zr forms a very fine spheroidal precipitate (20 - 100 nm) of  $\text{Al}_3\text{Zr}$  which is beneficial for microstructural stability during solidification. In addition, Gayle and Vandersande suggest that, in Al-Li-Zr alloys,  $\text{Al}_3\text{Zr}$  particles may act as nucleation sites for  $\delta'$  co-precipitation [Ref. 11].

### B. SUPERPLASTICITY

#### 1. Phenomenological Description

Although much progress has been made in recent years, the phenomenon of superplastic behaviour in metals is not yet fully understood. Many early researchers advanced theories which can be classified into two main categories, namely diffusion-dominated and dislocation creep mechanisms. Diffusion-dominated mechanisms are those which require the action of thermally-activated vacancy motion to provide accommodation strains during elongation, while dislocation creep theories require the movement of dislocations to perform this stress relieving function. More recently, both of these mechanisms have been cited as playing a role in superplastic deformation (SPD). The most generally accepted descriptions have, as a common feature, a power law relationship such as

$$\sigma = K \dot{\epsilon}^m \quad (\text{eqn 2.1})$$

where  $\sigma$  is the true stress,  $\dot{\epsilon}$  is the strain rate and  $K$  is a material dependent proportionality factor which accounts for such influences as temperature, diffusivity

and grain size effects [Ref. 12]. The parameter  $m$  is known as the "strain-rate sensitivity coefficient" and is defined as

$$m = \frac{d \ln (\sigma)}{d \ln (\dot{\epsilon})}. \quad (\text{eqn 2.2})$$

If we note that

$$\sigma = P/A$$

and

$$\dot{\epsilon} = 1/l (dl/dt) = -l/A (dA/dt)$$

then equation 2.2, after rearrangement, takes the form of

$$dA/dt = -(P/K)^{(1-m)} l (A^{(1-m)})^m \quad (\text{eqn 2.3})$$

where  $A$  is the cross sectional area,  $P$  is the load and  $l$  is the gauge length. This clearly demonstrates the dependance of necking on the strain-rate sensitivity coefficient. If  $m$  approaches 1, then the rate of change of the area will become independent of the current cross sectional area. This means that nonuniformities in cross sectional area will not become increasingly severe, leading to initiation of localized necking. It is this delaying of necking, in the absence of cavitation, which is termed superplasticity. Most superplastic alloys have  $m$ -values of 0.5 and it has become common for these values to be used to predict superplastic response. For this reason, the strain rate sensitivity coefficient is considered an important material parameter throughout the literature on superplasticity. For example, Hales et al. demonstrated a correlation between maximum  $m$ -value and elongation in the Al-Mg-Li system [Ref. 5]. One important assumption made in the above analysis is that the microstructural dimensions remain constant throughout deformation. This is usually seen as an inverse grain size dependence. It has been shown that the strain rate during SPD has a  $(\sigma d)^2$

dependence on the grain size [Ref. 13]. If grain growth occurs during straining, then the stress will have to adjust to maintain a constant strain rate. If the grain growth also is influenced by strain rate and temperature, then the apparent m-value obtained from experimental data may not reflect the underlying deformation process. Furthermore, some materials are found to have high m-values but low ductility and the reason is generally ascribed to cavitation leading to premature failure [Ref. 12: p. 1-3].

## 2. Microstructural Requirements

It is universally noted that a very fine microstructure is required to sustain SPD. This is achieved through a thermomechanical process all variations of which include a rolling step. This step introduces a very high dislocation density which provides the energy to drive a restoration process resulting in a fine structure. Also recovery processes differ from recrystallization processes in that they do not change the crystal orientation. Beginning with this recovered substructure, new grains form in one of two ways to produce the moderate to high angle boundaries required for SPD.

The first is 'discontinuous recrystallization' where new grains nucleate and grow as boundaries migrate through the matrix causing the grains to enlarge. These new grains would grow until the grain boundaries are prevented from further movement. Thus, to maintain a fine microstructure, it is important that the alloy has a means to retard boundary migration once the appropriate structural dimensions have been achieved.

The second recrystallization mechanism is referred to as 'continuous recrystallization.' This phenomenon does not involve the nucleation and growth of new grains but rather the 'in situ' evolution of the substructure created during the recovery process. Essentially it consists of a gradual increasing of the boundary misorientations to the point that they are at high enough angles to support grain boundary sliding, believed to be the dominant deformation mechanism in SPD.

## C. THERMOMECHANICAL PROCESSING

### 1. Alternative TMP

Many processing schemes, designed to produce the necessary structure in Al alloys, have been developed. One well-known program, involving the 7475 alloy, is that of Rockwell International. This process consists of solution treatment at 500°C followed by overaging at 400°C and then warm rolling at 200°C followed by a final recrystallization at 500°C. A point to note is the use of high temperature employed in all but the rolling process. This implies that the grain refinement is provided through a

discontinuous recrystallization process with new grains nucleating at primary second phase particles. Due to a fine dispersion of  $\text{Al}_3\text{Zr}$  particles, each new grain is limited in volume as its interaction with grain boundaries prevents additional growth. This material shows best superplastic properties at temperatures on the order of  $0.95T_m$  ( $516^\circ\text{C}$ ). Several variations on this process which make industrial implementation easier are also used but the modified procedure invariably concludes with a high temperature recrystallization at  $500^\circ\text{C}$ .

Another approach is used commercially to produce an alloy called Supral. This process requires large concentrations (0.4 wt. pct.) of Zr introduced prior to casting. This is a difficult (and proprietary) procedure because this represents 4 times the maximum solubility of this element even at the melting temperatures. The alloy is then subjected to a careful heat treatment to homogenize the structure without unduly coarsening the  $\text{Al}_3\text{Zr}$  precipitates. The final step prior to SPD is to cold roll the material, presumably to create a high dislocation density. During deformation the relatively large grained structure is transformed into a finer substructure by a dynamic recrystallization mechanism. Alloys processed in this manner require temperatures of  $460^\circ\text{C}$  for best SPD and again the  $\text{Al}_3\text{Zr}$  is the phase which stabilizes recrystallized grain boundaries.

## 2. NPS Procedure

While the goal of a refined microstructure is the same, the NPS approach is unique in several respects. The homogenizing step consists of solution treatment at  $500^\circ\text{C}$  followed by upset forging and a further solution treatment for 1 hour at  $500^\circ\text{C}$ . The principal feature of this TMP is the warm rolling at  $300^\circ\text{C}$ . This process does not include a recrystallization or aging heat treatment step but relies on microstructure development during rolling and SPD. The critical variables in this process are discussed in greater detail in the following sections.

## 3. Warm Rolling Temperature

Extensive research has shown that microstructural development capable of supporting superplastic deformation (SPD) can be achieved in high-Mg content Al alloys by warm rolling at  $300^\circ\text{C}$ . The notable feature of this TMP is that it occurs just below the  $\beta$  phase solvus temperature, thereby permitting simultaneous precipitation of the second phase while the rolling introduces large numbers of dislocations. TEM studies of as-rolled material have consistently shown a very high dislocation density which completely obscures the original grain structure or any underlying substructure.

#### **4. Reheating Time Between Rolling Passes**

Investigations by Wise [Ref. 14] and Stewart [Ref. 15] were very successful in isolating the effects of altering several TMP variables in these high-Mg alloys. The studies included warm rolling with reheat time between passes of 4 and 30 minutes. Stewart concluded that the longer reheat time between passes lead to improvement in the elevated temperature ductilities. Further work has suggested that this is due to better development of boundaries with moderate misorientations when reheating time is greater [Ref. 5].

#### **5. Reduction Per Rolling Pass**

Wise discovered that a decrease in ductility resulted from a larger reduction per rolling pass; however, Stewart learned that a large reduction per pass could be beneficial if the reheating time between passes is extended. This is believed to be the result of a significant increase in the number of dislocations introduced due to the more severe local straining. The recovery rate of the dislocations to the newly formed subboundaries depends on elevated temperature which, as discussed above, must not exceed the  $\beta$  solvus temperature. This suggests the longer reheating time is permitting the larger number of dislocations to recover to the subgrain boundaries, thereby increasing boundary misorientation angles beyond the critical value required for GBS to occur [Ref. 16]. This would also explain why Wise saw reduced ductilities with larger reductions per pass. The higher density of dislocations within the substructure was not able to recover to boundaries and resulted in strain hardening of the material.

#### **6. Total Strain**

It has been consistently demonstrated that increasing the total true strain improves the superplastic response. Wise nearly doubled the elongations attained when rolling the 10-0 alloy to a 2.5 total strain as compared to results obtained when rolled to only 1.5 strain [Ref. 14: p. 32-38]. Stewart was able to show that the advantages of increasing the total rolling strain were more pronounced for samples which experienced longer total time at the rolling temperature. This is further evidence that a recovery mechanism is responsible for microstructural development leading to superplastic response.

### **D. DIFFERENTIAL SCANNING CALORIMETER**

The differential scanning calorimeter (DSC) is an instrument used to detect changes in the heat capacity of a test sample. This is done by heating (or cooling) a

specimen and a reference sample under the same controlled conditions and measuring the difference in power requirements. A schematic of the DSC apparatus used in this investigation is shown in Figure 2.1. If a test sample requires less power input than the reference to maintain a given heating rate, it implies that an exothermic reaction is occurring within the microstructure. This can be employed to assist in determining solid solution solvi of phases in Al alloys.

It is often very difficult to characterize the microstructure of Al alloys using TEM. The DSC offers a quantitative means for assessing the precipitation sequence in these alloys. Much information can be gleaned from DSC analysis, but this work has centered on determining phases present and corresponding solvus temperatures. A review of the Al-Li phase diagram in Figure 2.2 shows that, when Li content is between 0.5 and 2.0 wt. pct., the solvus for the equilibrium  $\delta$  phase is between 225 and 375°C. The metastable  $\delta'$  phase solvus would be 150°C for 0.5 wt. pct. and up to 230°C for 2 wt. pct. Li. These temperatures must be assumed to represent minimum values since the addition of Mg reduces the solubility of Li in Al thereby increasing these solvus temperatures.

For a binary Al-Mg alloy, the phase diagram of Figure 2.3 shows a  $\beta$  solvus temperature of 280°C for 6 wt. pct. and up to 310°C for 8 wt. pct. Mg content. The addition of Li to the alloy might be expected to raise these solvi also. Figure 2.4 is a view of the Al-Mg-Li ternary diagram which clearly shows that, when Li content is low, the phase expected is the  $\text{Al}_8\text{Mg}_5$  phase. At higher Li content levels, the equilibrium phases become the matrix and  $\text{Al}_2\text{MgLi}$  phase. As discussed previously, this Li level was expected to be approximately 1.6 wt. pct.

Working with binary Al-2.5 wt. pct. Li alloys, Papazian, Sigli and Sanchez found endothermic peaks at 125, 300 and 490°C during heating [Ref. 17]. The low temperature peak remains controversial but is frequently explained as the dissolution of Guinier-Preston (GP) zones. The authors conclude that  $\delta'$  dissolution is represented by the 300°C peak and the equilibrium  $\delta$  phase is the remaining peak. Research by Rioja and Ludwiczak on the alloy 2090 (Al-Mg-Li-Cu) showed endotherms at 120, 250, and 450°C [Ref. 18]. Again no concrete determination of the low temperature peak could be made, but  $\delta'$  and equilibrium phase dissolution were identified as causes of the higher temperature peaks respectively.

Working with the 10-0 alloy, Stewart found peaks in the heat capacity versus temperature curves between 360 and 385°C. These peaks were all the result of  $\beta$  phase

## DSC SCHEMATIC

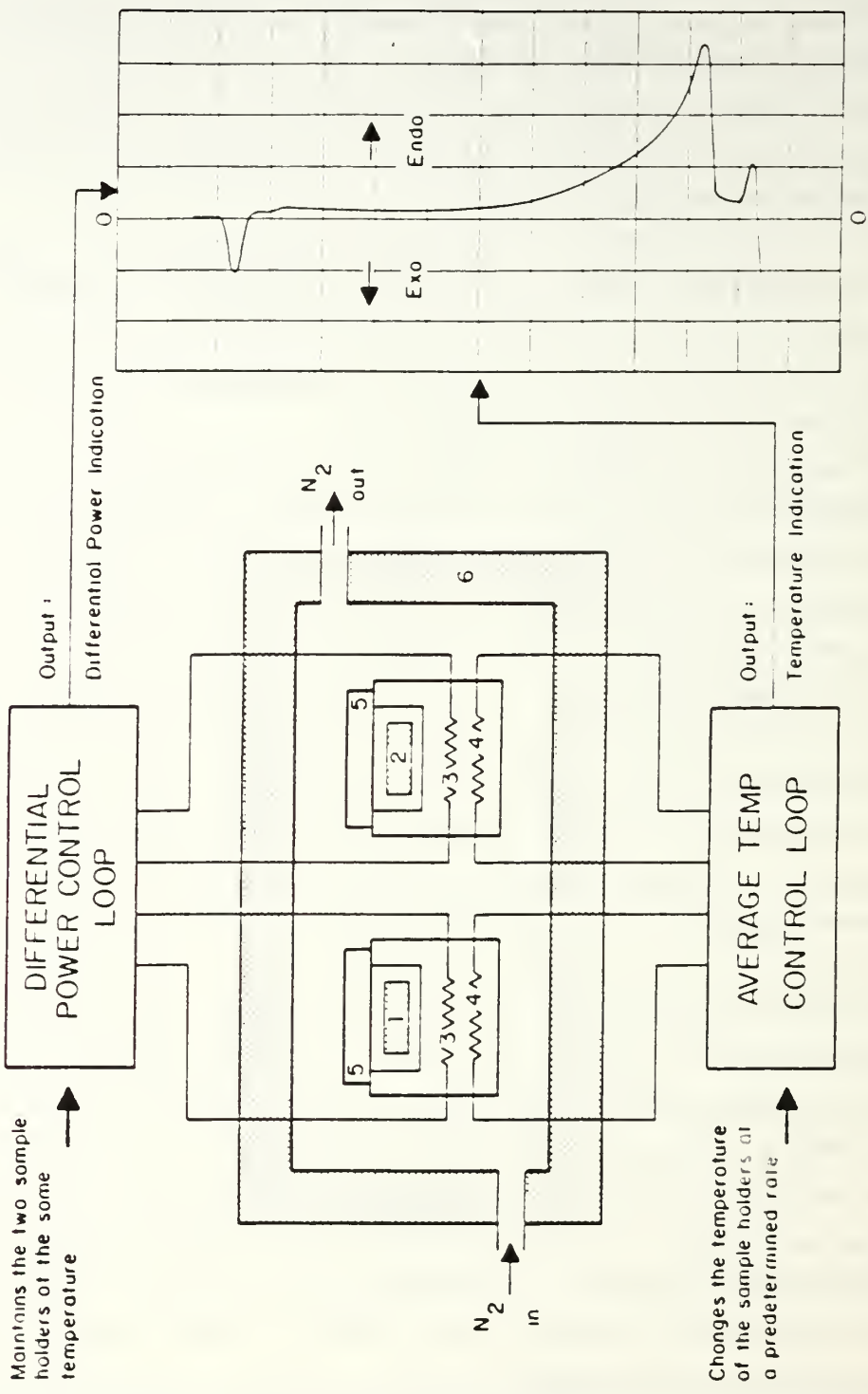


Figure 2.1 DSC Apparatus Showing Theory of Operation

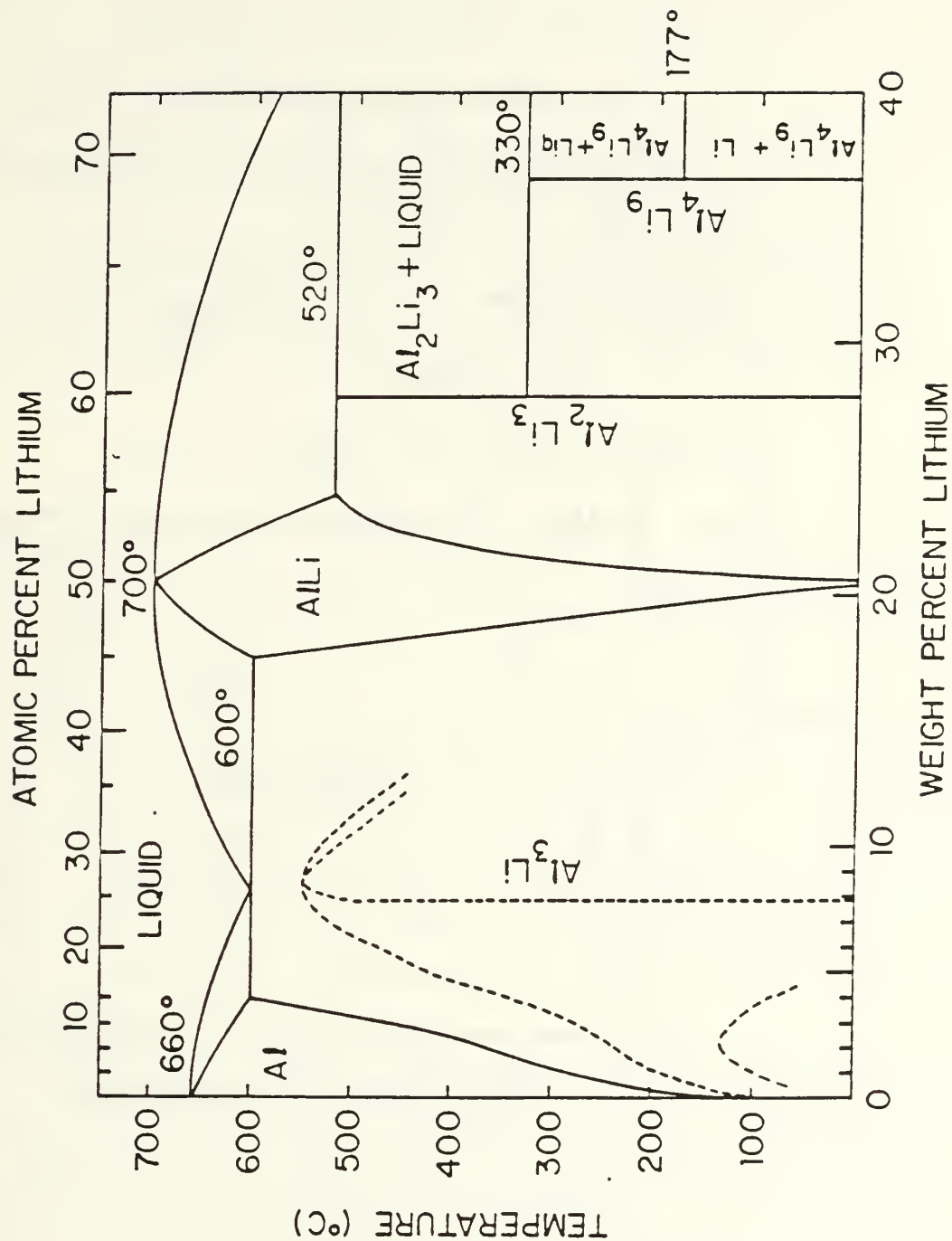


Figure 2.2 Aluminum-Lithium Binary Phase Diagram

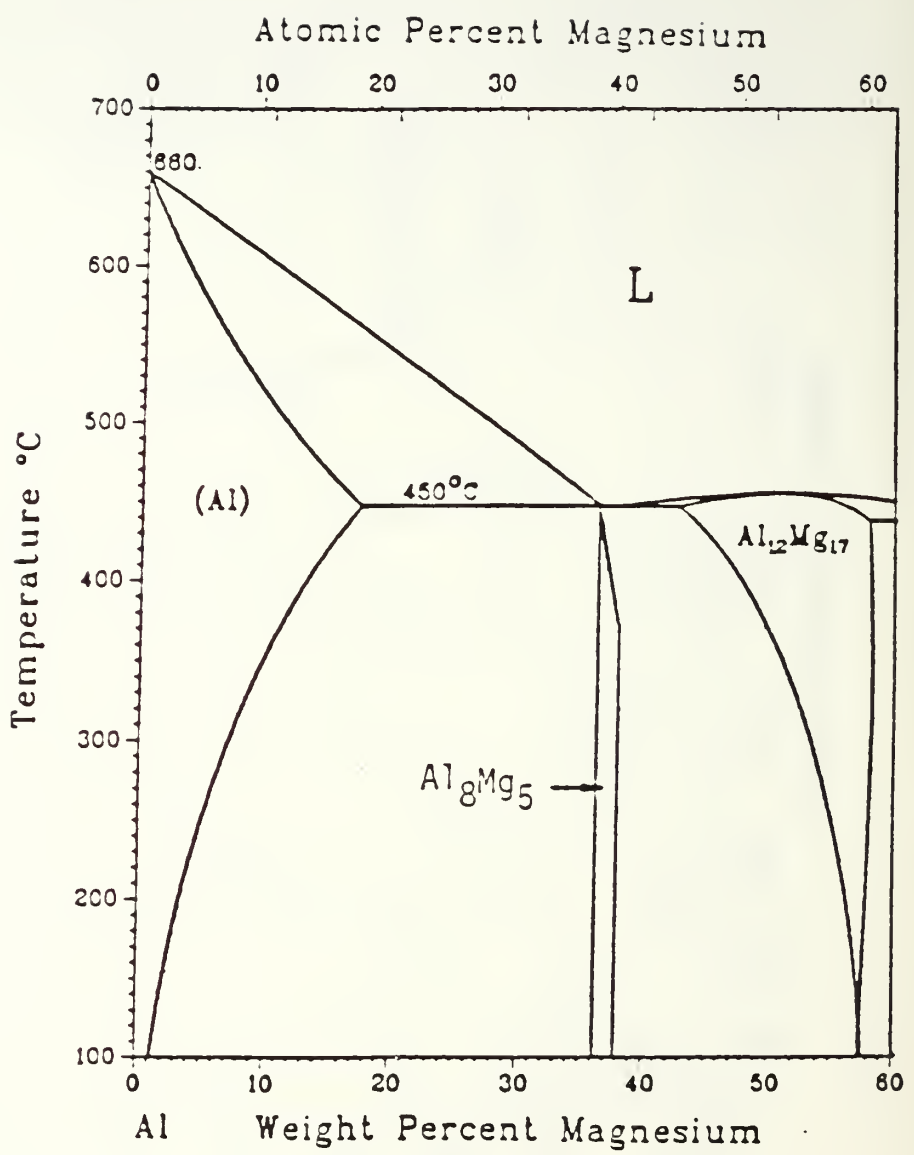


Figure 2.3 Aluminum-Magnesium Binary Phase Diagram

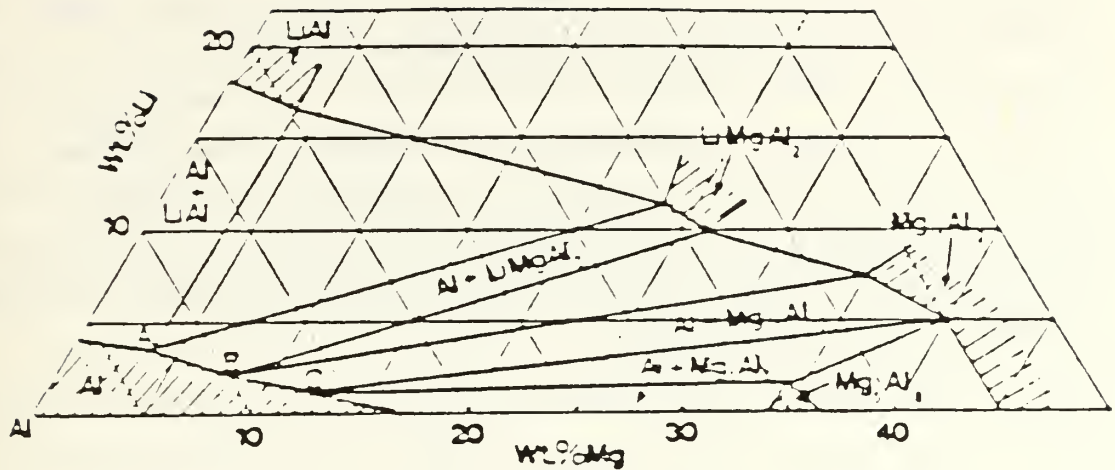


Figure 2.4 Al-Li-Mg Ternary Phase Diagram at 425°C

dissolution and were seen to vary over this temperature range as a function of changing TMP parameters. It is speculated that this variation is due to a change in morphology of the precipitate following the warm rolling, which causes the precipitate to be more stable.

Care must be taken when interpreting DSC data due to peak temperature shifts caused by variations in the material being examined. For example, as volume fraction of a phase increases, the corresponding DSC peak maximum will shift to a higher value. Similarly, if the stability of the precipitate were to increase, the DSC peak would shift to a higher temperature reflecting the higher thermal energy required to return the phase to the solid solution. Finally, if the precipitate average size is coarser, it would have the same effect as increasing stability and force the peak to appear at a higher temperature.

One of the practical difficulties involved in the use of the DSC is the need to establish a baseline heat capacity. The measured value required is the heat capacity of the test sample as compared to an ideal sample which has no phase transformations taking place within the microstructure. Stewart developed a successful technique of cycling the sample through the temperature range a second time after the second phase had been returned into solid solution and using the corresponding DSC trace as a baseline. To be more certain of the validity of this approach the sample was cycled a third time in order to establish that, within experimental limits, the second and third

traces were the same. Other research has determined that the use of pure Al samples positions a baseline for use with subsequent test samples; however, sample mass is critical in such tests and thus is only valid if the pure Al standard and the test sample are of the same mass. The effects mentioned above, on the positions of DSC peak maxima with respect to the solvi of the corresponding phases returning to solid solution, dictate that there will always be an element of experimental uncertainty. However, correlating the results of Stewart on the 10-0 alloy with the TMP temperatures used allows for a reasonably accurate determination of processing temperatures for the present alloys.

### III. EXPERIMENTAL PROCEDURE

#### A. DIFFERENTIAL SCANNING CALORIMETRY

Calorimetric measurements were made using a Perkin-Elmer DSC-2C machine equipped with a paper chart recorder in a manner similar to that employed by Stewart [Ref. 15: p. 24]. Samples were prepared by sectioning a thin wafer from the center of the material and obtaining a 3 mm diameter disc using a through hole punch. These samples were placed into an aluminum pan and covered with an aluminum lid before being positioned into the sample holder of the DSC. Since the discs were small, ranging in mass from 3.5 - 6.0 mg, an empty aluminum pan and lid were used as a reference. The same reference and sample pans and lids were used throughout the experiment. All runs were performed at a heating rate of 40 K min to permit direct comparison of results.

Table 4 shows the materials and heat treatments tested in the DSC. At least three samples of each case were examined and, as in Stewart's work, the baseline heat capacity of each sample was assumed to be defined by the third heating cycle. Difficulties with this approach arose when studying the 6-2 alloy because large endothermic peaks existed on all traces. In this case, runs with pure aluminum samples of approximately the same mass were used to define a baseline. Pen deviation from baseline was then used to produce heat capacity versus temperature plots. DSC calibration, operation and data reduction are explained further in appendix A.

#### B. THERMOMECHANICAL PROCESSING

The TMP employed was similar to those processes achieving best results in high magnesium alloys, with only hot working temperatures altered slightly because of the Li content. Forging billets with approximate dimensions of 2.6 x 2.6 x 8 cm were machined from the as-received ingots. Each billet was heated at 440°C for 8 hours before solution treatment at either 480°C (8 wt. pct. Mg) or 500°C (6 wt. pct. Mg) for 16 hours. This was followed by upset forging for all alloys at 480°C plus an additional hour at the solution treatment temperature prior to a cold water quench. Each forging billet was then cut in half to form 2 rolling billets.

TABLE 4  
ALLOY CONDITIONS AS TESTED IN THE DSC

Alloy	Heat Treatment
8-1 2	rolled 300°C + 1hr 300°C
8-1 2	rolled 300°C + 1hr 300°C + 72hrs 120°C
8-1 2	rolled 300°C + 1hr 300°C + 72hrs 150°C
8-1	rolled 300°C + 1.3hrs 300°C
8-1	rolled 300°C + 1.3hrs 300°C + 72hrs 75°C
6-1	hot forged 480°C + 5hrs 300°C
6-2	hot rolled 480°C + 5hrs 300°C

All but the 6-2 alloy were then warm rolled at 300°C using a reduction of 2.5 mm per rolling pass and a reheating time of 30 min. between passes. Rolling was done to a final total true rolling strain of 2.45 to 2.8 and the rolling billet was cold water quenched immediately after the final pass. Figure 3.1 shows the TMP schematically and Table 5 lists the conditions for each alloy. The 6-2 alloy had shown a much different structure in the DSC investigation and thus it was decided to warm roll it at 350°C. The rolling was not successful and so a billet was rolled at 300°C and another at 380°C in an effort to improve results, again without success. It was decided to halt efforts on this alloy pending further study.

### C. ELEVATED TEMPERATURE TESTING

Specimens for use in the elevated temperature tensile tests were machined from the rolled billets using the geometry which has become the standard for such tests at NPS and which permits direct comparison of results between researchers. All specimens were oriented with the gauge section parallel to the billet rolling direction. The sample dimensions are shown in Figure 3.2 .

The testing was performed on a calibrated Instron tensile testing machine fitted with a 1000 lb load cell. Special grips and hardware for use at high temperature were employed to mount the samples in the Instron. Elevated temperatures were achieved through the use of a temperature controlled three-zone clamshell furnace.

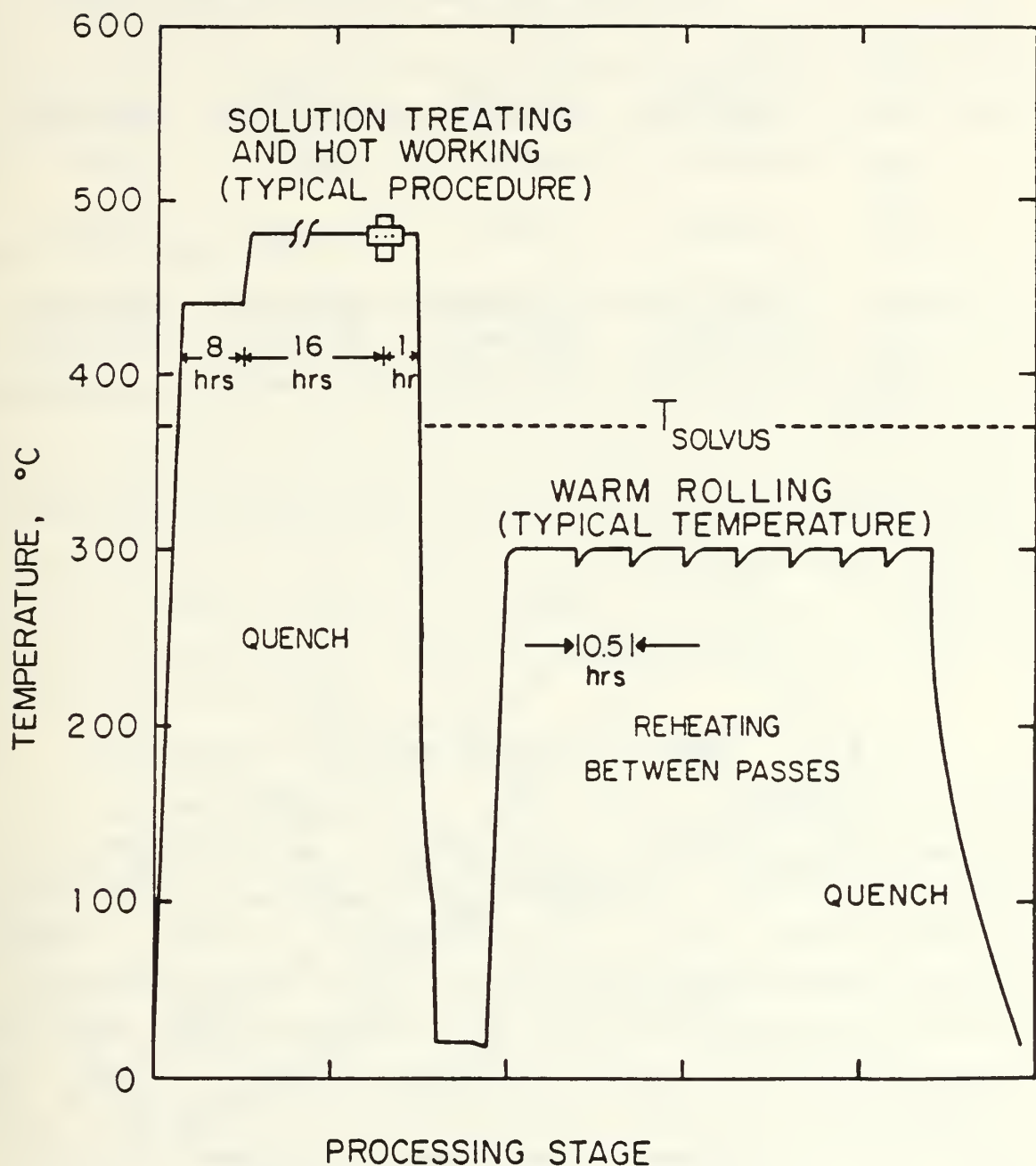


Figure 3.1 NPS Thermomechanical Processing Procedure

TABLE 5  
TMP VARIABLES FOR EACH OF THE ALLOYS STUDIED

Alloy	8-1.2	8-1	6-1	6-2
sol'n treat	8hrs 440°C 16hrs 480°C	8hrs 440°C 16hrs 480°C	8hrs 440°C 16hrs 500°C	8hrs 440°C 16hrs 500°C
upset forge	480°C	480°C	480°C	480°C
sol'n treat	1hr 480°C	1hr 480°C	1hr 500°C	1hr 500°C
rolling	2.5mm pass 300°C w 30 min reheat	2.5mm pass 300°C w 30 min reheat	2.5mm pass 300°C w 30 min reheat	2.5mm pass 350°C w 30 min reheat
tensile testing	275 - 350°C	275 - 350°C	275 - 350°C	not performed

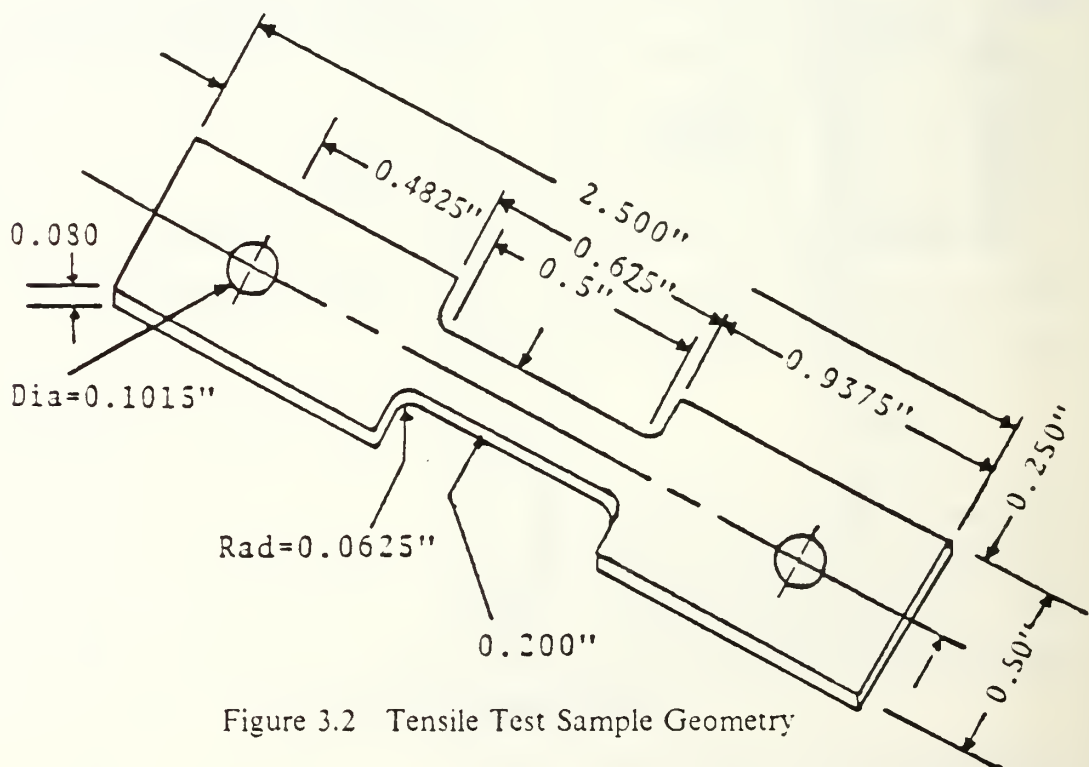


Figure 3.2 Tensile Test Sample Geometry

Thermocouples were installed to monitor sample temperature during testing and the furnace was sealed with insulation to maximize heating rate and to minimize temperature gradients.

Both the 6-1 and 8-1 alloys were tested at five strain rates between  $6.67 \times 10^{-5}$  sec $^{-1}$  and  $6.67 \times 10^{-2}$  sec $^{-1}$  at temperatures of 275, 300, 325 and 350°C in order to determine the optimum superplastic forming conditions. A billet of the 8-1 2 alloy, previously investigated by Sanchez, was prepared using the same TMP scheme as employed in this research. This alloy was then tensile tested at the same strain rates as above but only at 300°C. This data was required to isolate the one changed variable from Sanchez's work, which was a longer reheat time between rolling passes.

#### D. DATA REDUCTION

A description of the data reduction procedure for the DSC experiments is contained in Appendix A. Elevated temperature tensile test data reduction was conducted as described by Alcamio [Ref. 19]. Scribe marks were placed 1.27 cm (0.5 in.) apart on the gauge section of each specimen prior to testing. Subsequent to the test, the separation of these marks was used to determine percent elongation. The load versus time data was sampled and a computer data file created from which true stress versus true strain curves were calculated, using a simple fortran program, and then plotted and included in Appendix B. These graphs in turn were used to produce flow stress versus strain rate curves at 0.1% true strain. From these plots the strain rate sensitivity ( $m$ ) was determined.

#### E. TRANSMISSION ELECTRON MICROSCOPY (TEM)

To assess the microstructure of the alloys, TEM was utilized on a selected number of tensile specimens. TEM foils were extracted from gauge section specimens as close to the point of fracture as could be realized. In the case of the 8-1 specimen deformed at  $1.67 \times 10^{-2}$ , where elongation was so extreme, a second specimen was tested and the cross heads stopped when the measured elongation was 401%. Grip foils were obtained from that portion of the grip furthest from the gauge section where the effects of strain on the microstructure would be minimized. A JEOL-120CX operating at 120kV was used to view the foils. Conventional bright field (2-beam) imaging was utilized for microstructural characterization and weak-beam ( $g \cdot 3g$ ) dark field imaging for studying dislocation structures. TEM was also used to evaluate the microstructure of the 6-2 alloy which could not be processed. Foils were prepared from material in the as rolled state as well as after a 1 hour anneal at 300°C. Standard foil preparation techniques were employed to produce TEM specimens with foil normals perpendicular

to the rolling plane. A solution of 20% HNO<sub>3</sub> in methanol with an applied potential of 15V at a temperature of -20°C was utilized in a 'Struers Tenupol' system.

## IV. RESULTS

### A. DSC

#### 1. Al-8 wt. pct. Mg-0.5 wt. pct. Li

In order to use DSC data to design TMP, particularly with respect to temperature selection, samples of the 8-1.2 alloy were investigated. The superplastic response of this alloy following the well established TMP parameters was documented by Sanchez. The samples were taken from material after warm rolling at 300°C, 2.5 mm reduction per pass, and 4 min. reheat time between passes, followed by a 1 hour anneal at 300°C to approximate the conditions expected at the onset of deformation. The DSC trace is shown in Figure 4.1. The curves had a distinct and consistent peak in heat capacity at about 360°C. The traces depart from zero at approximately 300°C and return to near zero at a temperature of 400°C. From previous work we know this peak to be due to the dissolution of the  $\beta$  phase. The traces show no evidence of any other phases affecting the heat capacity in the temperature range of these tests.

#### 2. Al-8 wt. pct. Mg-1 wt. pct. Li

The 8-1 alloy was prepared for DSC testing by first undergoing a homogenization procedure at 480°C and then a 1 hour anneal at 300°C and then tested in the same manner as for 8-1.2. The results of these tests are shown in Figure 4.2. Clearly the trace is of the same form but we can see that the peak occurred at a slightly higher value of heat capacity. This may be indicative of a higher volume fraction of the second phase in this alloy than in the previous material. The peak showed some broadening in temperature range but interestingly the peak value was, within the limits of experimental error, at the same temperature as observed in the 8-1.2 samples.

#### 3. Al-6 wt. pct. Mg-1 wt. pct. Li

Preparation of the 6-1 alloy for DSC testing also involved a high temperature homogenization procedure at 480°C followed by aging at 275°C for 5 hours and furnace cooling. This was designed to precipitate the maximum possible volume fraction of the equilibrium precipitate from solution during cooling. The results of the calorimetry are displayed in figure 4.3. Once again the peak heat capacity appeared at 360°C and the peak limits were similar to the previous alloys, the one difference being

the relatively small peak value. The similarity of this trace to the others shows that 6-1 alloy also precipitated  $\beta$  phase, although possibly in reduced amounts, while no evidence of additional phases was found.

#### 4. Al-6 wt. pct. Mg-2 wt. pct. Li

The heat treatment given the 6-2 prior to DSC evaluation, with the exception of slightly longer homogenization times, was identical with that used for 6-1. Upon testing this alloy, it was immediately evident that a different series of reactions was taking place because two new peaks appeared which were not evident during the first run. One result of this was that the procedure for determining a baseline would have to be modified for this alloy. Using a series of pure aluminum samples with masses approximately equal to those to be tested, a series of traces were made which were then employed to determine the baseline heat capacity. The plots for the first run are shown at Figure 4.4 and for the third run at Figure 4.5. The first run showed a large endothermic peak at approximately  $400^{\circ}\text{C}$ . The trace rises above zero near  $230^{\circ}\text{C}$  and remains above zero to a temperature above  $440^{\circ}\text{C}$ . The abrupt temperature shift and increase in size when compared to previous data indicate it is not due to  $\beta$  phase. The large size would indicate the phase it represents is present in relatively large volume fraction and, because it resulted from a furnace cooling procedure, it must be assumed it is an equilibrium phase. Mondolfo states that the equilibrium phase expected for this alloy is  $\text{Al}_2\text{MgLi}$ . The trace of sample 1 shows a small additional endothermic peak which might be indicating the presence of  $\text{Al}_{12}\text{Mg}_{17}$ . This appears on only one trace, possibly because of concentration variations within the alloy, sample mass being only on the order of 5 mg.

The second and third runs performed on samples of this alloy showed the presence of two additional endothermic peaks and one exothermic peak. Since the nominal cooling rate in the DSC was  $320^{\circ}\text{C}$  per minute, it is clear that the kinetics for the dissolution and precipitation of these phases are very fast. Since alloys containing more than 1.6 wt. pct. Li are known to be quench rate sensitive and to precipitate  $\delta'$ , this suggests that the large peak at  $240^{\circ}\text{C}$  is due to this phase. Comparison of these traces with that for 7075 alloy also confirms this hypothesis. Several authors, including Papazian, report an endothermic peak similar to that appearing at  $160^{\circ}\text{C}$  [Ref. 17]. While some uncertainty as to the source of this peak still remains, most have concluded that it is due to GP zones. The exothermic peak seen on the second and third runs at  $350^{\circ}\text{C}$  appears to result from the precipitation of the  $\text{Al}_2\text{MgLi}$  phase from

AL-8%MG-0.5%LI

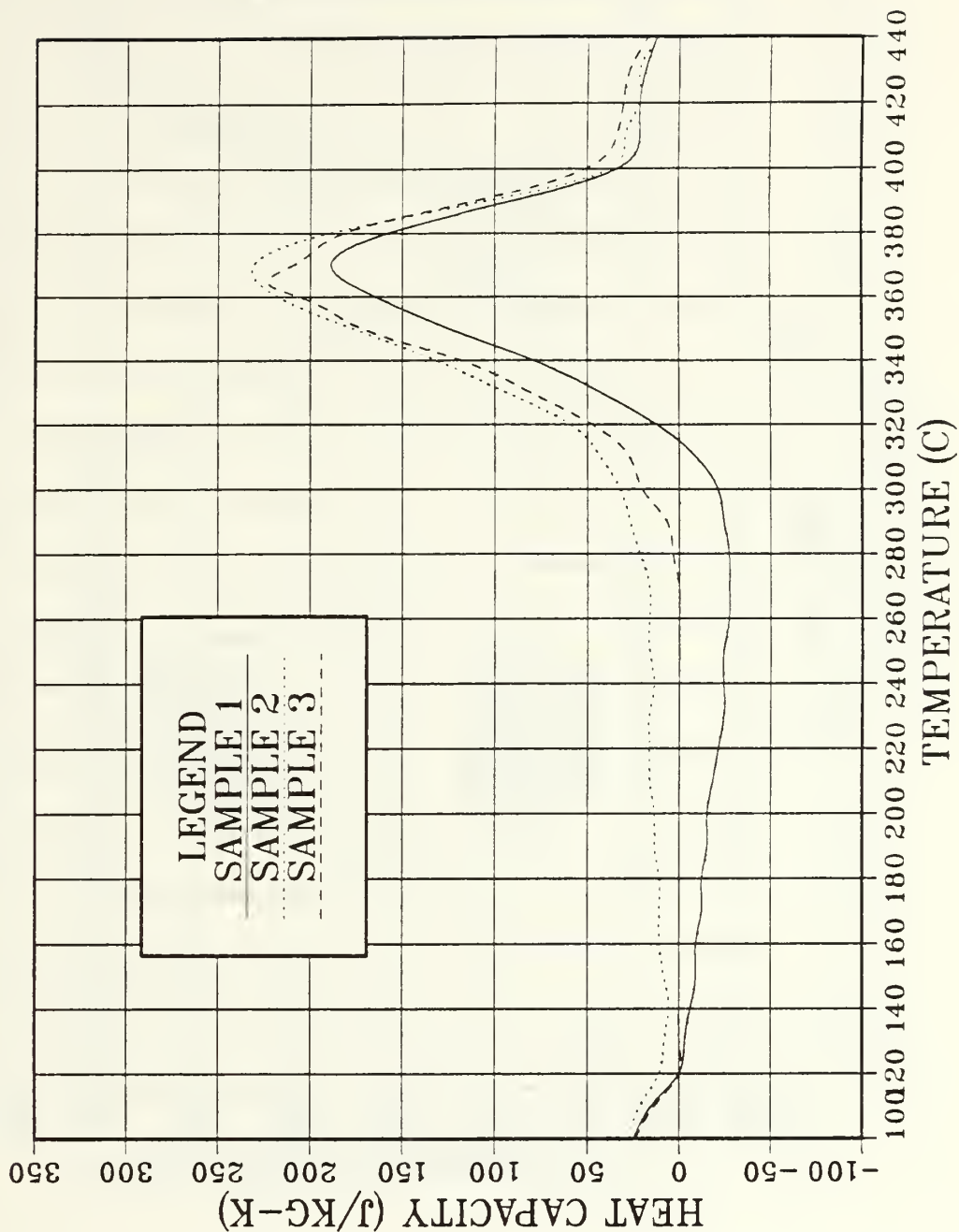


Figure 4.1 DSC trace for the 8-1/2 alloy

AL-8%MG-1%LI

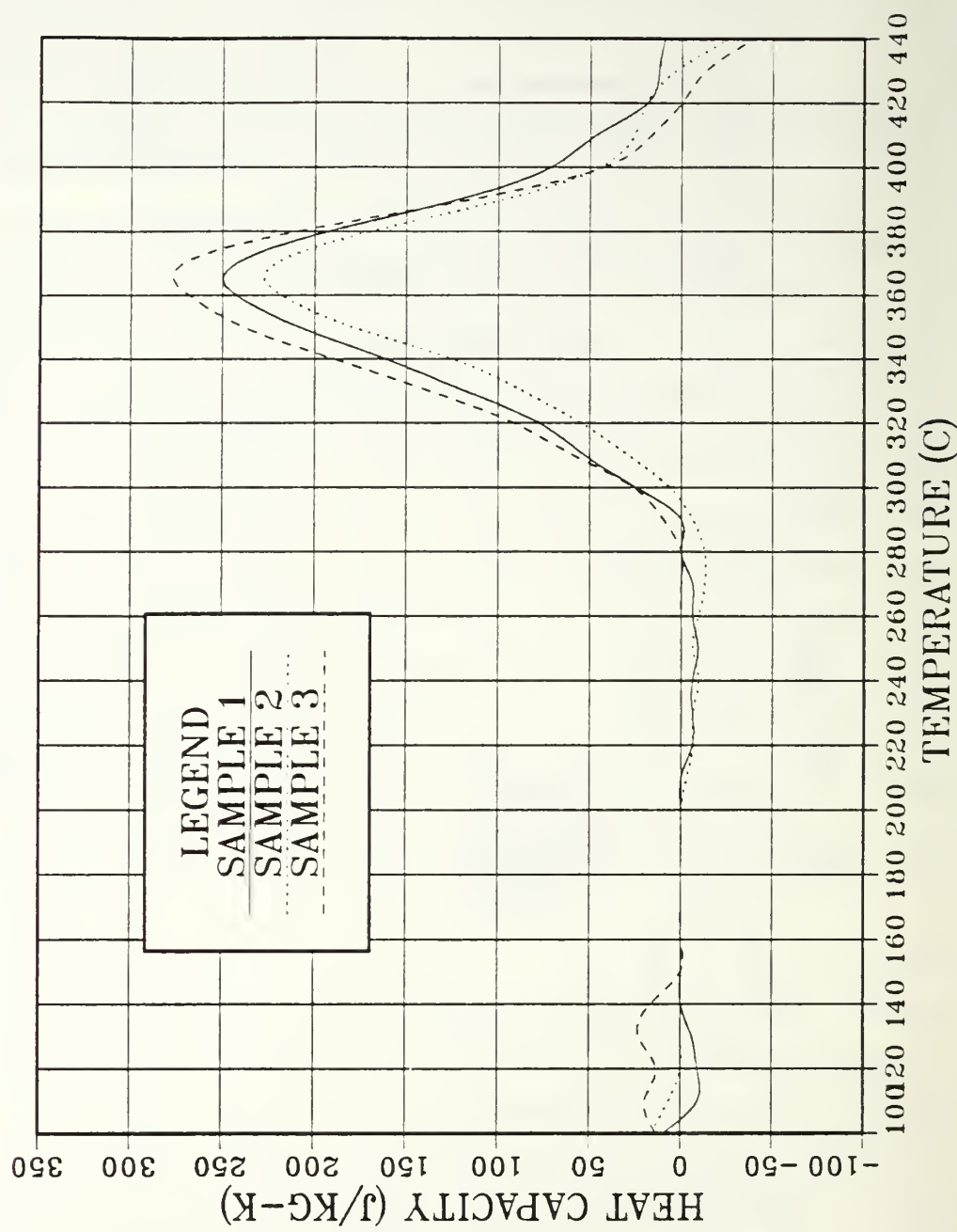


Figure 4.2 DSC trace for the 8-1 alloy

# AL-6%MG-1%LI

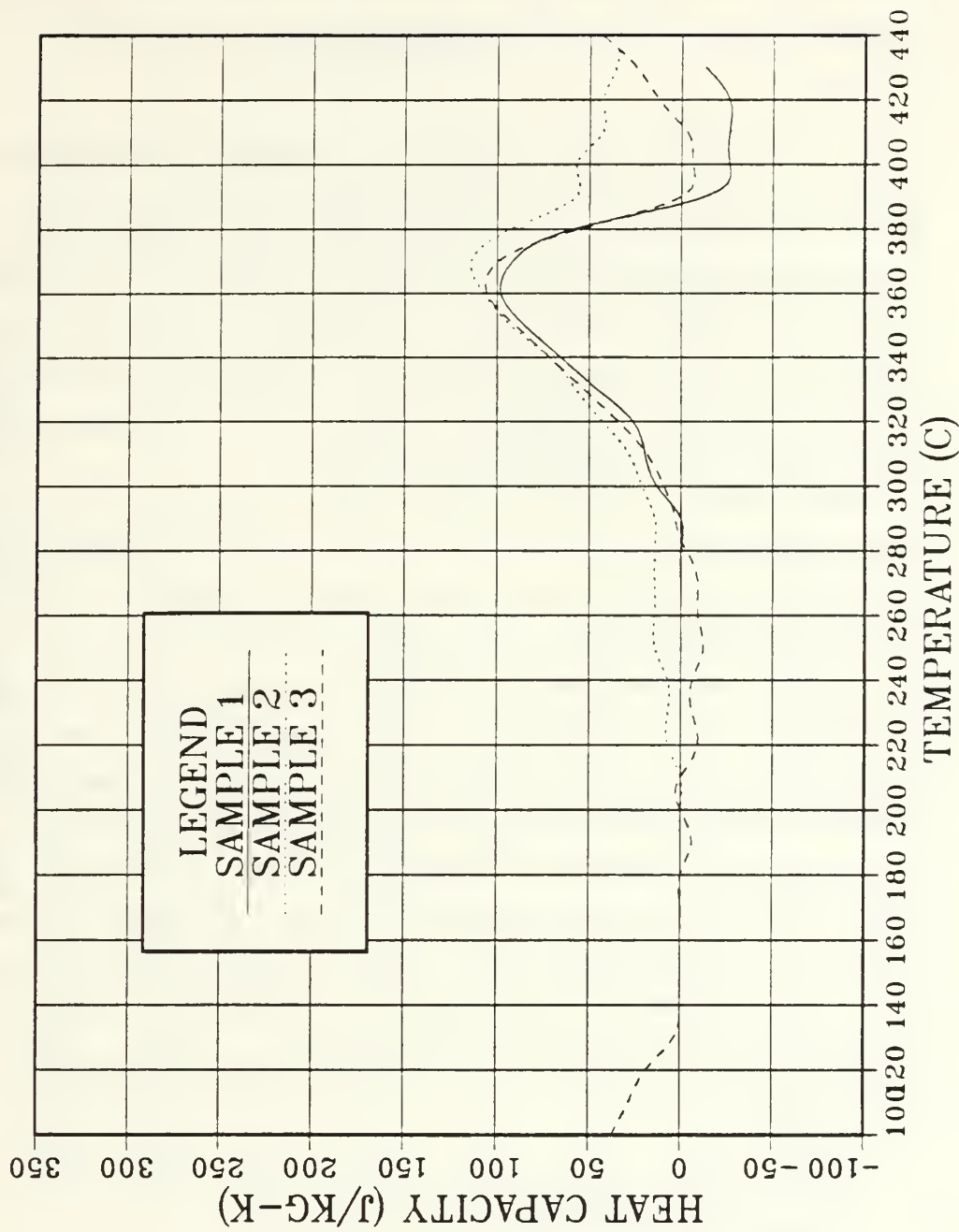


Figure 4.3 DSC trace for the 6-1 alloy

the supersaturated solid solution created by  $\delta'$  dissolution prior to its subsequent dissolution. This phenomenon is observed in other alloys such as 2090 although the equilibrium phase involved is not  $\text{Al}_2\text{MgLi}$  [Ref. 18].

## B. TMP

The aim of the DSC experiment was to optimize grain refinement and thus superplastic response through careful control of the TMP parameters. The rolling parameters involving total strain, reduction per pass, and reheat time between passes have all been previously established through the work of Sanchez, Oster and Stewart. In light of the results from the 8-1 2 studies and a comparison with DSC traces obtained here, it would appear that the best TMP temperature is located approximately 60°C below the  $\beta$  Peak. The similarity of the 8-1 and 6-1 DSC traces dictates that the same temperatures be employed for these materials.

This is clearly not the case for the 6-2 alloy. Using the same criterion, we would choose a higher temperature for TMP of this alloy. If it is assumed that the  $\text{Al}_2\text{MgLi}$  phase plays the same role as the  $\beta$  phase during warm working, then the best rolling temperature based upon DSC considerations would be 350°C.

The DSC evidence points to a successful homogenization of the alloy and, since no difficulties were experienced in upset forging, it must be concluded that inhomogeneities were not present. However, on warm rolling, difficulties were experienced. Alligatoring and edge cracking were both observed. A review of the DSC data showed that a window of temperatures was available which would both retain  $\text{Al}_2\text{MgLi}$  and leave all other precipitates in solution. The range of temperatures was determined to be approximately 300 - 380°C and thus a sample was warm rolled at each of these temperatures. The cracking persisted and it was decided to halt the processing of this alloy and perform TEM experiments in an effort to better understand these difficulties.

## C. MECHANICAL PROPERTIES

### 1. Matrix of Experiments

To allow comparison to earlier work, elevated temperature tensile tests were performed at 300°C over a series of 5 strain rates ranging from  $6.67 \times 10^{-5}$  to  $6.67 \times 10^{-2}$ . The range of strain rates was necessary because previous work indicates that maximum elongations for various superplastic alloys occur at points which are very

## AL-6%MG-2%LI (RUN 1)

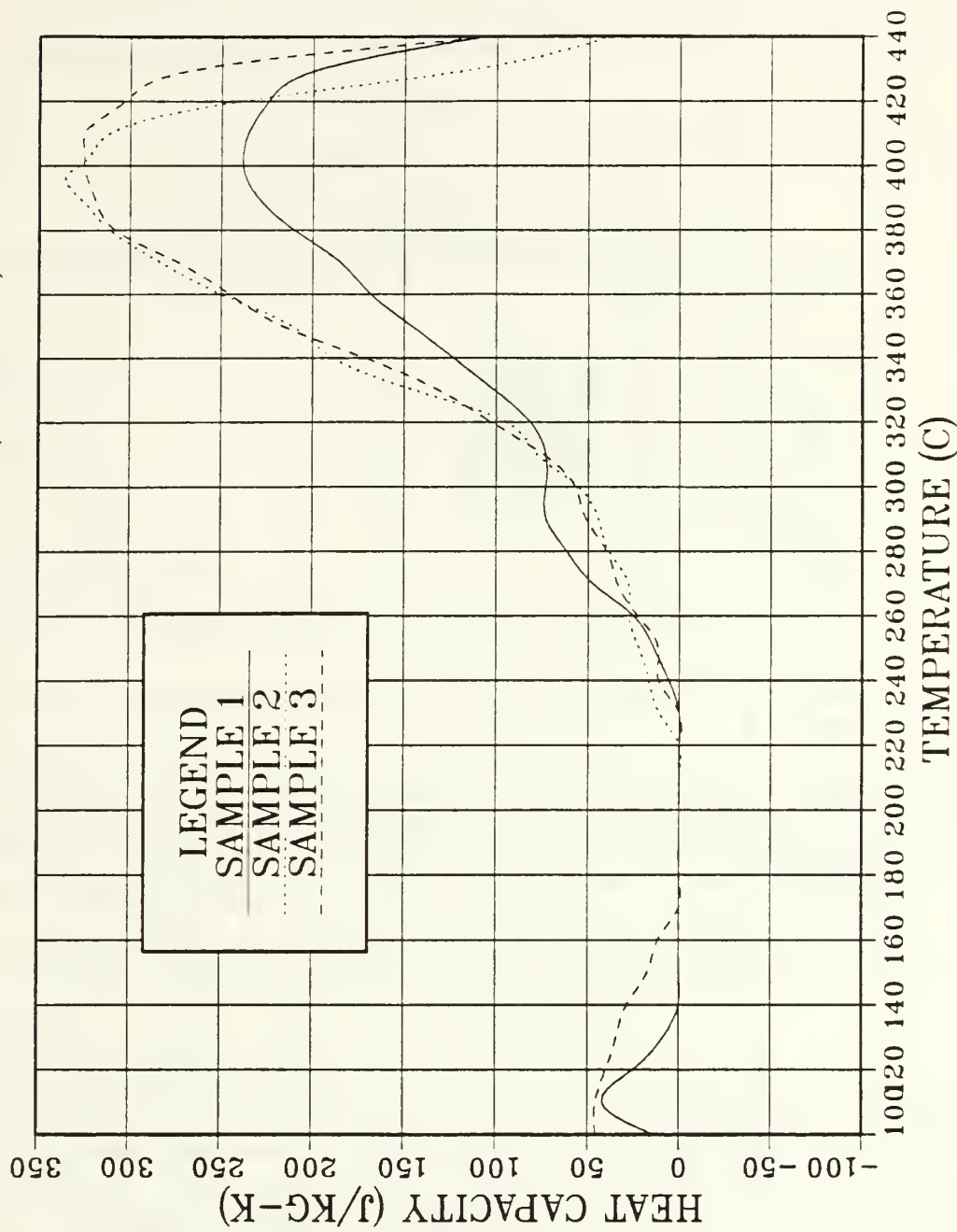


Figure 4.4 DSC trace for the 6-2 alloy (1st run)

### AL-6%MG-2%LI (RUN 3)

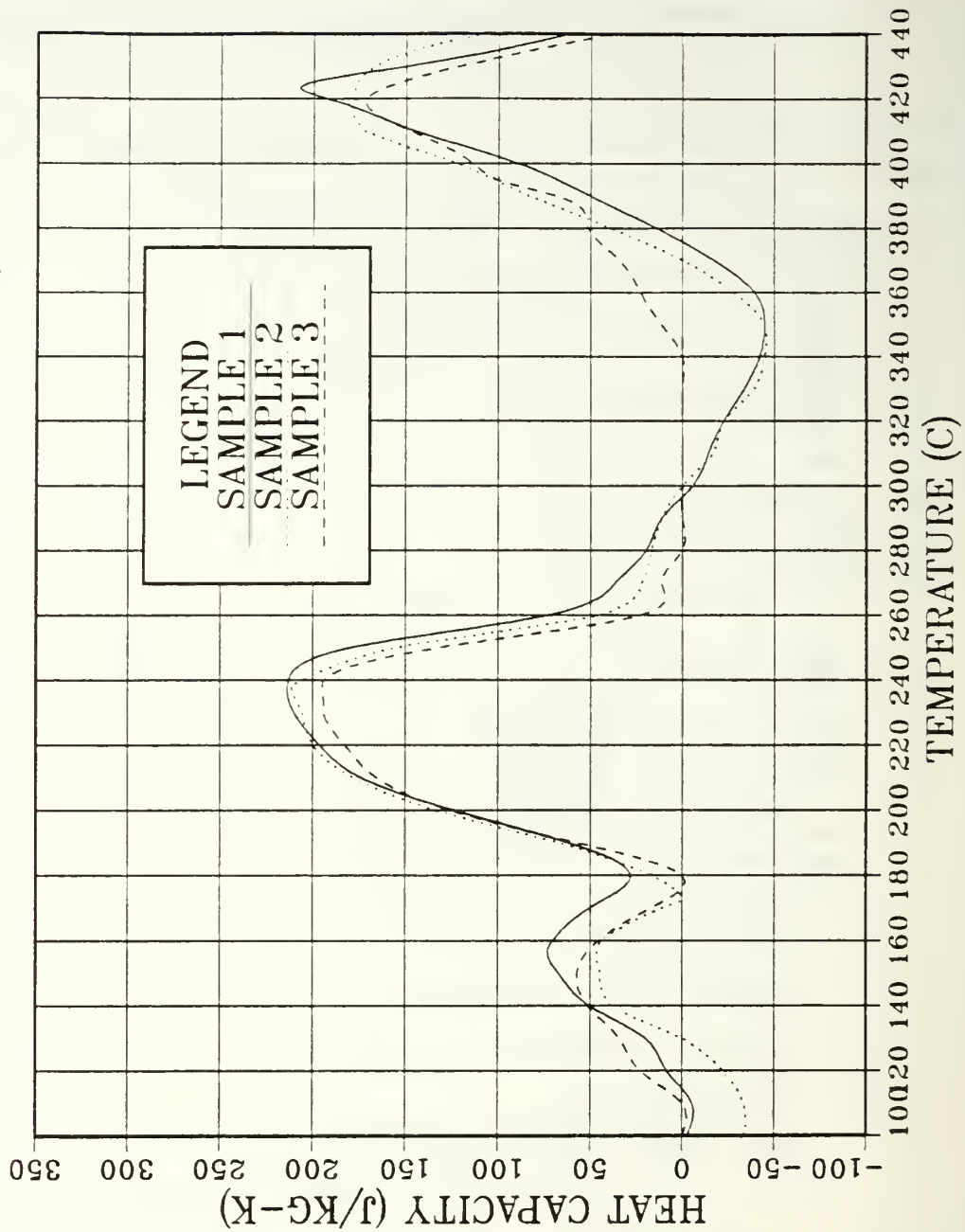


Figure 4.5 DSC trace for the 6-2 alloy (3rd run)

strain rate dependent. In addition, a series of temperatures were also selected so that elongations at elevated temperature could be correlated with the  $\beta$  peak temperature from the DSC traces. Hence the matrix of experiments shown in Table 6 was established.

TABLE 6  
MATRIX OF ELEVATED TEMPERATURE EXPERIMENTS

temp(C)	275	300	325	350
$\dot{\epsilon}$				
$6.7 \times 10^{-5}$				
$6.7 \times 10^{-4}$				
$6.7 \times 10^{-3}$				
$1.7 \times 10^{-2}$				
$6.7 \times 10^{-2}$				

The 8-1.2 alloy was tested over the entire strain rate range but only at 300°C. This experiment was necessary to evaluate the effect the added reheating time between rolling passes would have upon elongations when compared to the results achieved by Sanchez. The entire matrix was evaluated for both the 8-1 and the 6-1 alloys. No elevated temperature testing was possible on the 6-2 alloy due to its inability to warm roll successfully.

## 2. Al-8 wt. pct. Mg-1 wt. pct. Li

Results of the 8-1 tensile testing experiment are shown in Figure 4.6 . The flow stress data, obtained at 0.1 true strain, clearly show across all strain rates that the alloy is strongest at 275°C. For most strain rates, those tested at 350°C are the weakest material. Results at 300 and 325°C are similar with 325°C being marginally weaker. These curves all have a generally sigmoidal shape. The slopes of the flow stress curves ( $m$ -values) are maximum at around  $10^{-3} \text{ sec}^{-1}$ , but it must be remembered that the limited number of data points create uncertainty in these results. Particularly suspect is the flow stress curve at 350°C which appears to have an anomalous data point at  $6.7 \times 10^{-4} \text{ sec}^{-1}$ .

The ductility data show considerable scatter for the alloy at 350°C. While the unusual appearance of the results at 350°C cast some doubt about the validity of individual data points, it is clear that overall, at this temperature, the alloy is not as ductile as it is at lower temperatures. For example, when tested at 325°C, the material supports ductilities as high as 800% at strain rates of  $1.7 \times 10^{-2} \text{ sec}^{-1}$  and shows improved elongations over the entire range of strain rates. This trend continues when tested at 300°C with the maximum elongation achieved being over 1000%. These extreme elongations occurred at very high strain rates of  $6.7 \times 10^{-3}$  and  $1.7 \times 10^{-2} \text{ sec}^{-1}$ . The alloy showed a sharp drop in ductility when tested at 275°C in comparison to that seen at 300°C although a peak ductility near 500% was still a respectable result. The close link reported between maximum m-value and peak ductility is not seen in the data for this alloy. For example, at 300°C the m-value at  $1.7 \times 10^{-2}$  was found to be 0.3 with elongation equal to 1059%. This compares with an m-value of 0.4 at a strain rate of  $6.7 \times 10^{-4}$  where ductility was found to be 660%.

The tensile test samples from the 8-1 alloy tested at 300°C are shown in Figure 4.7. The extreme elongations compared to the undeformed sample are seen clearly. Also seen is the critical effect of strain rate on the total elongations which can be achieved. It should be noted that, comparatively, the sample tested at  $6.7 \times 10^{-2} \text{ sec}^{-1}$  is not the equal of the remaining samples; however, it was still able to achieve over 300% elongation at this very high strain rate.

Figure 4.8 illustrates the effects temperature has on the ductility and the flow stress. The flow stress versus temperature data indicate a clear trend to a softer material as temperature rises from 275 to 300°C where it levels off and may even slightly increase with further temperature increases. This can only indicate that some significant microstructural changes are occurring to cause a material hardening effect. The most likely reason for this is a grain growth phenomenon which accelerates rapidly as the  $\beta$  phase solvus is approached. The corresponding elongation versus temperature plot shows a clear softening behaviour with lower strain rates at all temperatures. This shows that the material at 10% true strain behaves in a more ductile manner at lower strain rates but exhibits much higher flow stresses at higher strain rates. This suggests that an overall strain rate sensitivity for this material, particularly at 300°C, will be very high and in fact this is seen in the previously discussed flow stress versus strain rate plot.

The ductility versus temperature plots for 8-1 show clearly that the optimum temperature for SPD in this alloy is 300°C. However, ductilities achieved were substantial over a relatively wide range of temperatures. The highest ductilities were found to occur at 300°C at all but the highest strain rate. The ductility clearly drops as the temperature approaches the  $\beta$  peak temperature as determined from DSC data. This could mean the microstructure is coarsening due to the dissolution of the  $\beta$  phase particles. The reason for a drop in ductility as the temperature goes below 300°C is likely the result of a slowing of diffusional processes necessary to support GBS.

Figure 4.9 provides details of the fracture of each of the 8-1 test samples strained at  $6.7 \times 10^{-5} \text{ sec}^{-1}$  at the four test temperatures. Clearly the failure mode has changed dramatically from the lower temperature, where a single distinct neck was seen, to the higher temperature where little necking was observed. At 300°C, the necking appears at several points along the sample indicating that the strain rate is just hardening the neck sufficiently to prevent further narrowing thereby causing the weaker structure elsewhere to begin the necking process. The 350°C sample clearly did not fail due to excessive necking but failed in a mode which resembles that seen in more brittle materials.

### 3. Al-6 wt. pct. Mg-1 wt. pct. Li

The same matrix of experiments was repeated for the 6-1 alloy and a summary of results is shown in Figure 4.10. One clear difference between the two alloys is that overall the flow stress for the 6-1 is higher, particularly at the moderate strain rates. The flow stress curves are less sigmoidal in shape and have maximum m-values at a lower strain rate than does 8-1.

The ductility data reflect these differences in the flow stress curves by having peak elongations at lower strain rates. The lower strain rate ductility is comparable to that for 8-1 for all temperatures. Interestingly, in this case the second highest ductilities were obtained at 275°C rather than at 325°C. This suggests that, at higher temperatures, the lesser volume fraction of  $\beta$  phase, as detected by DSC, might be returning to solution more quickly thereby diminishing the microstructural stability.

Temperature clearly has the same overall impact on the ductility of the 6-1 alloy as depicted in Figure 4.11. Here also the best superplastic forming conditions are at 300°C. The significant difference is that high ductilities are obtainable over a smaller range of temperatures and strain rates.

# AL-8%MG-1%LI

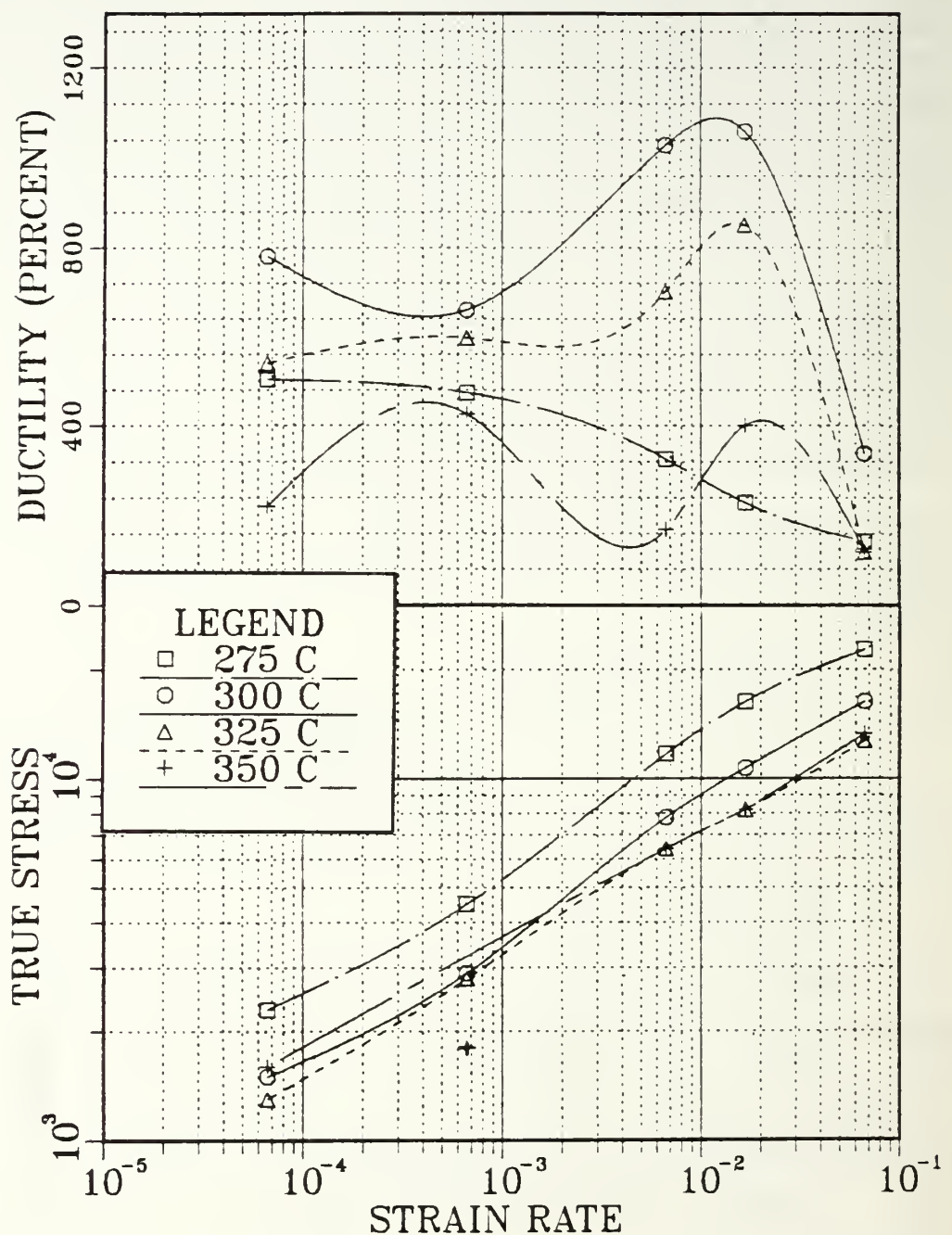


Figure 4.6 Mechanical properties vs strain rate for the 8-1 alloy

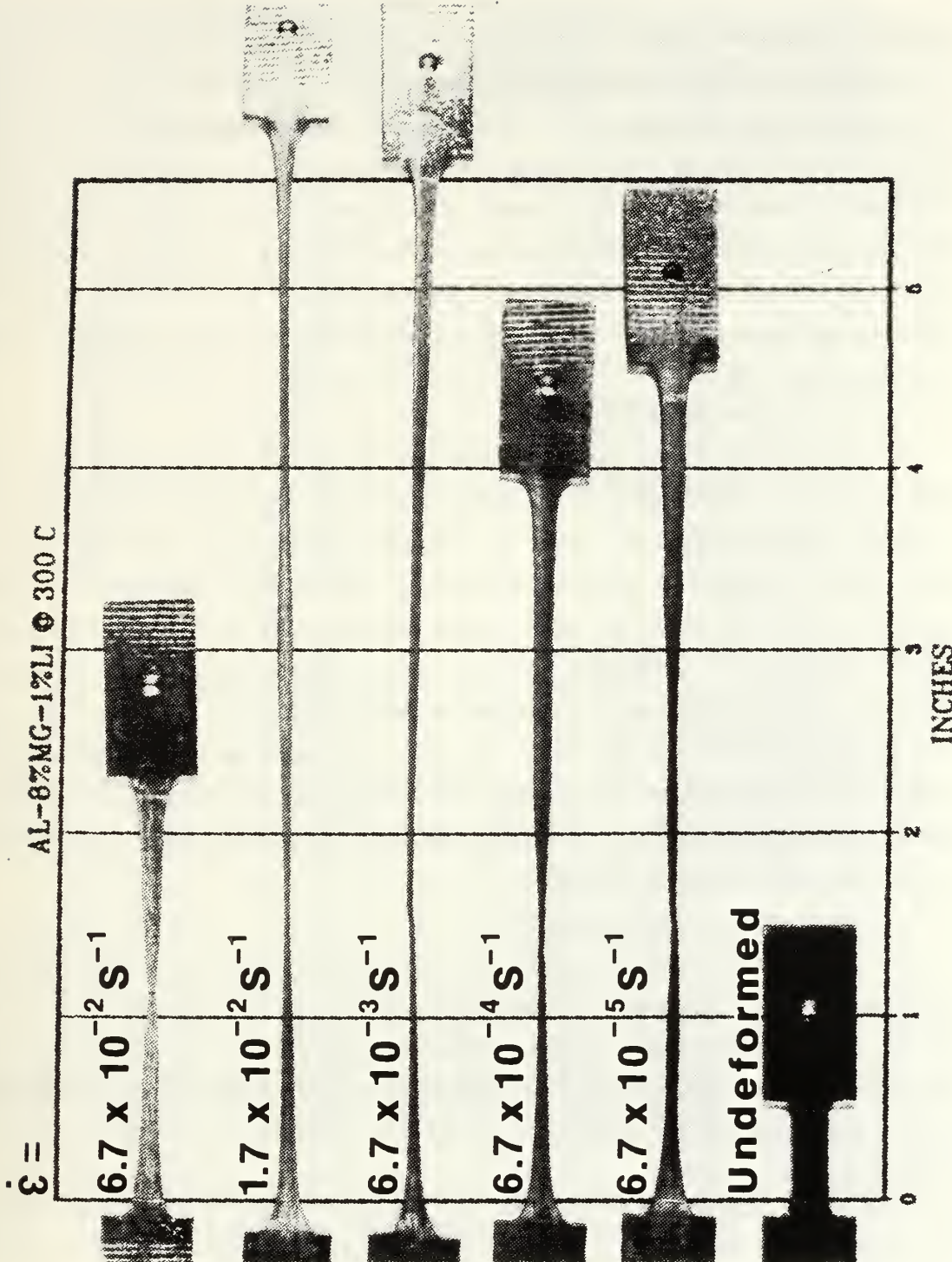


Figure 4.7 Tensile samples of the 8-1 alloy deformed at 300°C

The flow stress versus temperature data for the 6-1 alloy show a similar trend where the flow stress is lower at lower strain rates. The shape of these curves indicates a hardening effect as temperature increases from 300 - 325°C and continued softening as the temperature increases to 350°C. This effect is more distinct than for the 8-1 alloy which may indicate that the structure is coarsening more rapidly as the  $\beta$  solvus temperature is exceeded. As the microstructure loses the stabilizing influence of the  $\beta$  particles, grains will grow rapidly resulting in the hardening effect seen in both alloys. The trend seen at higher temperatures indicates that, once the  $\beta$  has completely dissolved and microstructural coarsening is completed, the overall softening continues with increasing temperature.

#### **4. Al-8 wt. pct. Mg-0.5 wt. pct. Li**

The data have established that 300°C is the optimum temperature for SPD of both 8-1 and 6-1 alloys. This is the same temperature at which the 8-1.2 alloy was tested. It would therefore be useful to compare the three alloys and this is done in Figure 4.12. The trend noted earlier, in which the alloy showing the highest flow stress overall is also the least ductile, remains valid here also. The flow stress of the 8-1 and the 8-1.2 alloys are comparable over the entire range of strain rates as are the ductilities, with the exception of the higher strain rates where 8-1 is superior. It should be noted that the relative order of the ductilities is the same as the relative order of  $\beta$  phase peak size in the DSC experiment. This implies that the superplastic response of these alloys depends heavily upon the presence of the second phase. To assess this further a TEM study was undertaken.

#### **5. Al-10 wt. pct. Mg-0 wt. pct. Li**

Also plotted on Figure 4.12 are the results of the 10-0 alloy which was processed in the same manner as that used in this work. The obvious improvement that all three lithium containing alloys show, when compared to the binary alloy data, points to a significant effect caused by lithium on the superplastic response. The reason for this is not immediately obvious and TEM data comparison is required to assist in understanding this result.

### **D. TEM**

#### **1. Al-8 wt. pct. Mg-1 wt. pct. Li**

The 8-1 microstructure is compared with that of the 10-0 alloy in Figure 4.13 as each would appear at the onset of deformation in a tensile test. These samples were

# AL-8%MG-1%LI

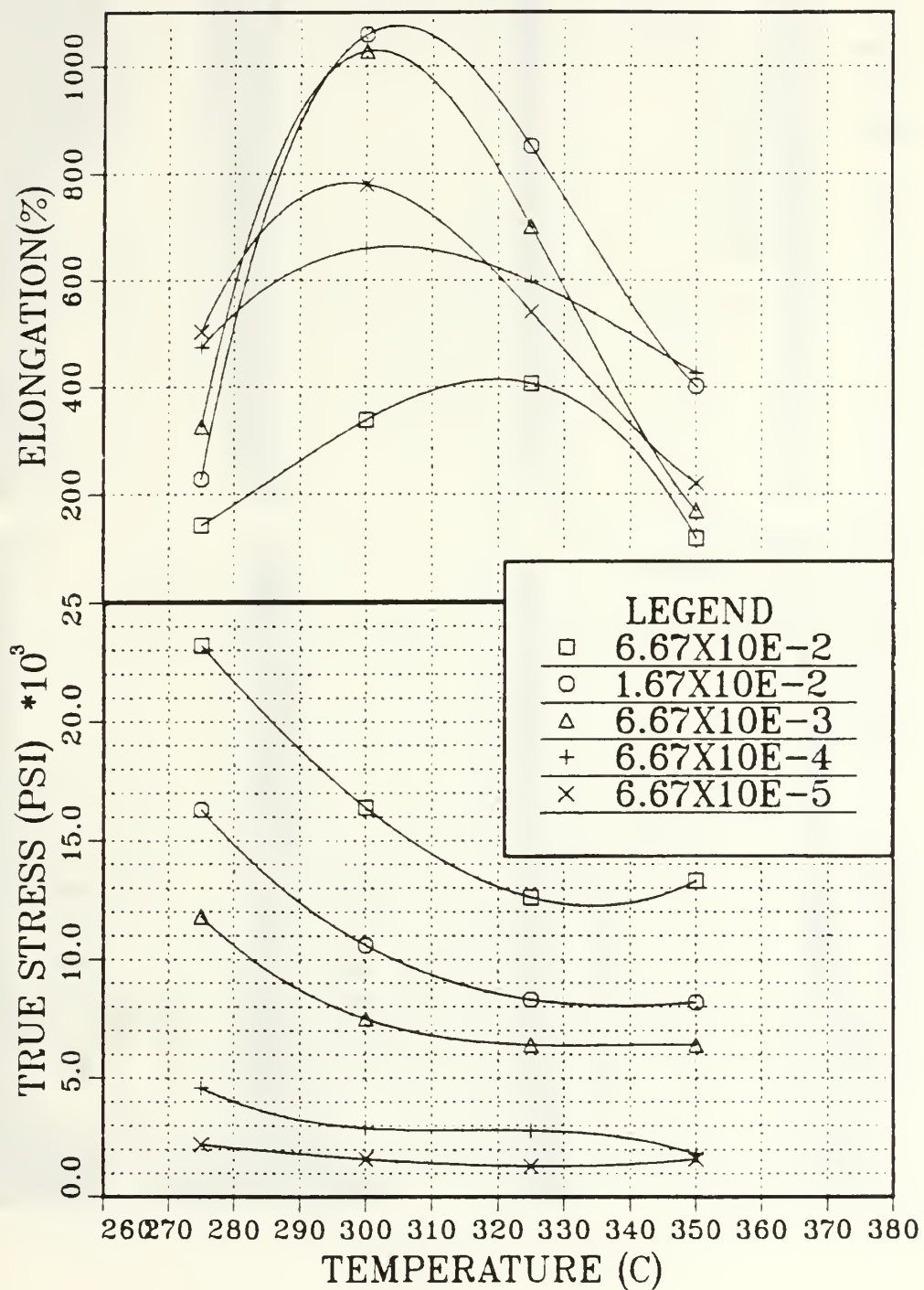


Figure 4.8 Mechanical properties vs temperature for the 8-1 alloy

$$\dot{\varepsilon} = 6.7 \times 10^{-5} \text{ s}^{-1}$$

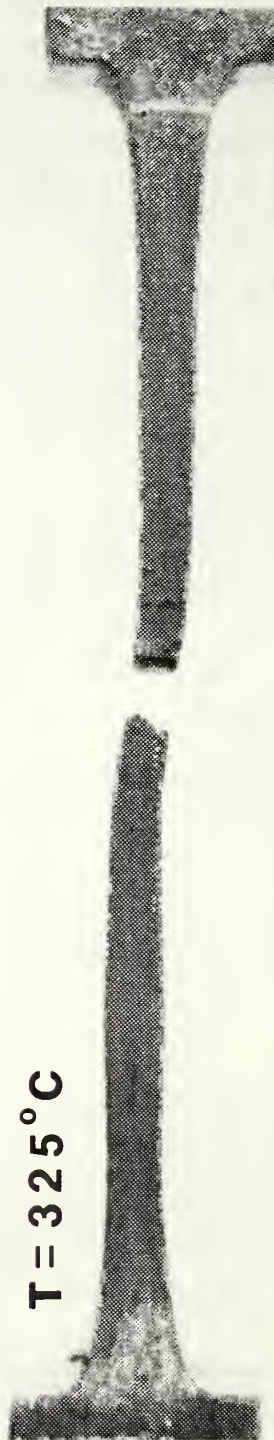
$$T = 275^\circ\text{C}$$



$$T = 300^\circ\text{C}$$



$$T = 325^\circ\text{C}$$



$$T = 350^\circ\text{C}$$

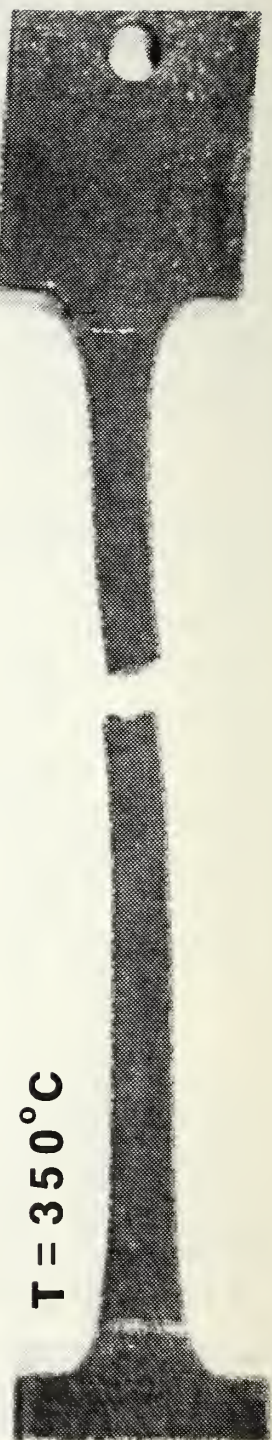


Figure 4.9 Variation in fracture mode due to temperature

# AL-6%MG-1%LI

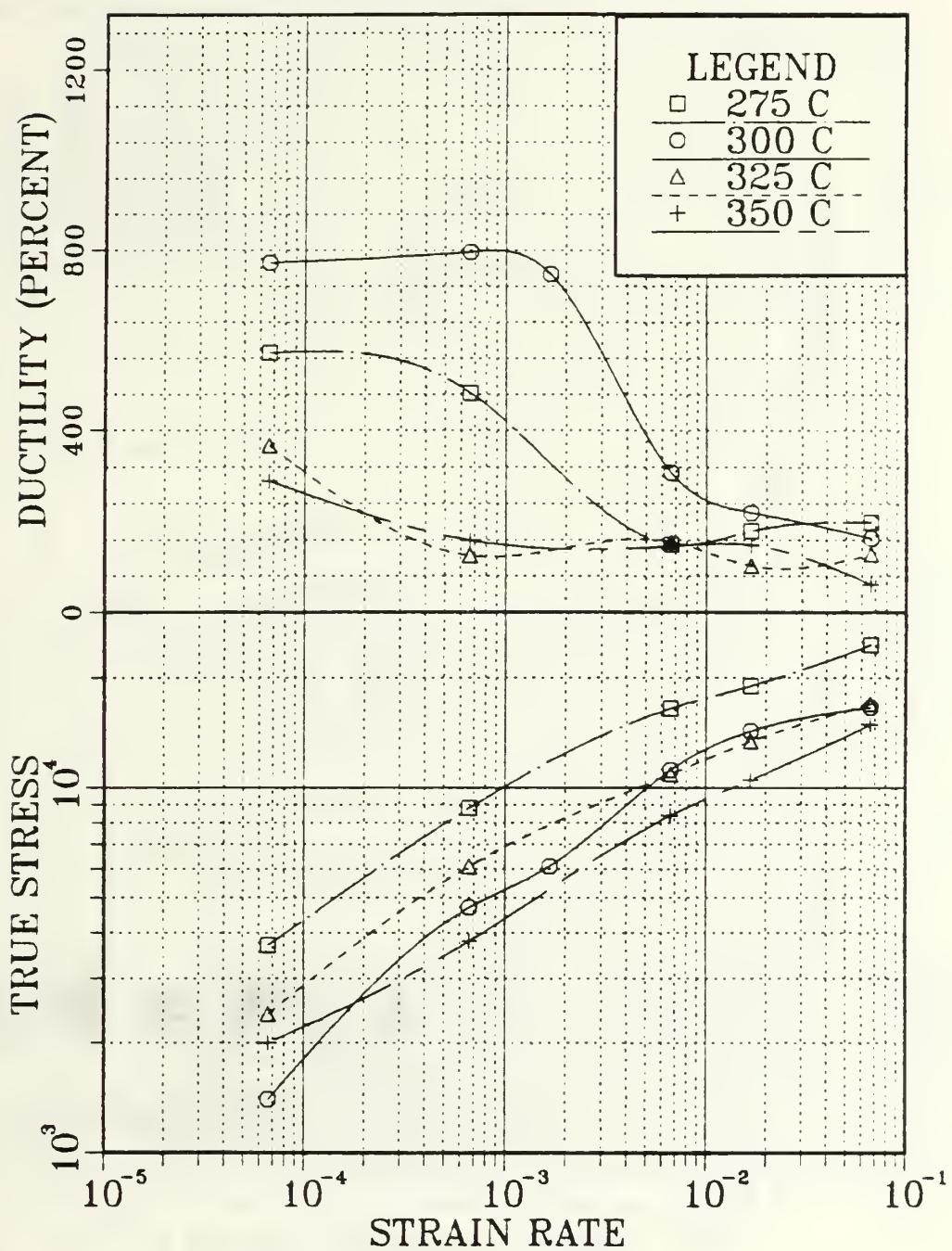


Figure 4.10 Mechanical properties vs strain rate for the 6-1 alloy

# AL-6%MG-1%LI

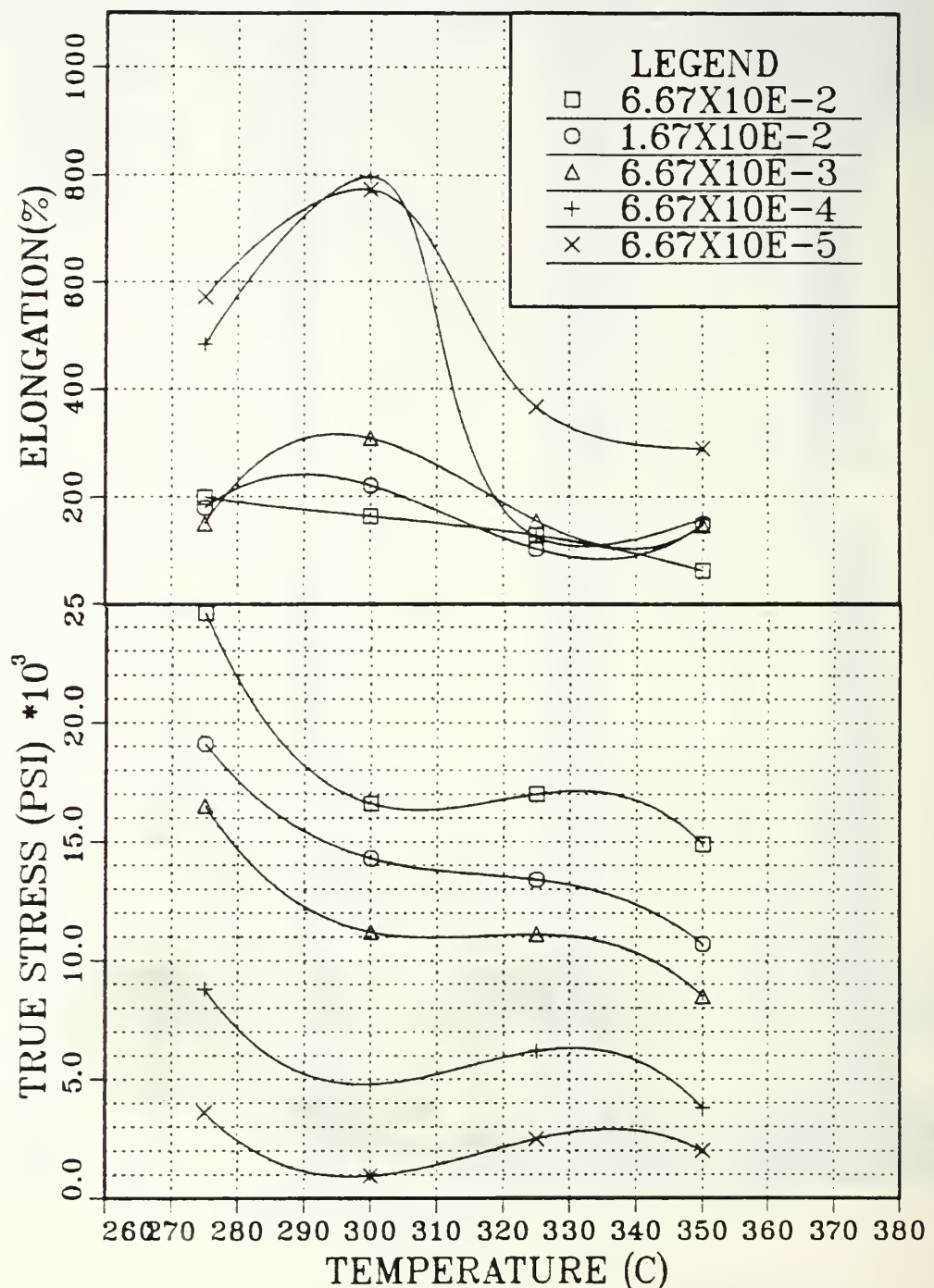


Figure 4.11 Mechanical properties vs temperature for the 6-1 alloy

# ELONGATION / TRUE STRESS VS STRAIN RATE

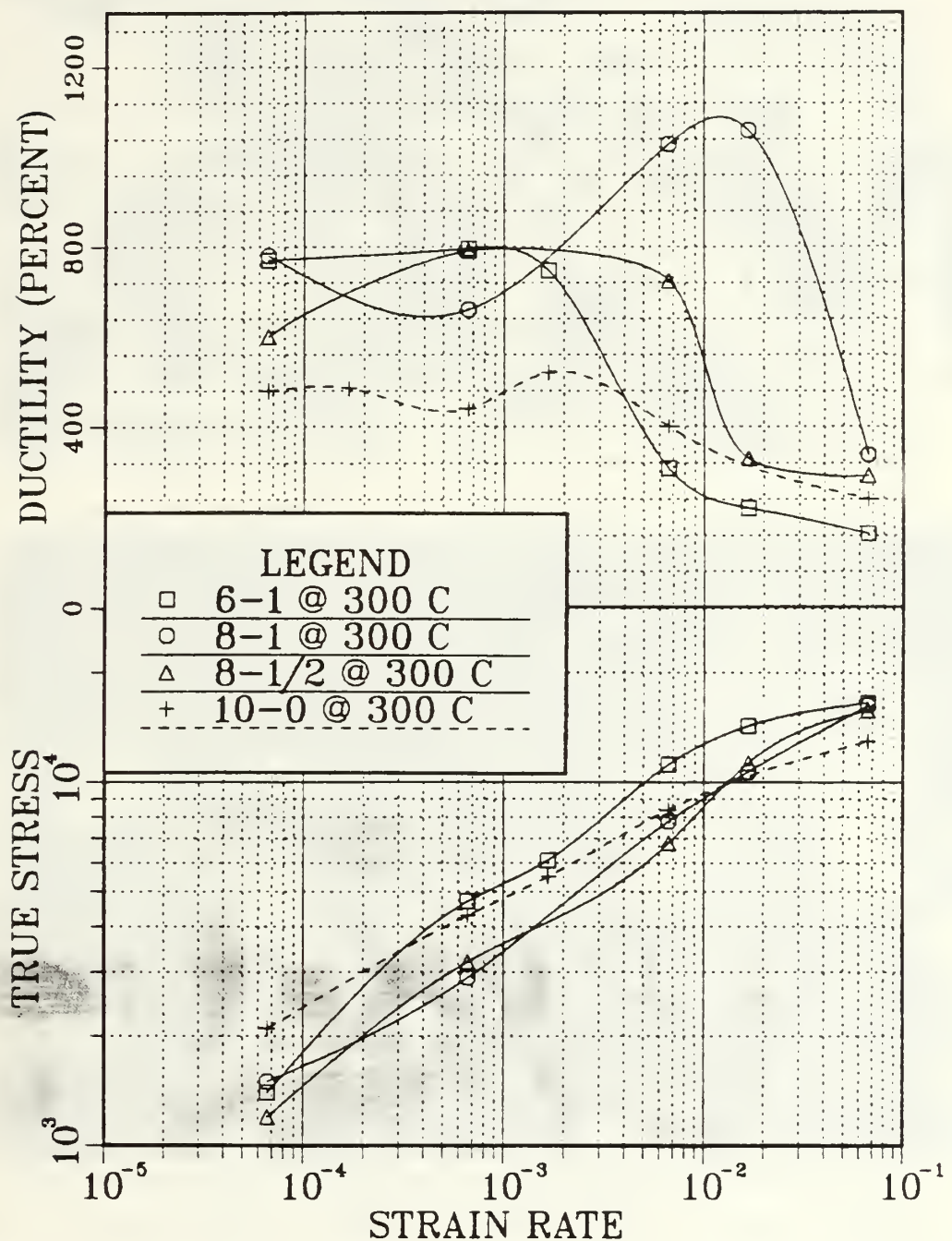


Figure 4.12 Mechanical properties for 4 identically processed alloys

taken from grip sections of tensile samples which were deformed at  $1.7 \times 10^{-2} \text{ sec}^{-1}$ . Due to the short duration of the test at this high strain rate, the total time at elevated temperature following TMP would be approximately the same as that seen by the gauge section of any sample as it begins to deform. The microstructure of the 10-0 alloy shows evidence of high dislocation density in some areas as well as other areas where the grains are relatively dislocation free. The grain size can also be seen to vary over the micrograph.  $\beta$  phase is evident as small spheroidal precipitates in clusters which appear to coincide with the finest structure. In contrast, the 8-1 alloy shows a very homogeneous appearance. The grain size is remarkably uniform and no evidence of areas of high dislocation density can be seen. Grain subgrain boundaries are all well-defined. The  $\beta$  phase particles are larger than seen in the 10-0 alloy and are more evenly dispersed. The microstructural dimensions are on the order of the interparticle spacing. The relative ductilities of these two identically processed materials shows the 8-1 alloy to be approximately twice as ductile throughout the strain rate range, suggesting that the 8-1 microstructure is the more stable of the two. The micrographs seem to support the hypothesis that the  $\beta$  phase is the critical microstructural stabilizer.

Figure 4.14 shows higher magnification of the same 8-1 sample. Here also the well-defined nature of the grain boundaries can be seen and the relatively dislocation free grains are evident. The even distribution of the  $\beta$  phase is still apparent even at the higher magnifications. Micrograph (b) shows clear examples of the  $\beta$  phase residing along boundaries and at triple points.

Figure 4.15 shows direct comparison of the gauge sections of an 8-1 2 and 8-1 tensile sample following SPD. The 8-1 2 alloy microstructure is homogeneous and shows well-defined boundaries. The microstructures are of similar size in both alloys. The most striking feature of these micrographs is again the relative lack of  $\beta$  phase in the 8-1 2 as compared to the 8-1 alloy. The  $\beta$  particles in the 8-1 sample are no longer mostly on grain boundaries but can be found within grains, implying that the grains have grown substantially during deformation. A bright field dark field pair of the 8-1 alloy after deformation is shown in Figure 4.16 . Of note here is the precipitate residing at a triple point and the well-defined boundaries existing between grains. It is also possible to see a low angle boundary apparently forming within the structure of a grain.

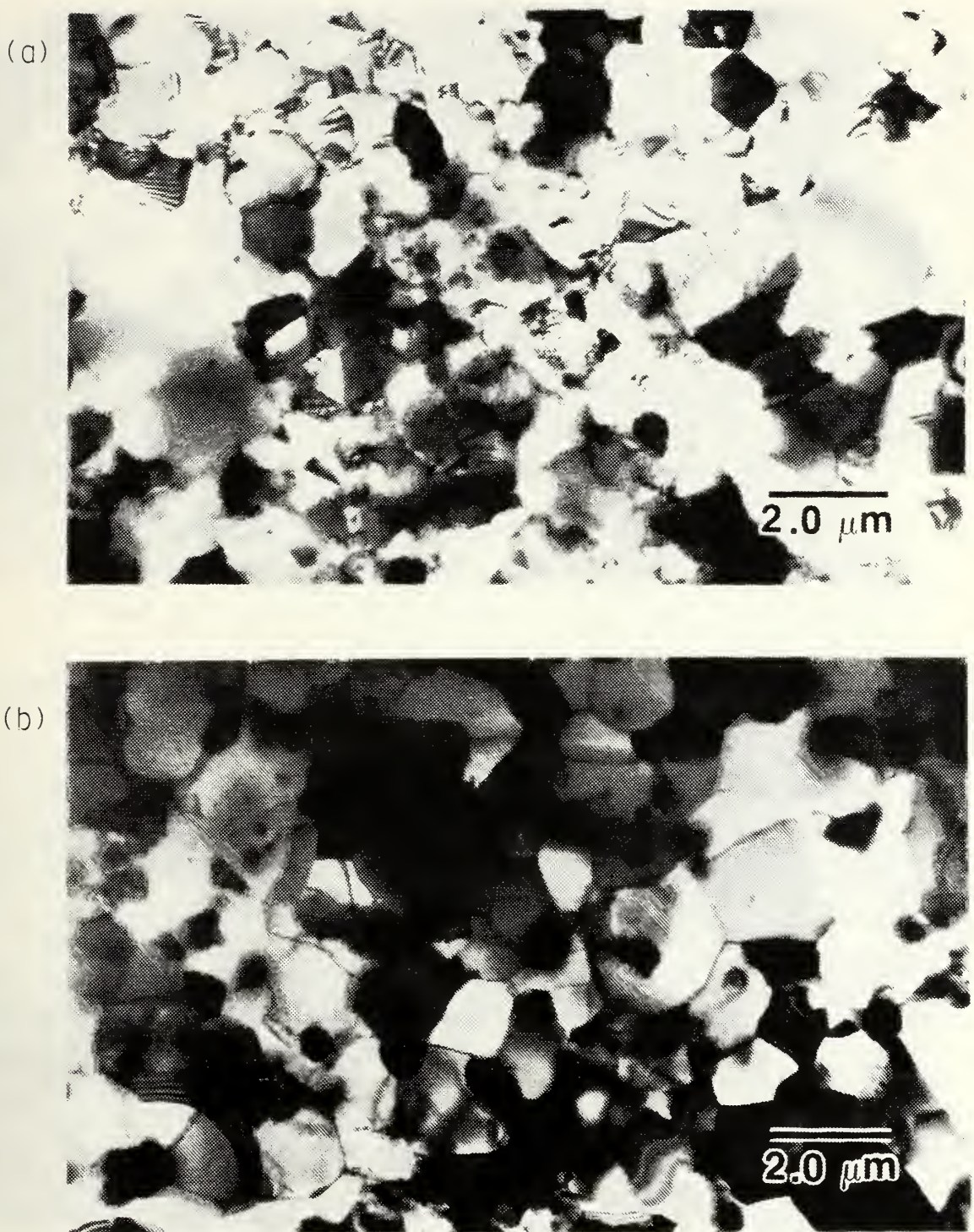
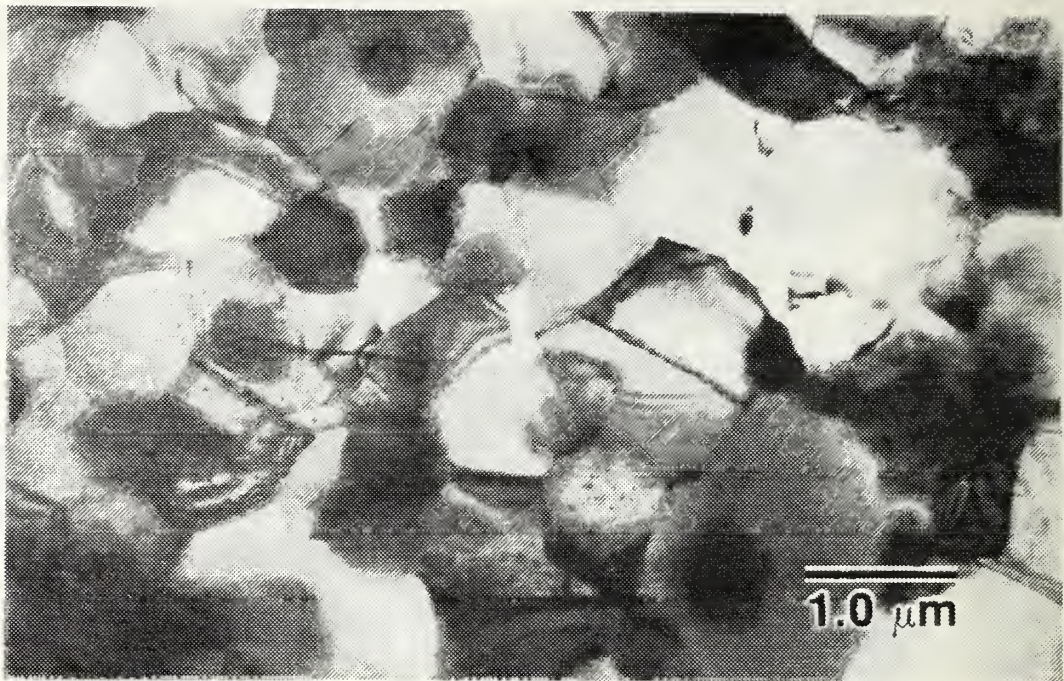


Figure 4.13 10-0 and 8-1 prior to deformation

A comparison between the microstructures of (a) the 10-0 alloy and (b) the 8-1 alloy prior to deformation at 300°C indicates a more homogeneous distribution of the  $\beta$  phase in the 8-1 microstructure.

(a)



(b)

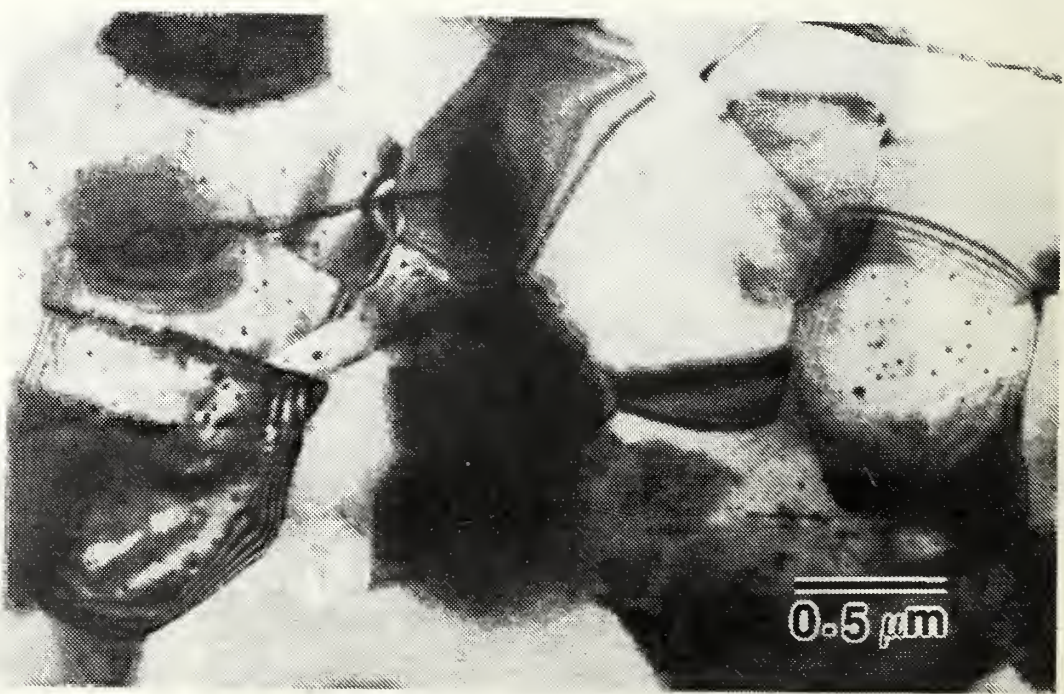


Figure 4.14 8-1 prior to deformation

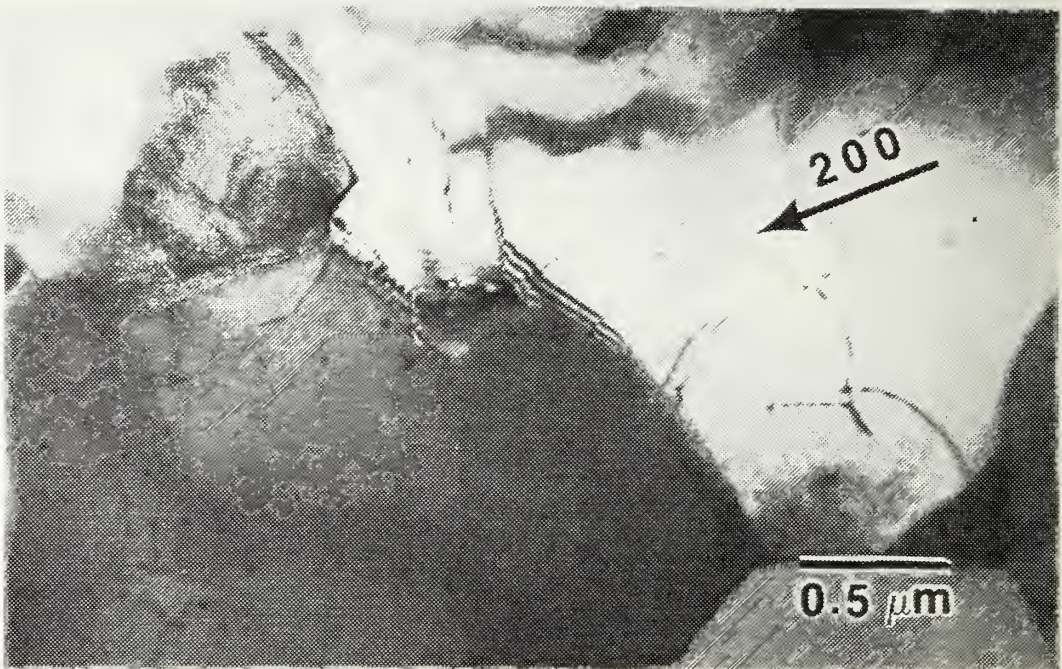
A closer examination of the microstructure shown in Figure 4.13 b reveals (a) a grain size of 1 - 3  $\mu\text{m}$  and an absence of dislocations and (b) 0.5 - 1.0  $\mu\text{m}$   $\beta$  particles residing at grain boundary triple points.



Figure 4.15 8-1.2 and 8-1 following deformation at  $1.7 \times 10^{-2} \text{ sec}^{-1}$

A comparison between the microstructures of (a) the 8-1.2 alloy and (b) the 8-1 alloy after deformation at 300°C indicates the increased volume fraction of the  $\beta$  phase in the 8-1 microstructure.

(a)



(b)

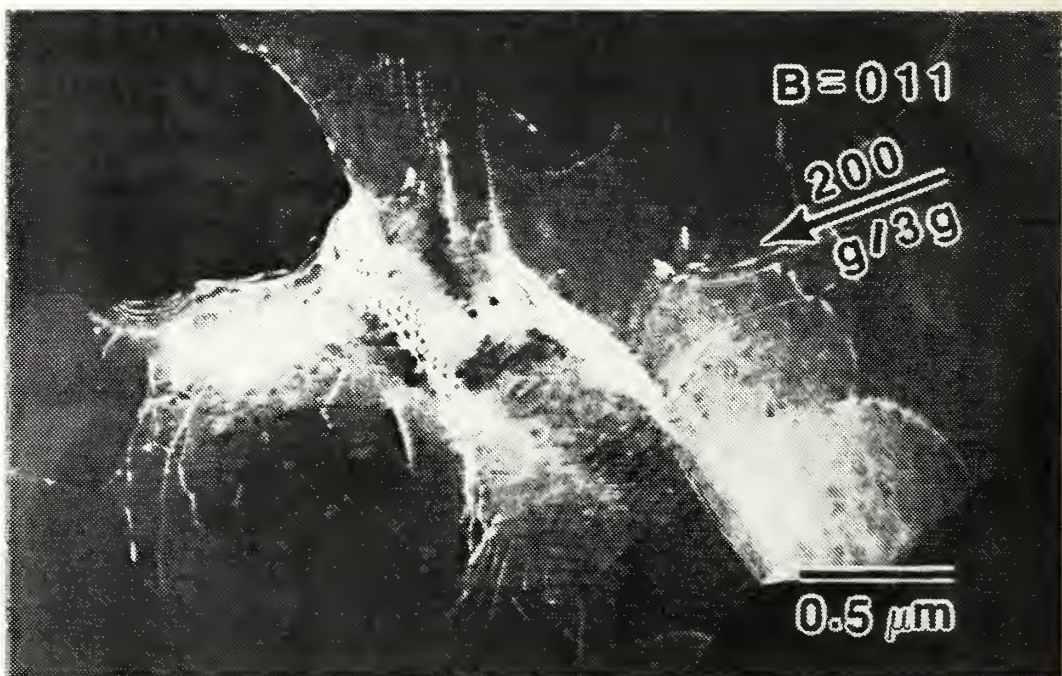


Figure 4.16 8-I bright field dark field following deformation at  $1.7 \times 10^{-2} \text{ sec}^{-1}$

Imaging the microstructure shown in Figure 4.15 b using (a) bright field and (b) weak-beam dark field reveals evidence of dislocation activity during deformation. Note the apparent formation of a boundary adjacent to a  $\beta$  particle.

## 2. Al-6 wt. pct. Mg-1 wt. pct. Li

The 6-1 alloy was examined with TEM in the same manner as the 8-1 alloy. First a specimen was taken from the grip section of a sample that had been deformed at  $1.67 \times 10^{-2} \text{ sec}^{-1}$  in order to assess the microstructure at the onset of SPD. Figure 4.17 and Figure 4.18 are views of a representative area of this sample. It is obviously a more coarse structure than that seen in the 8-1 alloy after a similar thermal history. For the most part, boundaries are well-defined but areas of higher dislocation density can also be seen. The bright field dark field pair at higher magnification shows what appears to be a relatively dislocation free grain with a subgrain forming within it. The subgrain may have been prevented from coarsening by a  $\beta$  particle which was removed during electropolishing of the sample. This could explain why it remained relatively



Figure 4.17 6-1 prior to deformation

The microstructure of the 6-1 alloy at the onset of deformation at 300°C exhibits a coarser grain size (2 - 4  $\mu\text{m}$ ) than the 8-1 alloy. The reduced volume fraction of  $\beta$  particles is also evident.

small while other structures around it grew larger.

Figure 4.19 shows the 6-1 alloy following deformation at  $1.7 \times 10^{-2} \text{ sec}^{-1}$ . This microstructure is not homogeneous, having zones where dislocation density is still quite high and other zones where nearly dislocation free structures can be seen. In this micrograph there are relatively few second phase particles, and those there are do not appear to be closely enough spaced to prevent grain boundary migration. This could explain why this alloy was not able to achieve the high ductilities at high strain rates. A bright field dark field pair taken from this same sample shows details within a constituent grain (Figure 4.20). The grain of the order of  $3 \mu\text{m}$  in size shows evidence of dislocations interacting with a fine non-uniform dispersion of particles which may be evidence of dislocation motion during SPD process. These particles have been identified as the secondary  $\text{Al}_3\text{Zr}$  phase which in this case is semi-coherent with the matrix. Dislocation motion is apparently inhibited by the presence of these particles; however these particles are not effective in retardation of grain growth due to their non-uniform size and distribution throughout the matrix.

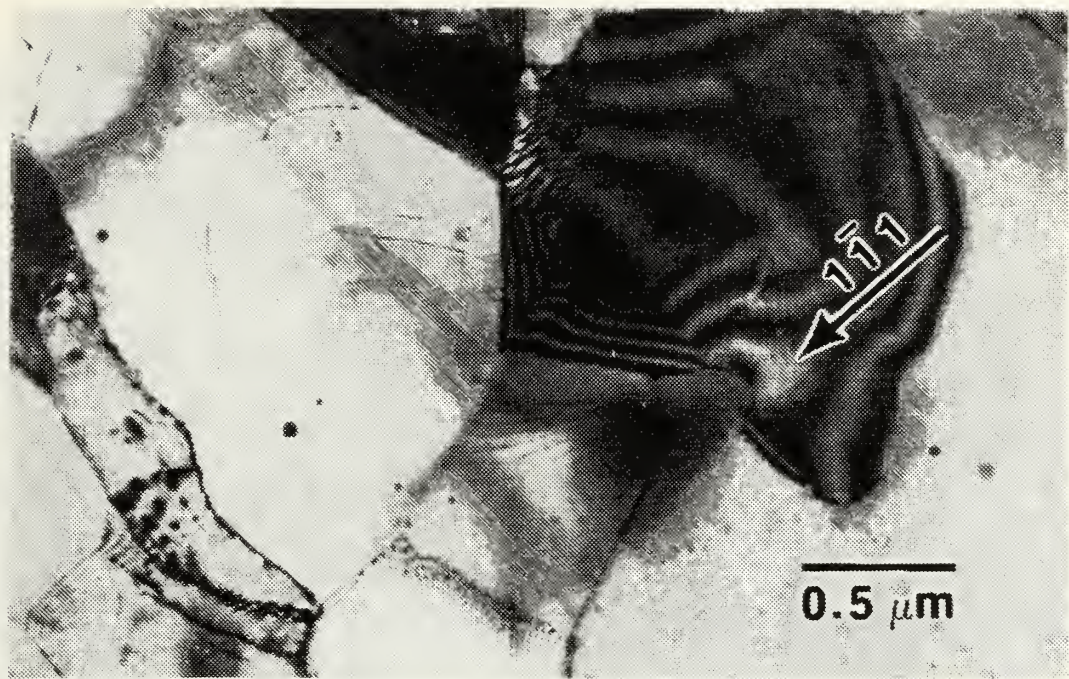
To determine why this alloy was so much more ductile at lower strain rates, a TEM sample was taken from the gauge section of a tensile specimen deformed at  $6.67 \times 10^{-3}$ . The micrograph in Figure 4.21 shows the results of an extended time at elevated temperature. The boundaries are well-defined, grains are essentially strain free, and the structure size is becoming comparatively large. There is very little  $\beta$  phase visible which suggests that much of it has returned to the solid solution during the deformation process. A grain in this sample is shown in Figure 4.22 in both bright and dark field at higher magnification. The grain contains a very fine dispersion of particles which appears to be incoherent with the matrix and quite unevenly distributed. For these reasons, along with DSC data, it is not likely that this is  $\delta'$  and instead it is probably  $\text{Al}_3\text{Zr}$ .

### 3. Al-6 wt. pct. Mg-2 wt. pct. Li

The micrographs of Figure 4.23 are of a sample taken from a small portion of 6-2 which was rolled at  $350^\circ\text{C}$ . They show a very high density of dislocations throughout the material. These dislocations so distort the image that no grain or subgrain boundaries can be identified. This type of structure is typical of those seen in as-rolled aluminum alloys and offers no clues to the rolling problems encountered.

The material from which the previous micrographs were taken was annealed for 1 hour at  $300^\circ\text{C}$  in order to better view the substructure. The microstructure which

(a)



(b)



Figure 4.18 6-1 bright field/dark field prior to deformation

A more detailed investigation of the constituent boundaries from Figure 4.17 using (a) bright field and (b) weak-beam dark field imaging reveals their low angle nature, composed of regular arrays of dislocations.

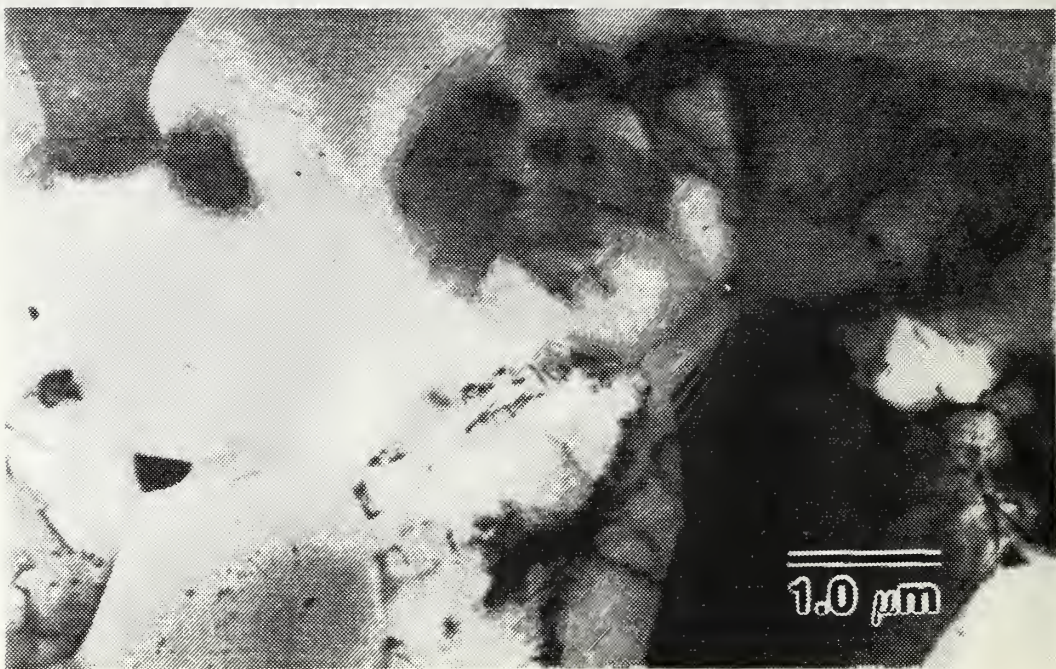


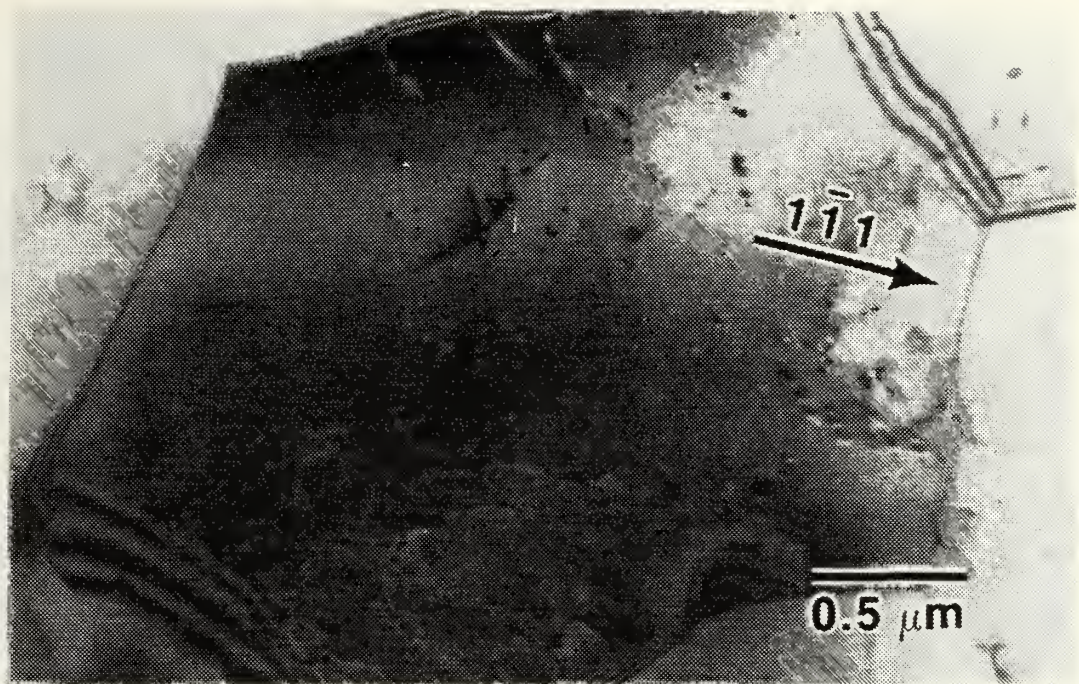
Figure 4.19 6-1 following deformation at  $1.7 \times 10^{-2} \text{ sec}^{-1}$

The microstructure of the 6-1 alloy at the conclusion of deformation at  $300^\circ\text{C}$  ( $\dot{\epsilon} = 1.7 \times 10^{-2} \text{ sec}^{-1}$ ) shows that the structure has coarsened in the absence of sufficient  $\beta$  particles to retard growth.

resulted from that heat treatment is shown in Figure 4.24 . The structure possesses relatively fine grains with moderately well-defined boundaries. The structure is reasonably homogeneous but areas exist where the structure is finer. These finer areas appear to be associated with a higher density of second phase precipitates which seem to prefer forming along grain boundaries. The precipitates are of various sizes and geometries but do seem to have a stabilizing impact on the microstructure. In view of the DSC data, these precipitates are believed to be  $\text{Al}_2\text{MgLi}$ .

For direct comparison of TEM with DSC results, it was decided to utilize one of the 6-2 DSC samples in the TEM experiment. The structure proved to have quite large grains and the bright field dark field pair in Figure 4.25 shows a typical example of the structure within one of the grains. The coherent, very finely dispersed particles are homogeneously distributed. These particles were identified as the  $\delta'$  phase as

(a)



(b)

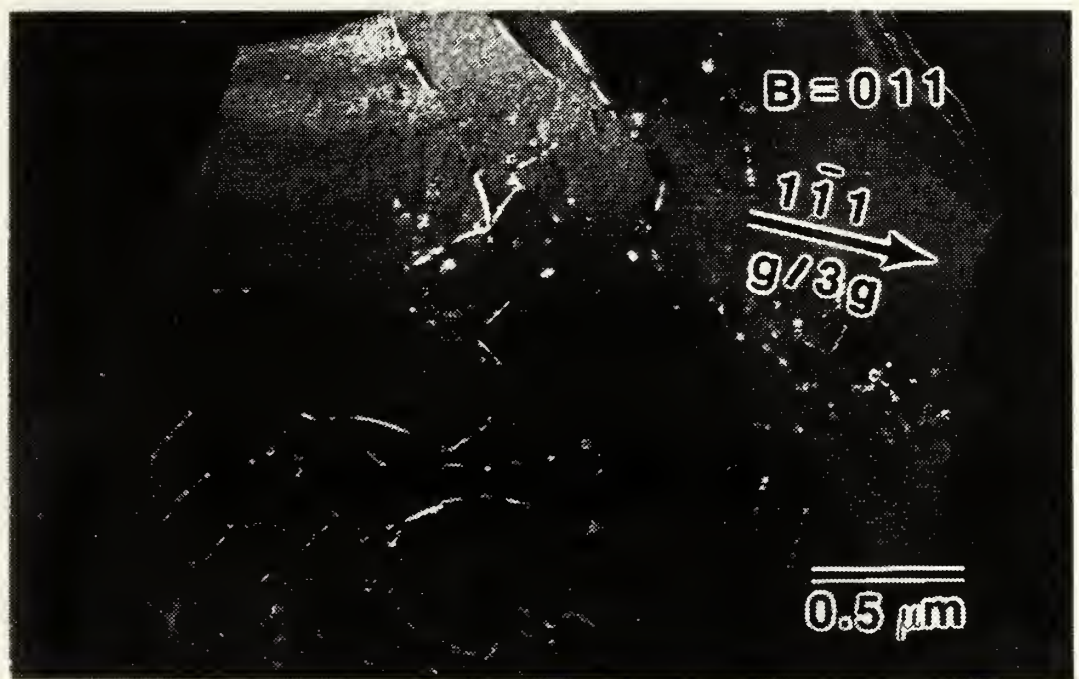


Figure 4.20 6-1 bright field dark field following deformation at  $1.7 \times 10^{-2} \text{ sec}^{-1}$

A bright field weak beam dark field pair of micrographs shows the details of individual dislocations interacting with  $\text{Al}_3\text{Zr}$  dispersoid particles within a constituent  $3 \mu\text{m}$  grain from the microstructure in Figure 4.19 .

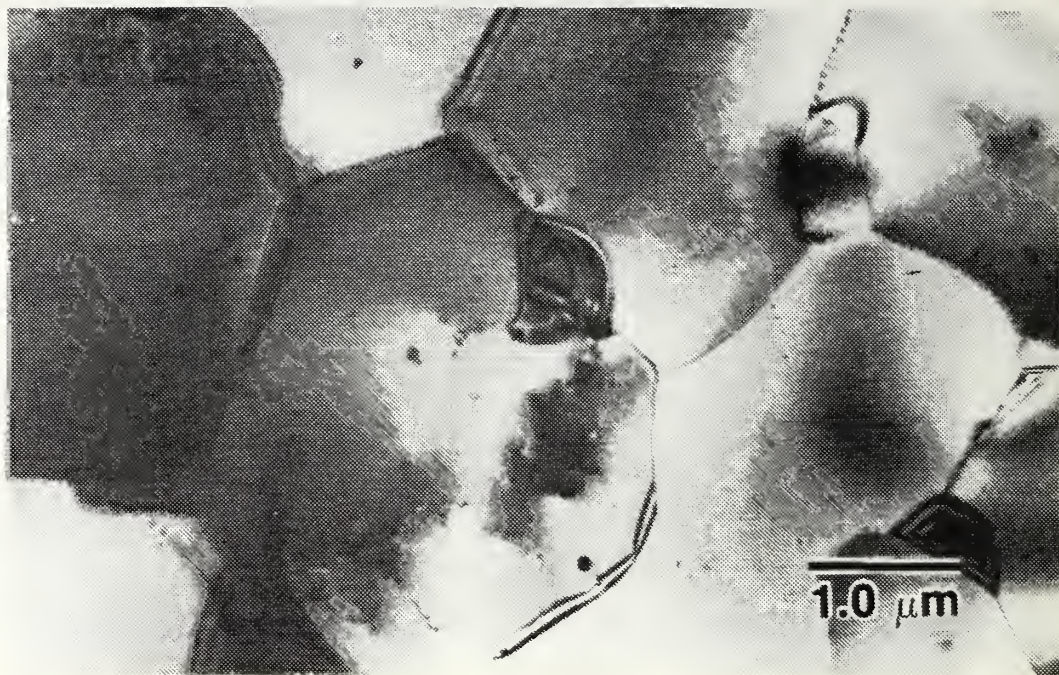


Figure 4.21 6-1 following deformation at  $6.7 \times 10^{-3} \text{ sec}^{-1}$

Deformation at a lower strain rate ( $\dot{\epsilon} = 6.67 \times 10^{-3} \text{ sec}^{-1}$ ) has produced a more well-developed structure in the 6-1 alloy (when compared with Figure 4.19). This would account for the improved ductility observed in this material.

predicted by the DSC results. Concurrent work by Ferris [Ref. 20] has shown that the presence of such a  $\delta'$  distribution greatly enhances the hardness of the material. The primary objective of future research on this alloy will be aimed at achieving superplastic forming capability such that these subsequent potential strengthening effects may be realized.

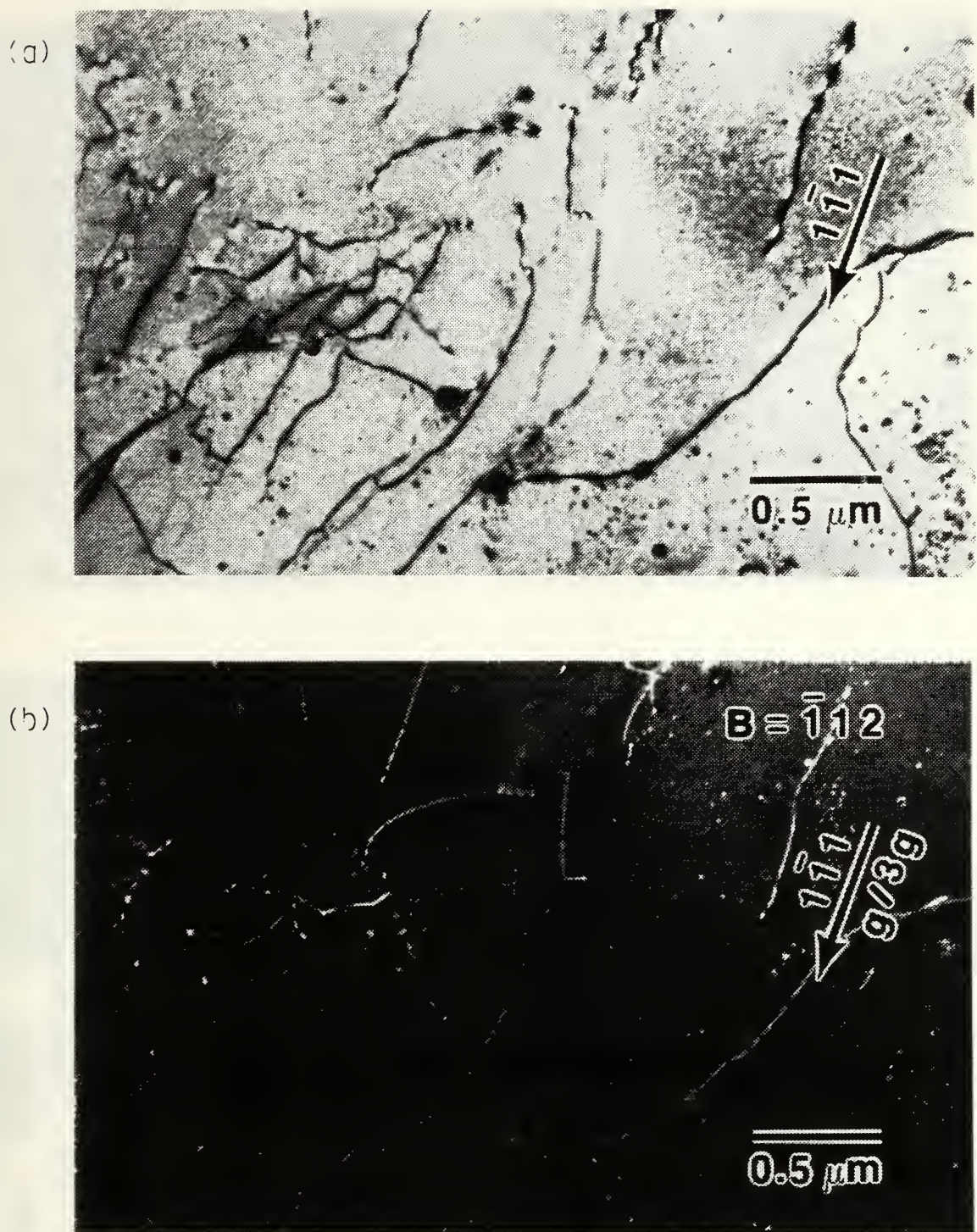
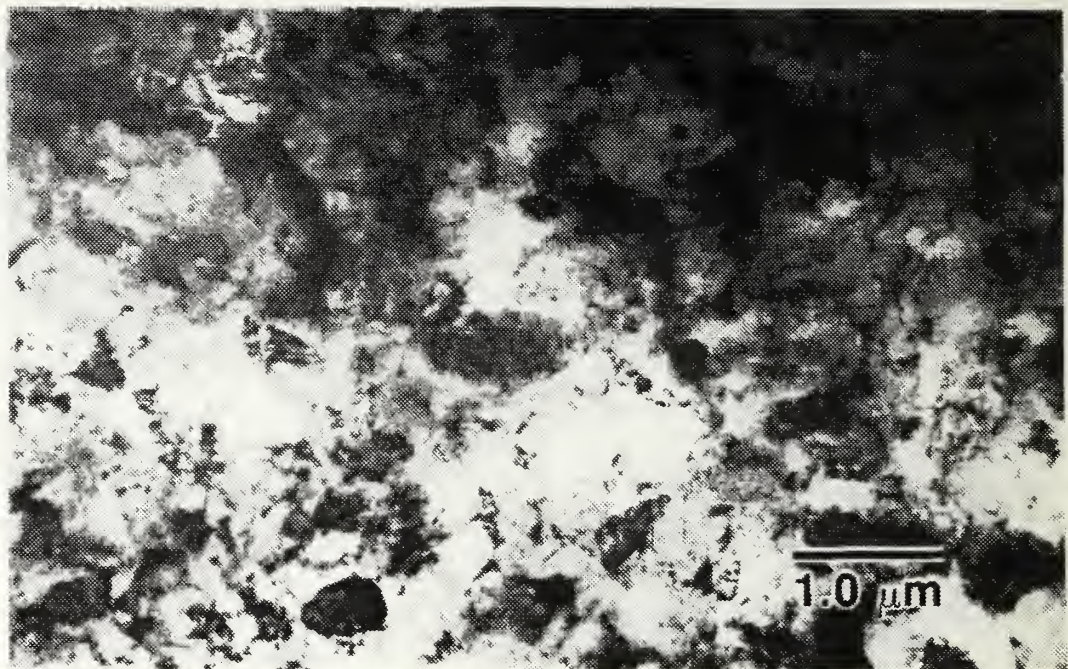


Figure 4.22 6-1 bright field/dark field following deformation at  $6.7 \times 10^{-3} \text{ sec}^{-1}$

Imaging of the interior of a representative grain from Figure 4.21 using (a) bright field and (b) weak-beam dark field shows evidence of considerable dislocation activity and the presence of a non-uniform distribution of  $\text{Al}_3\text{Zr}$  particles.

(a)



(b)

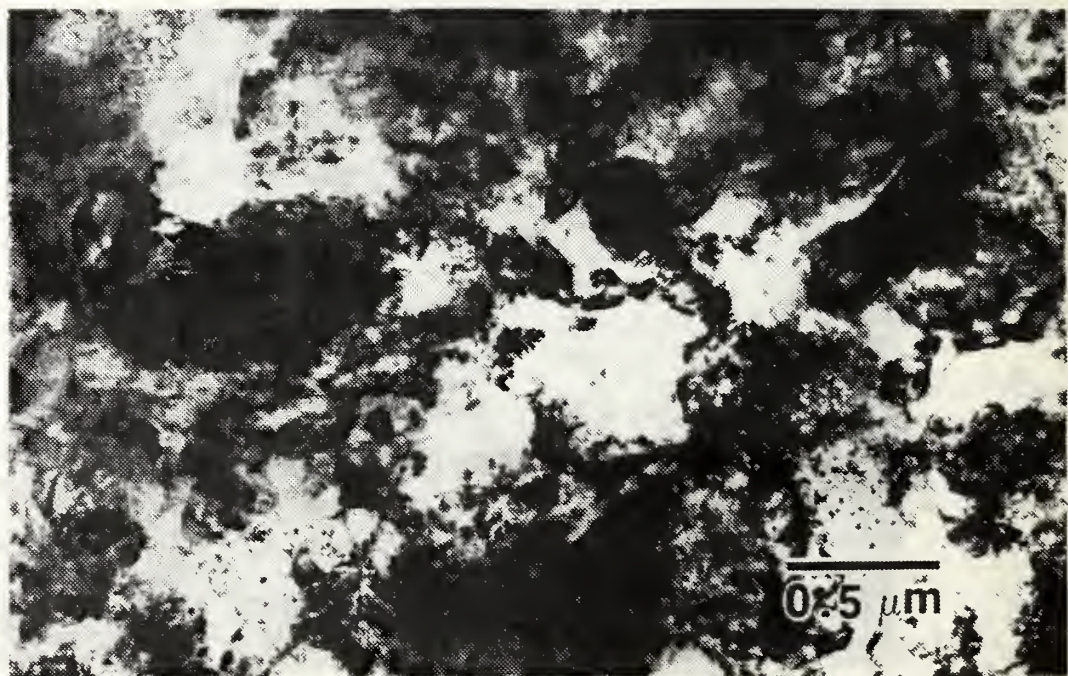


Figure 4.23 6-2 in the as-rolled condition

The structure of the 6-2 alloy rolled at 350°C to a true strain of 2.5 exhibits a very high dislocation density which completely obscures the features of the underlying microstructure.

(a)



(b)



Figure 4.24 6-2 following 1 hour anneal at 300°C

The heavily deformed structure seen in Figure 4.23 has transformed into a well-defined substructure during a 1 hour anneal at 300°C. The microstructure exhibits similar characteristics to other alloys capable of a superplastic response.

(a)



(b)



Figure 4.25 6-2 following DSC cycling

The microstructure of the 6-2 alloy after cycling in the DSC exhibits a uniform distribution of fine (10 nm)  $\delta'$  precipitates. This bright field dark field pair shows the potential hardening effects of such a precipitate morphology.

## V. DISCUSSION

### A. DSC

In light of subsequent mechanical property and TEM results, the DSC proved to be a useful aid in determining processing temperatures and precipitation sequences. TEM confirmed the identities of the various phases present in the alloys in addition to allowing a determination of solvus temperatures. It is clear that the height of DSC peaks can also indicate relative volume fractions of constituent phases. The TEM investigation highlights the importance of the volume fraction of the second phase. Comparing the micrographs was simplified by consideration of the relative area under the appropriate DSC peaks.

The position of the exothermic peak for the three quasi-binary alloys was the same within experimental error. Thus the thermomechanical processes were designed to be the same for all three. The success of this TMP suggests that, for designing future procedures, a temperature to select might be one that is approximately 60°C below the peak heat capacity for the primary second phase. It must of course be remembered that DSC peaks may shift along the temperature scale for various reasons. Reviewing the DSC data shows that the temperature selected for warm rolling is above the temperature at which the dissolution of the second phase has begun. This implies that, during the rolling operations, there is a dynamic interaction between the matrix and the second phase. In fact, it may be more relevant for the TMP temperature to be positioned just above the temperature at which the heat capacity departs from zero than for it to be positioned at a specified number of degrees below the peak. On this basis, it is conceivable that, for best superplastic results, 6-2 should be rolled below 300°C. This of course does not consider the rolling difficulties encountered. This alloy might well require that a rolling temperature be chosen which does not offer the optimum SPD results.

It is well-known that diffusion kinetics within an alloy increase rapidly as the second phase solvus is approached and it might be anticipated that such a phenomenon may aid superplastic deformation mechanisms which are diffusion controlled. It is also interesting to note that the optimum SPD forming temperature and the TMP warm rolling temperature for both 8-1 and 6-1 were the same. It is

tempting to speculate that, during the rolling passes and reheating, the microstructure is achieving a stable structure specific to the temperature at which it is being rolled.

The DSC was perhaps most informative concerning the 6-2 alloy, as it detected the presence of  $\delta'$  which was later confirmed by TEM and by concurrent age hardening research. Since the other evaluations did not take place until after the TMP, only DSC information was available to characterize the microstructure and to select TMP temperatures. Although not central to this research, it is evident that only the DSC was able to detect the presence of GP zones since imaging in the TEM is known to be very difficult.

## B. MECHANICAL PROPERTIES

For the 8-1 and 6-1 alloys, precipitation follows the Al-Mg phase diagram and lithium behaves as a minor alloying addition. There was some speculation during the design of these alloys that Mg might force lithium out of solution in the form of  $\delta'$ . It has been reported that there is no  $\delta'$  formation in alloys with less than 1.5 wt. pct. Li; however none of the previous alloys (5 wt. pct. Mg) contain the large amount of Mg present in the alloys in this work. It would appear, however, from TEM observations (no  $\delta'$ ) that the reverse effect occurs, i.e. lithium would seem to displace Mg from solid solution promoting an increased volume fraction of  $\beta$  ( $\text{Al}_8\text{Mg}_5$ ). The 8-1 2 alloy has approximately the same total solute content as the 6-1 alloy. For each, a value of total atomic percent was calculated from the nominal weight percentages.

If it is assumed that the lithium remained in solid solution (as suggested by DSC and TEM results) and thus displaced magnesium on an atom for atom basis, then an equivalent magnesium content can be determined. These values are listed in Table 7. Using these equivalent Mg weight percent values and knowing that, at 300°C, the  $\beta$  solvus is located at 7.6 wt. pct. magnesium [Ref. 4: p. 313], and the solubility of Mg in  $\beta$  is 36.1 wt. pct., then a simple lever rule calculation can be performed. Results of this calculation give a weight percent fraction of  $\beta$  phase in each alloy and are also shown in Table 7.

Review of the ductility versus strain-rate data of Figure 4.12 shows a similar pattern of behaviour in the 6-1, 8-1 and 10-0 alloys. All three exhibit peak ductility at or below  $6.67 \times 10^{-2} \text{ sec}^{-1}$  and this most likely reflects a very similar volume fraction of  $\beta$  phase in each case. If the alloying content has not substantially altered the

TABLE 7  
TOTAL ATOMIC PERCENT SOLUTE CONTENT AND EQUIVALENT  
MAGNESIUM CONTENT

Alloy	Total Atomic % Solute	Equivalent Mg Atomic %	Expected $\beta$ Volume Fraction
6-1	10.6	9.5	7.6
8-1 2	10.8	9.8	8.6
10-0	11.1	10.0	13.6
8-1	12.8	11.5	15.5
6-2	14.4	13.0	-

morphology of the second phase, one would expect the grain size and ductility to be the same and, to the extent of the data available, this appears to be the case. It is appealing to think of the lithium displacing magnesium out of solution during the warm working. If this is indeed the mechanism, then it would seem possible to maintain a constant  $\beta$  volume fraction with less magnesium. An alternative explanation for the maintenance of superplastic properties is that the lithium is more directly affecting the component structures. For example it may assist in preventing the coarsening of the  $\beta$  phase particles or it could have a stabilizing effect on grain boundaries. Comparing the micrographs of Figure 4.13, the 8-1 alloy shows an apparently higher grain boundary misorientation than the non-lithium containing specimen which may be due to an ability of the lithium to assist in more fully recrystallizing the overall microstructure.

The 8-1 alloy demonstrated exceptional ductility of 1059% elongation at a strain rate of  $1.7 \times 10^{-2} \text{ sec}^{-1}$ . This infers that the combination of a small addition to the lithium content and the added reheat time between passes has resulted in an improvement from 600% to over 1000%. The results have also confirmed that the optimum temperature at which to superplastically deform this alloy is 300°C. These results have important implications for the possible introduction of this alloy into commercial service.

With most superplastic alloys exhibiting optimum tensile elongations of 500 - 1000%, this alloy clearly is near the high end of the range. With this high ductility, it

will be possible to form extremely complex shapes using SPF technology. Possibly more significant still is the high strain rate at which the elongation can be achieved. At the strain rate of  $1.7 \times 10^{-2} \text{ sec}^{-1}$ , the 1000% value is reached in only ten minutes. This high strain rate formability is an important breakthrough because the limitations of applying superplastic forming to high volume production may be overcome. A third important attribute of this alloy is the forming temperature of  $300^\circ\text{C}$ . Grimes reports that forming at  $600^\circ\text{C}$  requires more expensive materials for the production facilities [Ref. 21: p. 382]. He continues by pointing out that, at  $480^\circ\text{C}$ , relatively inexpensive tooling can be employed. From this one can only assume that a temperature reduction to  $300^\circ\text{C}$  would result in further cost savings. The higher the forming temperature, the lower will be the flow stress but the higher will be the superimposed back pressure requirements due to cavitation difficulties. The 8-1 alloy does have relatively high flow stress values due, in the main, to the lower forming temperature but, since no cavitation is observed, back pressure requirements and therefore forces required for forming will remain within the limits of current commercial processes. The combination of 1000% elongations, very high strain rates and low forming temperatures clearly make this a most attractive commercial alloy.

The overall flow stress versus strain rate data and the corresponding ductility plots show a familiar trend. As temperature increases from  $275 - 300^\circ\text{C}$ , the flow stress and ductilities decrease. On average, over all strain rates, there is little apparent difference in the m-value. With further heating, the flow stress increases which is consistent with observations made in previous work. TEM data have shown that grain growth can be significant at these temperatures. When the lithium containing alloy flow stress data are compared to the 10-0 plot, we see an overall higher m-value and a trend to increasing values at more rapid strain rates.

Applied mechanical models predict that, as the m-value increases, a resistance to necking will result to the point where, if  $m = 1$ , there will be no necking observed. This resistance to necking will result in greater elongations and thus a direct relationship between maximum m-value and maximum ductility is established. However, two important assumptions have been made in taking this approach. Firstly, the m-value is determined from data near the initiation of plastic deformation and it is implied by the analysis that the structure is stable throughout the deformation process. Secondly, it is assumed that all fractures will occur in a consistent manner. Since there does not yet exist an adequate model to predict fracture mode, the assumption that a consistent

fracture will occur may not be totally valid. In fact, the appearance of the fracture surfaces of the samples tested in this work varied considerably depending on strain rate and temperature. The fracture modes observed were necking to a fine point at one extreme and showed a more blunted, tearing fracture with little or no evidence of localized necking at the other. This variable fracture mode is unlikely to be predicted by the simple mathematical models currently employed in SPD studies.

It must be stated that the mechanical data for these alloys show an overall trend which supports the applied mechanics theory. At 275°C the flow stress is higher and, as temperature increases, the flow stress generally decreases. This is not unexpected in view of the important role played by diffusion in the deformation mechanism. The unusual 8-1 results seen at 350°C may well be caused by a heating rate effect. Data obtained by Salama for high Mg alloys shows that, at temperatures approaching the  $\beta$  solvus, a transition occurs where microstructure can change in size rapidly [Ref. 22]. Whether this transition reflects continuous recrystallization followed by growth due to the dissolution of the  $\beta$  phase or a discontinuous recrystallization process, the end result is that, over a narrow temperature range, grain size increases rapidly by a factor of ten. This effect has been found to depend sensitively on the heating rate experienced by the alloy, and the apparently anomalous data observed at 350°C may well be the result of this effect.

Evidence that this might be the case can also be found in TEM performed by Ferris [Ref. 20]. He observed a much different microstructure in the same alloys as studied here, with the only difference being that they were heated in an aging furnace where heating rate would be higher. A similar development can be seen in this work by comparing the microstructures of 6-2 samples, one of which had been cycled in the DSC and the other aged for 1 hour. The DSC cycled sample, which would experience the higher heating rate, was seen to be coarser than that of the aged sample.

Little concrete data is available on the effect of grain size on m-value. This weakness in the theoretical understanding of the SPD mechanism is well-known, but practical difficulties in obtaining sufficient data to relate temperature, strain rate, total elongation and grain growth have prevented any rapid progress toward understanding these questions. Except for the problem of failure mode prediction, if it were possible to predict the grain size in a material with known starting conditions and a known deformation rate, then the m-value, thus calculated, would accurately predict the

maximum elongation. Since this is not the case, use of the apparent m-value to predict maximum elongation is not straightforward. Flow stress and ductility data observed with the 8-1 and 6-1 alloys do not correlate as the currently available model would predict.

The inability to warm work 6-2 successfully was due principally to alligatoring and edge cracking. These are described by Scott, who states that they occur most readily when the roll diameter is large with respect to the sample thickness [Ref. 23]. This implies that, as the sample is rolled, these problems become more acute. This is supported by this work to the extent that cracking which occurred later in the rolling tended to be more serious than that noted in the initial passes. The number of variables which might impact on this is large. They include rolling temperature, alloy content, reduction per pass, reheat time and roll diameter as well as sample preparation. While temperature variations were used in this work, only three attempts to roll the alloy were carried out and optimizing rolling temperature should not be ruled out as a possible contribution to the solution. The 6-2 alloy has the highest alloying element content of the four alloys involved and this may have contributed to the rolling difficulties. In high solute content alloys containing lithium, a weakening of grain boundaries parallel to the rolling direction has been noted [Ref. 24]. By reducing the reduction per pass, the stresses introduced into the materials would be reduced and, given sufficient time at temperature, it may be possible for the structure to accommodate these stresses before the next rolling pass thereby lowering the strain hardening effects.

Rolling speeds may be a useful variable in that the rate of deformation may be too fast for the microstructural accommodation to take place. The sample itself may be better able to withstand rolling strains if stress concentration points along edges and at the point of initiation of the alligatoring are removed by more careful sample preparation. Finally, since the roll diameter-to-thickness ratio has been determined to play a role in these difficulties, one possible solution is to roll with smaller diameter rolls. In view of the many combinations of the possible changes to the TMP, a narrowing of options must be made. Since the simplest way to soften aluminum is to raise the temperature, this should be done as much as is consistent with retaining the primary second phase. DSC data indicates the highest possible temperature that will retain  $\text{Al}_2\text{MgLi}$  in precipitate form is 380°C. Therefore the most practical next step would be to roll with a smaller reduction per pass (e.g. 1 mm) at 380°C.

### C. TEM

The TEM data show that 8-1 2, 6-1 and 8-1 alloys are all similar in overall structure. It is evident that, for all three alloys, the size of the structure is closely related to the second phase interparticle spacing. When the microstructures are compared, they show that, as total alloying content increases, the microstructure becomes more uniform and tends to be finer. The  $\beta$  phase particles are clearly the reason for this observation since TEM shows that the 8-1 alloy has a higher volume fraction and much more evenly distributed  $\beta$  phase. The more fine-grained structure observed in the 8-1 alloy was the reason it was able to sustain the extreme elongations of over 1000% at strain rates as high as  $1.7 \times 10^{-2} \text{ sec}^{-1}$ .

The obvious relationship seen in the TEM between  $\beta$  phase and the grain size is further evidence that microstructural instability resulting from the dissolution of  $\beta$  phase is the most likely explanation for the drop in SP properties seen as the  $\beta$  solvus temperature is approached. Areas of the microstructure where  $\beta$  is scarce are clearly more coarse than other areas, thus it is a logical projection that, as the second phase dissolves into solid solution, the structure will coarsen leading to the reduced ductilities as discussed previously. A series of TEM experiments conducted upon samples which had been deformed at different temperatures and strain rates could provide conclusive evidence of this; unfortunately time constraints did not allow this to be performed. Nonetheless, variations in the deformation temperature near the  $\beta$  solvus have a significant impact on superplastic properties.

In all three alloys, there was no TEM evidence seen for  $\delta'$  phase which supports the DSC data seen previously. The presence of this phase would provide the opportunity to employ age hardening following a superplastic forming operation and thereby improve ambient temperature properties with a post production heat treatment. The lack of this ability in these alloys implies that they will be limited to applications where moderate strengths are acceptable.

The 6-2 alloy demonstrates significantly different properties in the TEM investigation. The lack of  $\beta$  phase and the appearance of  $\text{Al}_2\text{MgLi}$  were the most immediately noted differences. The  $\text{Al}_2\text{MgLi}$  phase appeared at a much lower volume fraction than that for  $\beta$  in the 8-1 alloy but did appear to perform the substructure stabilization function in much the same manner. In fact, the appearance of the alloy under TEM investigation most closely resembled that of the 6-1 microstructure just

prior to deformation. This suggests that it might respond superplastically in this condition, but the TMP must first be improved to prevent the severe cracking experienced. The absence of  $\beta$  phase and the appearance of the  $\text{Al}_2\text{MgLi}$  and  $\delta'$  phases demonstrates that this is a true ternary Al-Mg-Li alloy. Perhaps more important in the long term is the presence of the  $\delta'$  phase. This alloy has proven to possess an age hardening capability and the  $\delta'$  is clearly the reason for this ability. If superplastic forming can be made practical, this alloy has the potential to produce superplastically formed components which can subsequently be age hardened to produce components in a moderate-to-high strength aluminum alloy.

## VI. CONCLUSIONS

1. DSC can be a useful aid in selecting TMP temperatures; the 8-1 2, 8-1 and 6-1 alloys were shown to be quasi-binary with respect to precipitation sequence. This allowed for the same TMP to be used to produce superplastic behaviour as in the Al-Mg alloys studied previously.
2. Experience with the 6-2 alloy demonstrates that DSC cannot be used in isolation. This alloy behaved as a true ternary which possessed a strikingly different microstructure than alloys with lower Li content. The presence of the  $\text{Al}_2\text{MgLi}$  phase had an apparent embrittling effect which did not permit effective thermomechanical processing of the alloy.
3. The combination of DSC and TEM data indicated that no  $\delta'$  precipitation occurred in alloys with less than 1 wt. pct. Li which is consistent with previous results.  $\delta'$  precipitation was observed in the 1.6 wt. pct. Li threshold concentration cited by other authors.
4. Mechanical property data show that  $300^\circ\text{C}$  ( $0.7T_m$ ) is the optimum temperature for SPD in these alloys. At this temperature and a strain rate of  $1.7 \times 10^{-2}$ , the 8-1 alloy exhibited elongations in excess of 1000% without cavitation.
5. TEM data confirm that the increased ductility associated with a higher total solute content is a result of the greater volume fraction of  $\beta$  phase present in the microstructure.
6. The  $\beta$  phase is the major microstructural constituent which controls grain size and structural stability both during TMP and SPD. The higher the volume fraction of  $\beta$  the more refined was the resultant microstructure.
7. Li additions have a greater effect than simply displacing additional Mg from solution. This appears to derive from an ability to prevent  $\beta$  coarsening during elevated temperature testing.
8. The concept of microstructural evolution via continuous recrystallization in these alloys was confirmed. However, the materials were shown to be very sensitive to heating rate and final deformation temperature with respect to the triggering of discontinuous recrystallization processes.

## VII. RECOMMENDATIONS

1. Further study of the precise role of lithium in improving the superplastic response of aluminum-magnesium alloys should be undertaken. The results of such a study could reveal new information on the superplastic phenomenon.
2. Additional research into the fundamental mechanisms of superplasticity would provide insight and the ability to further improve the performance of these alloys.
3. A more complete assessment of both ambient and elevated temperature properties of the 6-1, 8-1 2, and 8-1 alloys should be performed. In particular, a more extensive matrix of elevated temperature tests would permit greater confidence in flow stress versus ductility correlations.
4. It is further recommended that the results of this research be brought to the attention of the aluminum industry as these alloys have clear commercial and industrial potential.
5. In view of the combination of low density and high strength, the 6-2 alloy should be examined in detail to determine the optimum TMP to permit the earliest possible assessment of elevated temperature properties.

## APPENDIX A

### DIFFERENTIAL SCANNING CALORIMETRY

The Differential Scanning Calorimeter (DSC) used in this work was a Perkin-Elmer DSC-2C connected to a Perkin-Elmer paper chart recorder. Two purge gas systems both using nitrogen were employed, one connected to the isolation box and the other to the sample holder. For all experiments the outer purge system was pressurized briefly before operating the device to remove any water vapour introduced during the placement of the sample, and the inner system was set at a flow rate of 20 ml per minute and operated until completion of each series. The machine was first conditioned at 1000°C for approximately 1 hour as described in the operations manual. Following this, a temperature calibration sequence was performed using Indium and Potassium Chromate reference samples. The machine settings for these runs are shown in Table 8.

TABLE 8  
DSC CALIBRATION SETTINGS

Control	Indium	Potassium Chromate
range	5 mcal/sec	5 mcal sec
heating rate	10 deg/min	10 deg min
chart speed	80 mm/min	80 mm/min
pen 2	20 mV	50 mV
low temp	410 K	920 K
high temp	500 K	999 K

Using the calibration equation from page 3-14 of the manual the adjustment was calculated as shown below:

$$\Delta R = R^2 \times \frac{\Delta T_{ind} - \Delta T_{act}}{\Delta T_{act}} \times \frac{1}{1000}$$

$$\begin{array}{r}
 514.55 - 513.9 \quad 1 \\
 = (894)^2 \quad \hline \quad x \quad \hline \\
 \quad \quad \quad 513.9 \quad 1000 \\
 \\ = 1.01
 \end{array}$$

This adjustment was applied to the range control and the final temperature settings were:

Range	895
Zero	29.4

A final confirmation test was performed and the two transition temperatures were found to be within the expected limits.

The next step was to establish DSC settings which would result in the best possible baseline traces for the materials which were to be used in this series of experiments. The best results were found when a representative sample having approximately the same mass as that to be tested was used in the calibration. For this reason, a series of test runs with samples of masses ranging from 3 - 6 mg was performed and for each case the best machine settings were recorded. The difficulty experienced here was that it was found that changing any one control setting affected the other settings. The most significant of these was the inter-relationship of the  $\Delta T$ , zero, and slope controls. After some random alteration of these three, it was determined that, within a very narrow sample mass range, the use of the slope control could provide the necessary fine tuning of the baseline but, if the mass changed by more than 1 mg, it was necessary to alter the zero control. In the interests of reproducibility and ease of operation, it was decided not to alter the  $\Delta T$  control (used to adjust the baseline curvature) after an approximately optimal setting of 410.6 was found early in the testing.

Since the reactions occurring within the sample alloys are relatively low energy compared to, for example, the melting of water, it was necessary to optimize the overall experimental sensitivity. This involved the range setting of the DSC and the pen range settings on the paper chart. The manual explained that, for best results under normal circumstances, the higher DSC range settings are preferred as this will

allow for more accurate solvus temperature determination. This meant that the pens would need to be set at relatively high sensitivities to permit the reactions to be seen. For all runs in this work, the DSC range was set at 5 mCal sec. Pens 1 and 2 were set at 1 mV and 2 mV (full scale deflection) respectively for most of this work.

Once the baseline was optimized, the experiments involved heating the samples at a rate of 40°C per minute over a temperature range of approximately 100 - 700°C. Following that, the samples were cooled at the maximum cooling rate of 320 °C and a second and third heating cycle was performed. The results of the second and third heating cycles were compared to determine any variability occurring in the machine readings and from this a baseline trace was established to which the first trace could be compared. Due to the quench rate sensitivity of 6-1, this technique could not be used to define a baseline. Samples of pure aluminum with approximately the same mass were run and traces produced by these runs were used to define baselines for this alloy. For all alloys, the difference between the first trace and the baseline was measured at evenly spaced intervals over the temperature range of 100 - 440°C.

This value was used to calculate the heat capacity in J Kg-K. The following equation was employed to convert the number of divisions measured on the paper recorder to heat capacity:

$$C_p = \frac{\text{div} \times R(\text{mCal sec}) \times 4.186(\text{J Cal}) \times 60(\text{sec min}) \times P(\text{mV}) \times 1000}{F_s (\text{mV}) \times M (\text{mg}) \times HR (\text{K min})}$$

where: div = number of divisions measured on chart

R = DSC range

P = pen scale

F<sub>s</sub> = full scale output from DSC (10 mV)

M = sample mass

HR = heating rate (40 K min)

note: the factor of 1000 converts units from mJ mg-K to J Kg-K

These calculated results were tabulated and entered into the NPS mainframe computer. At least three samples of each material of interest were run and the results were plotted for comparison and analysis using the Easyplot graphics plotting software. The results of these experiments are discussed in the body of this work.

**APPENDIX B**  
**TRUE STRESS DATA**

AL-8%MG-1%LI @ 275 C

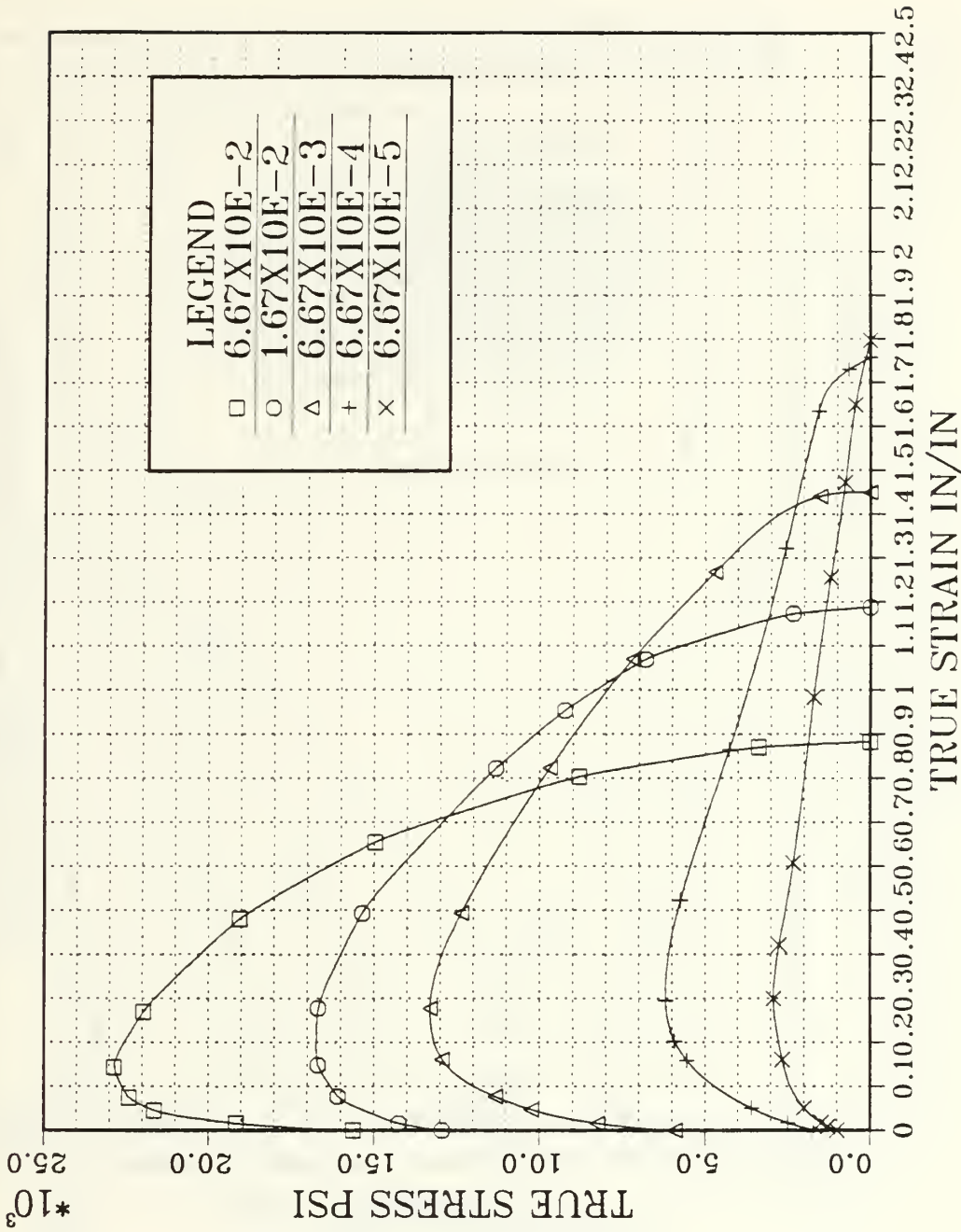


Figure B.1 The 8-1 Alloy at 275°C

AL-8%MG-1%LI @ 300 C

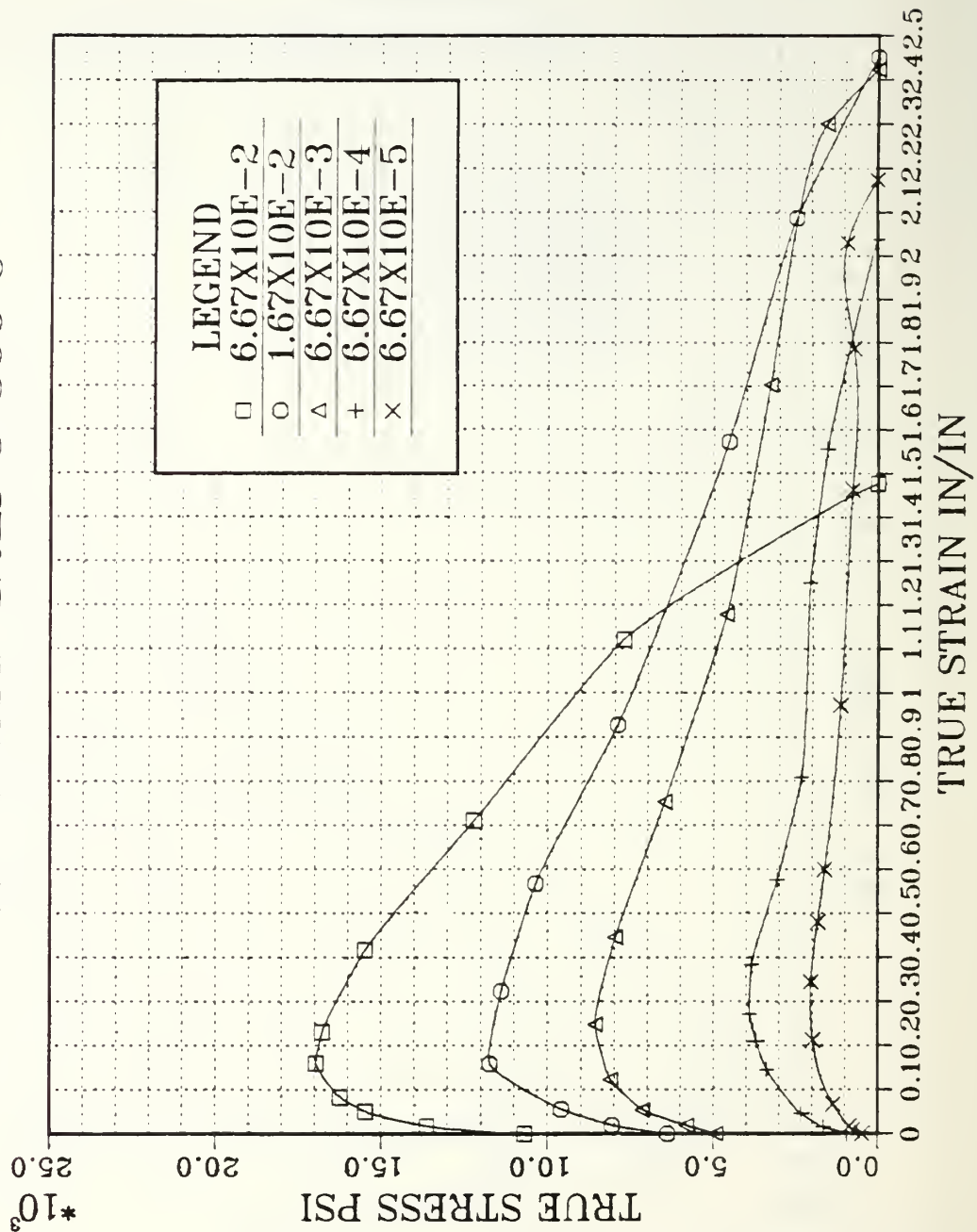


Figure B.2 The 8-1 Alloy at 300°C

AL-8%MG-1%LI @ 325 C

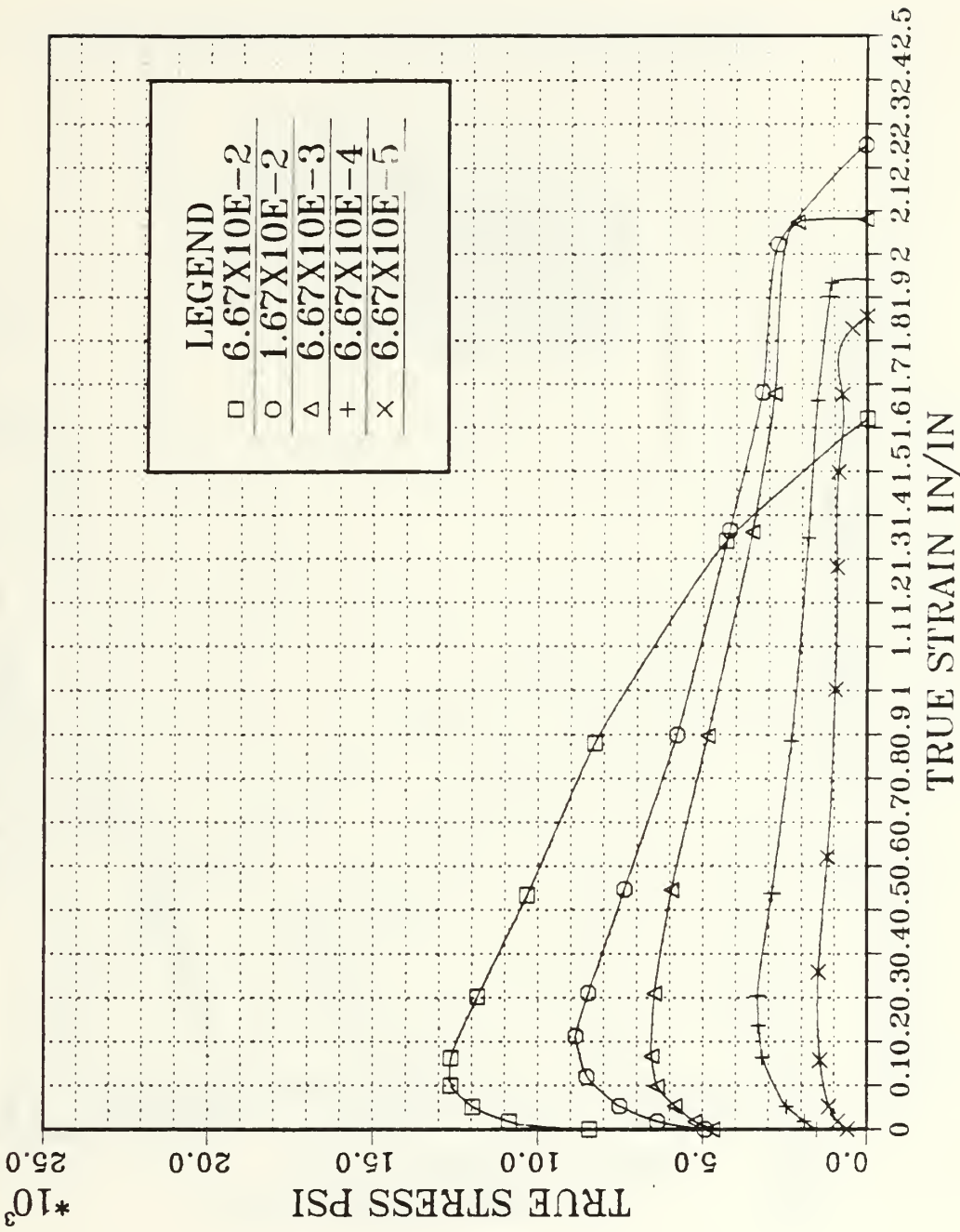


Figure B.3 The 8-I Alloy at 325°C

AL-8%MG-1%LI @ 350 C

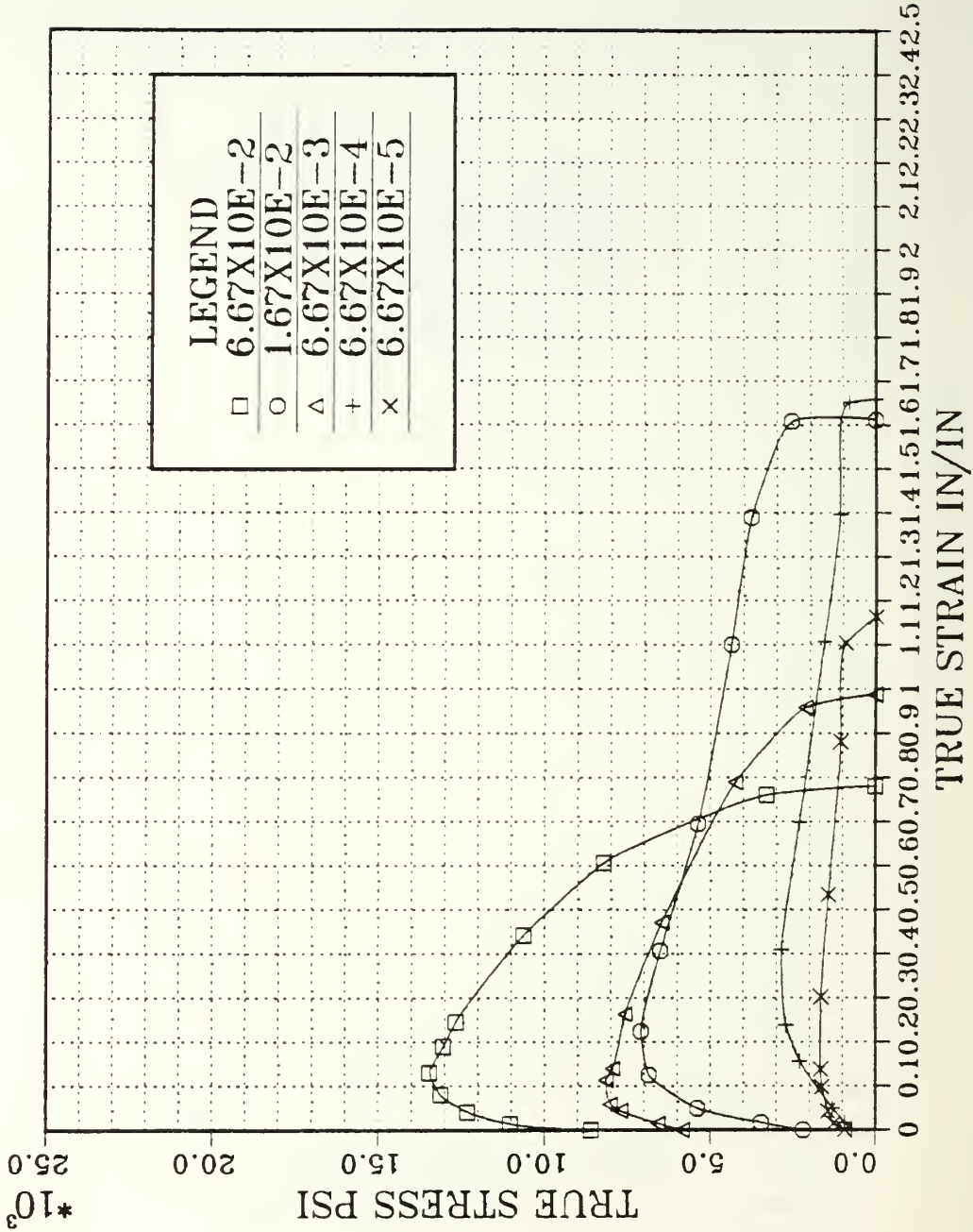


Figure B.4 The 8-1 Alloy at 350°C

AL-6%MG-1%LI @ 275 C

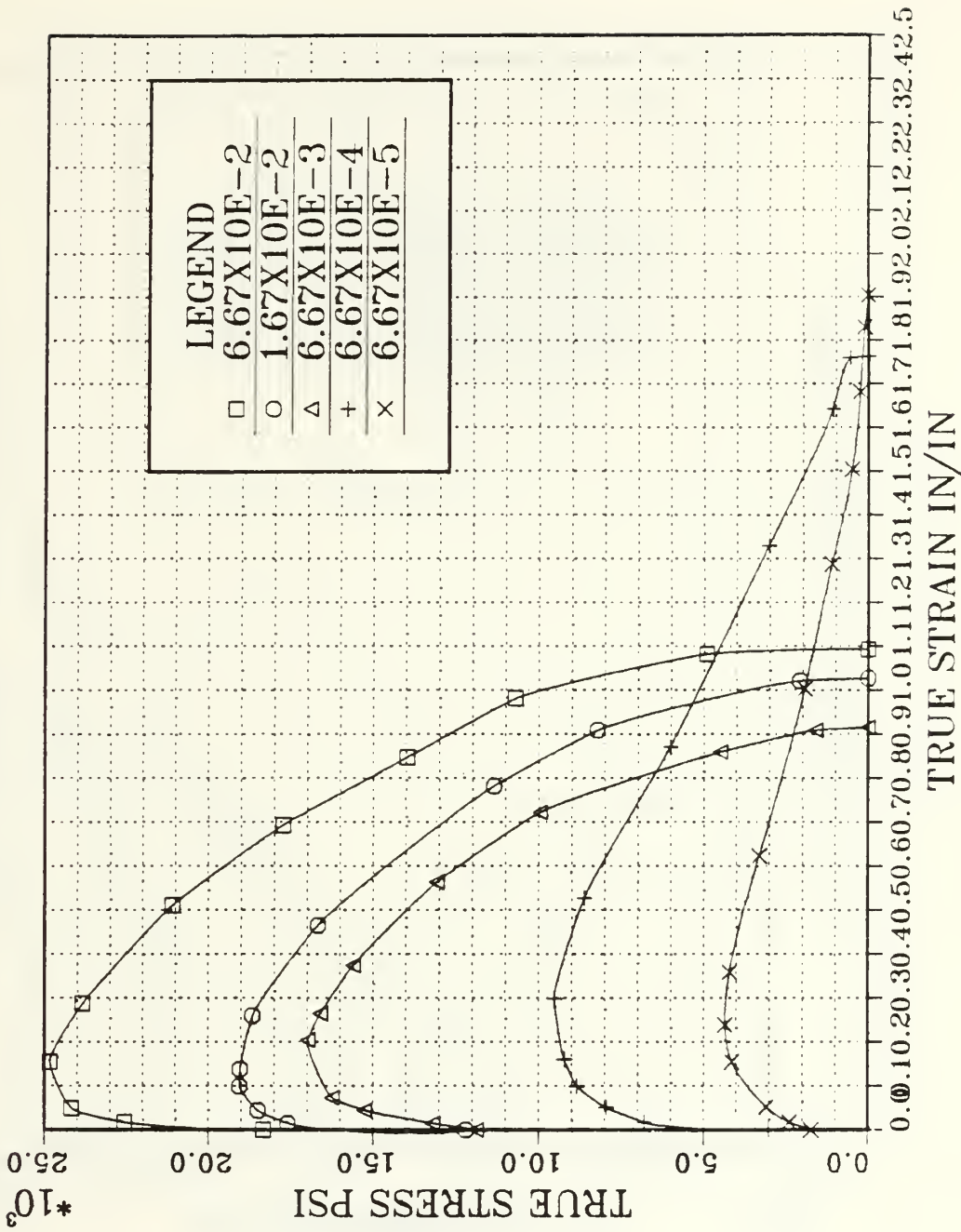


Figure B.5 The 6-1 Alloy at 275°C

AL-6%MG-1%LI @ 300 C

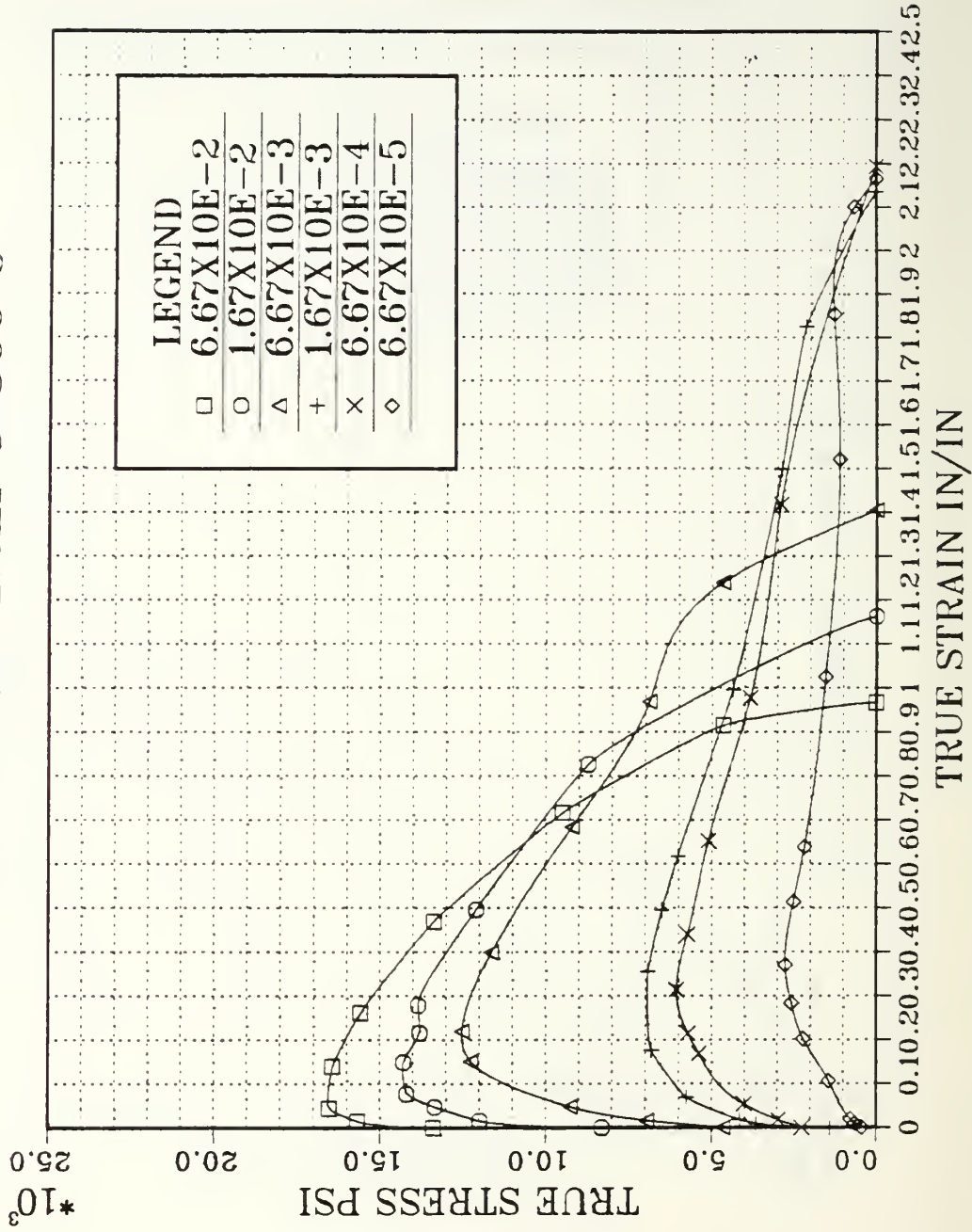


Figure B.6 The 6-1 Alloy at 300°C

AL-6%MG-1%LI @ 325 C

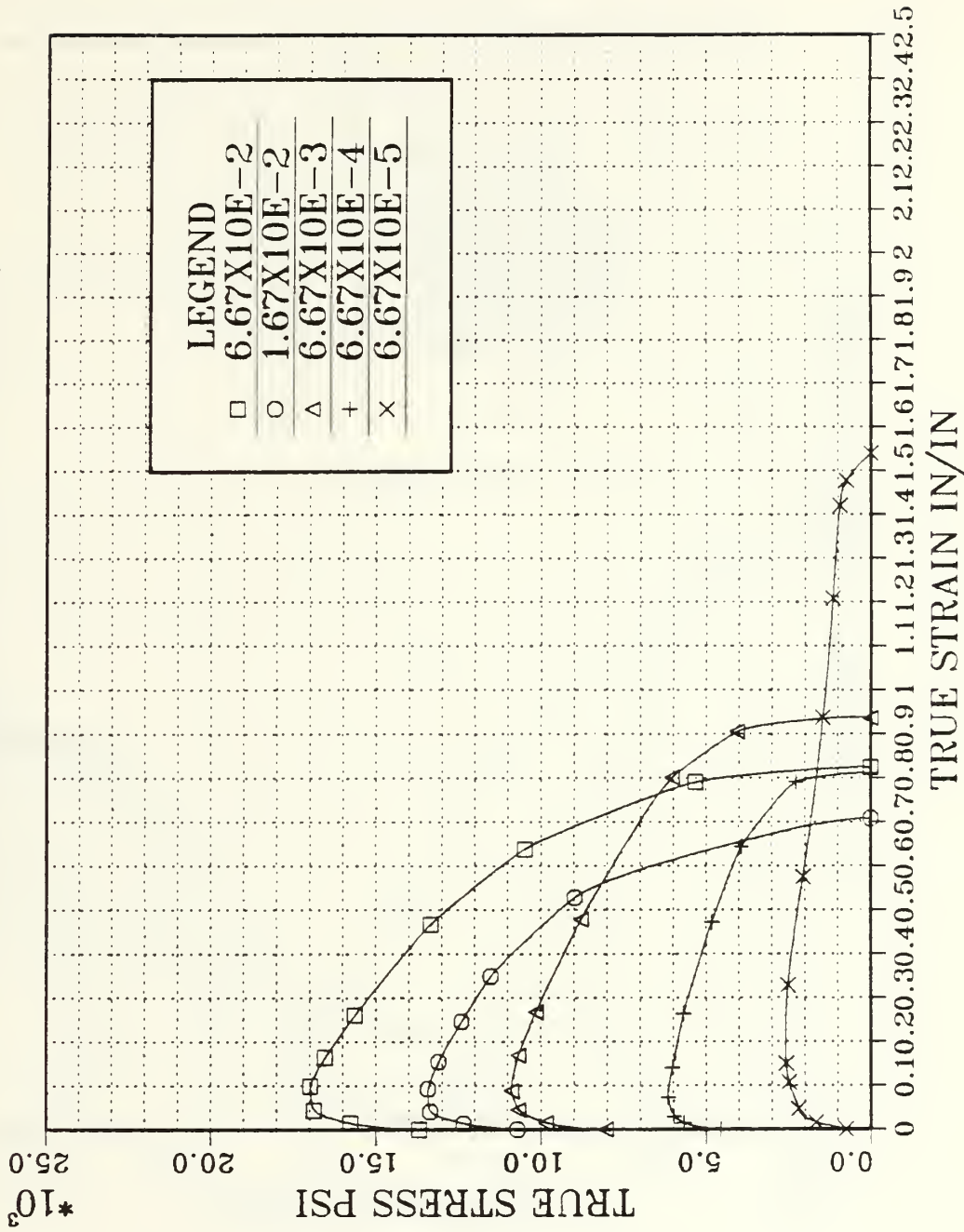


Figure B.7 The 6-1 Alloy at 325°C

AL-6%MG-1%LI @ 350 °C

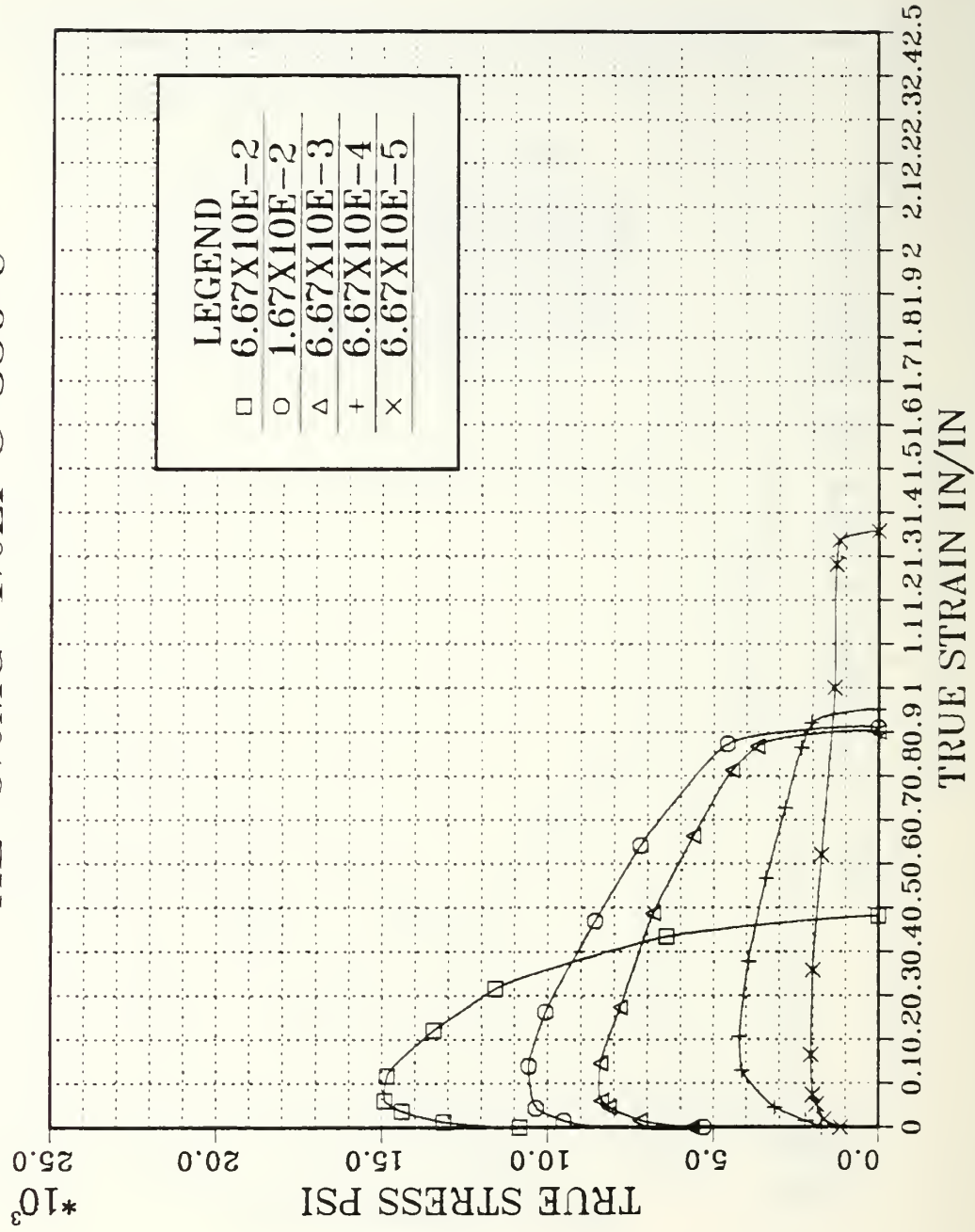


Figure B.8 The 6-1 Alloy at 350°C

AL-8%MG-0.5%LI @ 300 C

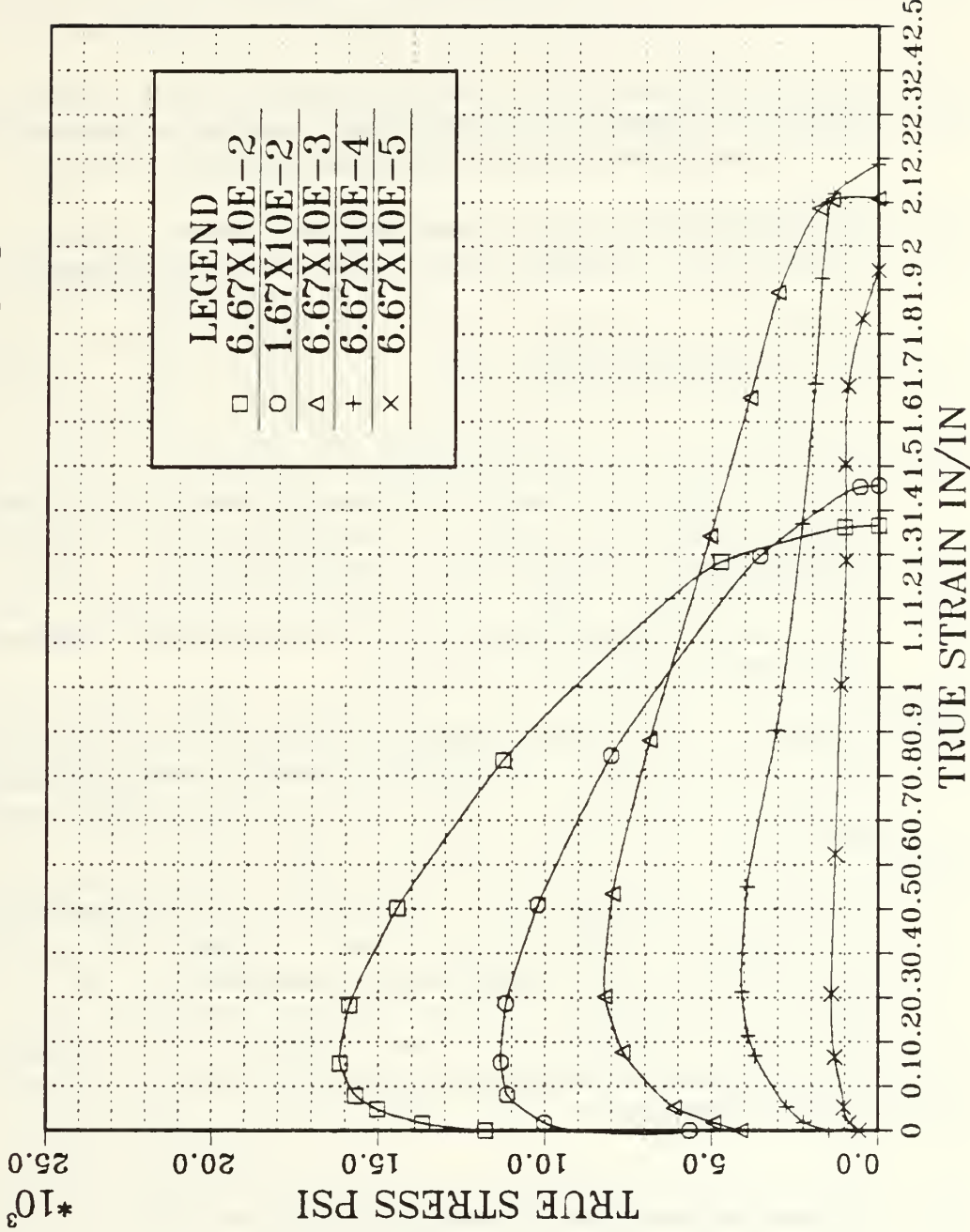


Figure B.9 The 8-1/2 Alloy at 300°C

## LIST OF REFERENCES

1. Oster S.B., *Effect of Thermomechanical Processing on the Elevated Temperature Behavior of Lithium-containing High-Mg, Al-Mg Alloys*, Masters Thesis, Naval Postgraduate School, Monterey, California, June 1985.
2. Sanchez B.W., *Processing and Superplasticity in Lithium Containing Al-Mg Alloys*, Masters Thesis, Naval Postgraduate School, Monterey, California, March 1987.
3. Hatch, J.E., ed., *Aluminum: Properties and Physical Metallurgy*, pg. 47, American Society for Metals, 1984.
4. Mondolfo, L.F., *Aluminum Alloys: Structure and Properties*, Butterworths, 1976.
5. Hales, S.J., Oster, S.B., Sanchez, B.W. and McNelley, T.R., "Grain Refinement and Superplasticity in a Lithium Containing Aluminum-Magnesium Alloy by Thermomechanical Processing," *Acta Met.*, in press.
6. Brosilow, R., "Aircraft Bodies: New Joining Processes," *Welding Design and Fabrication*, Vol. 58, pg. 57, March 1985.
7. Bauman, S.F. and Williams, D.B., "The Effect of Ternary Additions on the  $\delta'$   $\alpha$  Misfit and the  $\delta$  Solvus Line in Al-Li Alloys," *Aluminium-Lithium Alloys II*, Sanders, T.H. and Starke, E.A., eds., pg. 18, The Metallurgical Society of Aime, 1984.
8. Sanders, T.H. and Starke, E.A., "Overview of the Physical Metallurgy in the Al-Li-X Systems," *Aluminium-Lithium Alloys II*, Sanders, T.H. and Starke, E.A., eds., pp. 1-15, The Metallurgical Society of Aime, 1984.
9. Fridlyander, A.N., Sandler, U.S. and Nikol'skaya, T.I., "Investigation of the Aging of Aluminium-Magnesium-Lithium Alloys," *Phys. Met. Metallog.*, Vol. 32, pp. 93-100, 1971.
10. Parson, N.C. and Sheppard, T., "Extrusion Processing of Al-Mg-Li Alloys," *Aluminium-Lithium Alloys III*, Baker, C., Gregson, P.S., Harris, S.J. and Peel, C.J., eds., pp. 222-232, The Institute of Metals, 1986.
11. Gayle, F.W. and Vandersande, J.S., "Composite Precipitates in an Al-Li-Zr Alloy," *Scripta Met.*, Vol. 18, pp. 473-478, 1984.

12. Pearce, R., "Superplasticity - An Overview," *Superplasticity* pp. 11-24, Advisory Group for Aerospace Research and Development, NATO, 1987.
13. Sherby, O.D. and Wadsworth, J., "Development and Characterization of Fine-grained Superplastic Materials," *Deformation Processing and Structure*, Krauss, G., ed., pp. 355-390, American Society of Metals, 1984.
14. Wise, J.E., *The Influence of Total Strain, Strain Rate and Reheating Time During Warm Rolling on the Superplastic Ductility of an Al-Mg-Zr Alloy*, Masters Thesis, Naval Postgraduate School, Monterey, California, March 1987.
15. Stewart, D.L., *Investigation by Differential Scanning Calorimetry of Microstructure in a Superplastic Al-Mg-Zr Alloy*, Masters Thesis, Naval Postgraduate School, Monterey, California, June 1987.
16. Hales, S.J. and McNelley, T.R., "Microstructural Evolution by Continuous Recrystallization in a Superplastic Al-Mg Alloy," *Acta Meta.*, in press.
17. Papazian, J.M., "The Effects of Warm Working on Aluminum Alloy 7075-T651," *Materials Science and Engineering*, Vol. 51, pp. 223-230, 1981.
18. Rioja, R.J. and Ludwiczak, E.A., "Identification of Metastable Phases in an Al-Cu-Li Alloy (2090)," *Aluminum-Lithium Alloys*, Paper presented at the third Aluminum-Lithium Conference, University of Oxford, July 1985.
19. Alcamo, M.E., *Effect of Strain Rate on the Microstructure of a Superplastically Deformed Al-10% Mg-0.1%Zr Alloy*, Masters Thesis, Naval Postgraduate School, Monterey, California, June 1985.
20. Ferris, W.F., *The Age Hardening Response of Thermomechanically Processed Al-Mg-Li Alloys*, Masters Thesis, Naval Postgraduate School, Monterey, California, December 1987.
21. Grimes, R., "The Manufacture of Superplastic Alloys," *Superplasticity*, pp. 8.1-16, Advisory Group for Aerospace Research and Development, NATO, 1987.
22. Salama, A., *Analysis of Grain Refinement and Superplasticity in Aluminum-Magnesium Alloys*, Doctoral Thesis, Naval Postgraduate School, Monterey, California, December 1987.
23. Scott, T.E., "Ingot and Billet Processing of Aluminum Alloys," *Aluminum Alloys-Physical and Mechanical Properties*, Vol. III, Engineering Materials Advisory Services Ltd., June 1986.
24. Crooks, R., Rockwell Science Center, Thousand Oaks, California, July 1987, unpublished research.

## INITIAL DISTRIBUTION LIST

	No. Copies
1. Defense Technical Information Center Cameron Station Alexandria, VA 22304-6145	2
2. Library, Code 0142 Naval Postgraduate School Monterey, CA 93943-5002	2
3. Department Chairman, Code 69Hy Department of Mechanical Engineering Naval Postgraduate School Monterey, CA 93943-5000	1
4. Professor T. R. McNelley, Code 69Mc Department of Mechanical Engineering Naval Postgraduate School Monterey, CA 93943-5000	5
5. Dr. S. J. Hales, Code 69He Department of Mechanical Engineering Naval Postgraduate School Monterey, CA 93943-5000	5
6. Naval Air Systems Command, Code AIR 921 Naval Air Systems Command Headquarters Washington, DC 20361	1
7. Capt. I.G. Munro, DAME 3 National Defence Headquarters 101 Colonel By Drive Ottawa, Ont. Canada K1A 0K2	5
8. Dr. E.-W. Lee, Code 6063 Naval Air Development Center Warminster, Pennsylvania 18974.	1
9. LCDR S. B. Oster 110 Teri Court, N.E. Bremerton, Washington 98310.	1
10. LCDR D.L. Stewart 515 Harolds Drive Huntsville, Alabama 35806.	1









Thesis

M9525 Munro

c.1 Optimizing superplastic  
response in lithium con-  
taining aluminum-magne-  
sium alloys.

Thesis

M9525 Munro

c.1 Optimizing superplastic  
response in lithium con-  
taining aluminum-magne-  
sium alloys.



